

NAVAL POSTGRADUATE SCHOOL

Monterey, California



THESIS

NUMERICAL EXPERIMENTS IN UNSTEADY FLOWS
THROUGH THE USE OF
FULL NAVIER-STOKES EQUATIONS

by

Christopher J. Putzig

June, 1991

Thesis Advisor:

T. Sarpkaya

Approved for public release; distribution is unlimited

T256379

REPORT DOCUMENTATION PAGE

1a. REPORT SECURITY CLASSIFICATION Unclassified			1b. RESTRICTIVE MARKINGS	
2a. SECURITY CLASSIFICATION AUTHORITY			3. DISTRIBUTION/AVAILABILITY OF REPORT Approved for public release; distribution is unlimited.	
2b. DECLASSIFICATION/DOWNGRADING SCHEDULE				
4. PERFORMING ORGANIZATION REPORT NUMBER(S)			5. MONITORING ORGANIZATION REPORT NUMBER(S)	
6a. NAME OF PERFORMING ORGANIZATION Naval Postgraduate School		6b. OFFICE SYMBOL (If applicable) ME		7a. NAME OF MONITORING ORGANIZATION Naval Postgraduate School
6c. ADDRESS (City, State, and ZIP Code) Monterey, CA 93943-5000			7b. ADDRESS (City, State, and ZIP Code) Monterey, CA 93943-5000	
8a. NAME OF FUNDING/SPONSORING ORGANIZATION		8b. OFFICE SYMBOL (If applicable)		9. PROCUREMENT INSTRUMENT IDENTIFICATION NUMBER
8c. ADDRESS (City, State, and ZIP Code)			10. SOURCE OF FUNDING NUMBERS	
			Program Element No.	Project No.
			Task No.	Work Unit Accession Number
11. TITLE (Include Security Classification) NUMERICAL EXPERIMENTS IN UNSTEADY FLOWS THROUGH THE USE OF FULL NAVIER-STOKES EQUATIONS				
12. PERSONAL AUTHOR(S) Christopher J. Putzig				
13a. TYPE OF REPORT Master's and Engineer's Thesis		13b. TIME COVERED From To		14. DATE OF REPORT (year, month, day) JUNE 1991
15. PAGE COUNT 150				
16. SUPPLEMENTARY NOTATION The views expressed in this thesis are those of the author and do not reflect the official policy or position of the Department of Defense or the U.S. Government.				
17. COSATI CODES			18. SUBJECT TERMS (continue on reverse if necessary and identify by block number)	
FIELD	GROUP	SUBGROUP	Numerical, Navier-Stokes, Impulsive Flow, Non-Impulsive Flow, Oscillating Flow, Co-existing Flow	
19. ABSTRACT (continue on reverse if necessary and identify by block number) The numerical simulations of impulsively started flow, non-impulsively started flow, sinusoidally oscillating flow, and, finally, co-existing flow (with mean and oscillatory components) past a circular cylinder have been investigated in great detail through the use of several compact schemes with the Navier-Stokes vorticity/stream function formulation for various Reynolds numbers, frequency parameters, and ambient flow/oscillating flow combinations using VAX-3520 and NASA's Supercomputers. Extensive sensitivity analysis has been performed to delineate the effects of time step, outer boundary, nodal points on the cylinder, and the use of higher order polynomials in the calculation of the gradient of wall vorticity. The results have been compared with those obtained experimentally. In many cases the predicted wake region, vorticity and pressure distributions, and the time-variation of the force coefficients have shown excellent agreement with those obtained experimentally.				
20. DISTRIBUTION/AVAILABILITY OF ABSTRACT <input checked="" type="checkbox"/> UNCLASSIFIED/UNLIMITED <input type="checkbox"/> SAME AS REPORT <input type="checkbox"/> DTIC USERS			21. ABSTRACT SECURITY CLASSIFICATION Unclassified	
22a. NAME OF RESPONSIBLE INDIVIDUAL Professor T. Sarpkaya			22b. TELEPHONE (Include Area code) (408) 646-3425	22c. OFFICE SYMBOL ME-SL

Approved for public release; distribution is unlimited.

Numerical Experiments in Unsteady Flows
Through the use of Full Navier Stokes Equations

by

Christopher J. Putzig
Lieutenant, United States Navy
B.S., University of Idaho, 1983

Submitted in partial fulfillment of the
requirements for the degree of

MASTER OF SCIENCE IN MECHANICAL ENGINEERING

AND

MECHANICAL ENGINEER

from the

NAVAL POSTGRADUATE SCHOOL

June 1991

ABSTRACT

The numerical simulations of impulsively started flow, non-impulsively started flow, sinusoidally-oscillating flow, and, finally, co-existing flow (with mean and oscillatory components) past a circular cylinder have been investigated in great detail through the use of several compact schemes with the Navier-Stokes vorticity/stream function formulation for various Reynolds numbers, frequency parameters, and ambient flow/oscillating flow combinations using VAX-3520 and NASA's Supercomputers. Extensive sensitivity analysis has been performed to delineate the effects of time step, outer boundary, nodal points on the cylinder, and the use of higher order polynomials in the calculation of the gradient of wall vorticity. The results have been compared with those obtained by others, whenever available, and with those obtained experimentally. In many cases the predicted wake region, vorticity and pressure distributions, and the time-variation of the force coefficients have shown excellent agreement with those obtained experimentally.

110313
P477
C.1

TABLE OF CONTENTS

I. INTRODUCTION.....	1
II. BACKGROUND STUDIES.....	4
III. NUMERICAL REPRESENTATION.....	8
A. COMPUTATIONAL METHOD.....	8
B. CALCULATION OF THE FORCE COEFFICIENTS.....	10
C. CALCULATION OF THE DRAG AND INERTIA COEFFICIENTS.....	14
1. Governing Parameters.....	15
IV. DISCUSSION OF RESULTS.....	17
A. INTRODUCTION.....	17
B. CHARACTERIZATION OF PERTURBATIONS.....	19
C. IMPULSIVE/NON-IMPULSIVE FLOW.....	20
D. IMPULSIVELY-STARTED FLOW.....	22
E. NON-IMPULSIVELY-STARTED FLOW.....	23
F. OSCILLATING FLOWS.....	26
G. OSCILLATING FLOW WITH CURRENT.....	35
V. CONCLUSIONS.....	39
APPENDIX.....	41
REFERENCES.....	132
INITIAL DISTRIBUTION LIST.....	135

LIST OF FIGURES

Figure 1.	Grid in the Physical Domain.....	41
Figure 2.	Grid in the Computational Domain	42
Figure 3.	C_{IL} versus S/R , $Re = 200$, — : $\Delta\alpha = 0.5$ ($S/R = 3-10$), : $\Delta\alpha = 5.0$ ($S/R = 3-5$), - - - : $\Delta\alpha = 0.5$ ($S/R = 3-10$)	43
Figure 4.	C_L versus S/R , $Re = 200$, (lines same as in Fig. 3)	43
Figure 5.	C_{IL} versus S/R , $\Omega = 0.1$, $Re = 1000$, $\Delta\xi = 1/64$	44
Figure 6.	C_L versus S/R , $\Omega = 0.1$, $Re = 1000$, $\Delta\xi = 1/64$	44
Figure 7.	Streaklines, $\Omega = 0.1$, $Re = 1000$, $\Delta\xi = 1/64$	45
Figure 8.	C_{IL} versus S/R , $\Omega = 0.1$, — : $Re = 250$, : $Re = 500$, - - - : $Re = 750$, : $Re = 1000$	46
Figure 9.	C_{IL} versus S/R , $\Omega = 0.1$, (lines same as in Fig. 8).....	47
Figure 10.	C_L versus S/R , $\Omega = 0.1$, (lines same as in Fig. 8).....	47
Figure 11.	C_{IL} versus S/R , $\Omega = 0.25$, — : $n = 2$, : $n = 4$, - - - : $n = 6$, : $n = 8$, : $n = 10$	48
Figure 12.	C_{IL} versus S/R , $\Omega = 0.25$, (lines same as in Fig. 11)	48
Figure 13.	C_{IL} versus S/R , $\Omega = 1$, $Re = 1000$, $\Delta\xi = 1/128$	49
Figure 14.	Pressure p_s around Cylinder versus Time(τ), $\Omega = 1$	50
Figure 15.	Vorticity Contours, $\Omega = 1$, $S/R = 1$	51
Figure 16.	Streamlines $\Omega = 1$, $S/R = 3$	52
Figure 17.	Vorticity Contours, $\Omega = 1$, $S/R = 3$	53
Figure 18.	C_{IL} versus S/R , $\Omega = 2$, $Re = 1000$, $\Delta\xi = 1/128$	54
Figure 19.	Pressure p_s around the Cylinder versus Time(τ), $\Omega = 2$	55
Figure 20.	Vorticity Contours, $\Omega = 2$, $S/R = 2$	56
Figure 21.	Streamlines $\Omega = 2$, $S/R = 2$	57
Figure 22.	Vorticity Contours, $\Omega = 2$, $S/R = 3.5$	58

Figure 23.	Streamlines $\Omega = 2, S/R = 4$	59
Figure 24.	Vorticity Contours, $\Omega = 2, S/R = 4$	60
Figure 25.	C_{IL} versus S/R , $\Omega = 3, Re = 1000, \Delta\xi = 1/128$	61
Figure 26.	Pressure p_s around the Cylinder versus Time(τ), $\Omega = 3$	62
Figure 27.	Streamlines, $\Omega = 3, S/R = 3$	63
Figure 28.	Vorticity Contours, $\Omega = 3, S/R = 3$	64
Figure 29.	Vorticity Contours, $\Omega = 3 S/R = 4.4$	65
Figure 30.	Streamlines, $\Omega = 3, S/R = 4.4$	66
Figure 31.	Streamlines $\Omega = 3, S/R = 4.6$	67
Figure 32.	Vorticity Contours, $\Omega = 3, S/R = 4.6$	68
Figure 33.	C_{IL} versus S/R , $\Omega = 10, Re = 1000, \Delta\xi = 1/128$	69
Figure 34.	Pressure p_s around the Cylinder versus Time(τ), $\Omega = 10$	70
Figure 35.	Streamlines, $\Omega = 10, S/R = 10$	71
Figure 36.	Streamlines, $\Omega = 10, S/R = 10.2$	72
Figure 37.	Streamlines, $\Omega = 10, S/R = 11.6$	73
Figure 38.	Streamlines (Total Ψ), $K = 1.5, \beta = 300, t/T = 4$	74
Figure 39.	Streamlines (Total Ψ), $K = 1.5, \beta = 300, t/T = 4.004$	75
Figure 40.	Streamlines (Total Ψ), $K = 3, \beta = 196, t/T = 6$	76
Figure 41.	Streamlines (Total Ψ), $K = 3, \beta = 196, t/T = 6.25$	77
Figure 42.	Streamlines (Total Ψ), $K = 3, \beta = 196, t/T = 6.5$	78
Figure 43.	Streamlines (Total Ψ), $K = 3, \beta = 196, t/T = 6.75$	79
Figure 44.	Streamlines (Relative Motion Ψ), $K = 3, \beta = 196, t/T = 6$	80
Figure 45.	Streamlines (Relative Motion Ψ), $K = 3, \beta = 196,$ $t/T = 6.25$	81
Figure 46.	Streamlines (Relative Motion Ψ), $K = 3, \beta = 196,$ $t/T = 6.5$	82
Figure 47.	Streamlines (Relative Motion Ψ), $K = 3, \beta = 196,$ $t/T = 6.75$	83
Figure 48.	Streamlines (Total Ψ), $K = 4, \beta = 196, t/T = 6$	84

Figure 49.	Streamlines (Total Ψ), $K = 4$, $\beta = 196$, $t/T = 6.25$	85
Figure 50.	Streamlines (Total Ψ), $K = 4$, $\beta = 196$, $t/T = 6.5$	86
Figure 51.	Streamlines (Total Ψ), $K = 4$, $\beta = 196$, $t/T = 6.75$	87
Figure 52.	Streamlines (Relative Motion Ψ), $K = 4$, $\beta = 196$, $t/T = 6$	88
Figure 53.	Streamlines (Relative Motion Ψ), $K = 4$, $\beta = 196$, $t/T = 6.25$	89
Figure 54.	Streamlines (Relative Motion Ψ), $K = 4$, $\beta = 196$, $t/T = 6.5$	90
Figure 55.	Streamlines (Relative Motion Ψ), $K = 4$, $\beta = 196$, $t/T = 6.75$	91
Figure 56a.	C_{IL} versus t/T , $K = 1.5$, $\beta = 300$, — : $n = 2$, : $n = 4$, - - - - : $n = 6$, : $n = 8$, : $n = 10$	92
Figure 56b.	C_{IL} versus t/T , (Close-up of Figure 56).....	92
Figure 57a.	C_d and C_m , versus K , C_d : for $n = 2$ (open circles), C_d : for $n = 8$ (full circles), C_m : for $n = 2$ (open squares), C_m : for $n = 8$ (full squares)	93
Figure 57b.	C_{IL} and C_L , versus K , C_{IL} : for $n = 2$ (open circles), C_{IL} : for $n = 8$ (full circles), C_L : for $n = 2$ (open squares), C_L : for $n = 8$ (full squares).....	93
Figure 58a.	C_{IL} versus t/T , $K = 3$, $\beta = 196$, $\Delta\alpha = 0.5$ (open circles), $\Delta\alpha = 5.0$ (full circles)	94
Figure 58b.	C_L versus t/T , $K = 3$, $\beta = 196$, $\Delta\alpha = 0.5$ (open circles), $\Delta\alpha = 5.0$ (full circles)	94
Figure 59a.	C_{IL} versus t/T , $K = 4$, $\beta = 196$, $\Delta\alpha = 0.5$ (open circles), $\Delta\alpha = 5.0$ (full circles)	95
Figure 59b.	C_L versus t/T , $K = 4$, $\beta = 196$, $\Delta\alpha = 0.5$ (open circles), $\Delta\alpha = 5.0$ (full circles)	95

Figure 60.	C_{IL} versus t/T , $K=1$, with CRAY, $\beta = 450$, $\Delta t = 0.002$ (+), $\Delta t = 0.0001$ (full circles)	96
Figure 61a.	C_{IL} versus t/T , $K=4$, $\beta = 196$, $\Delta t = 0.002$ (open circles), $\Delta t=0.0005$ (full circles).....	97
Figure 61b.	C_L versus t/T , $K=4$, $\beta = 196$, — : $\Delta t = 0.002$, : $\Delta t = 0.0005$	97
Figure 62.	Streaklines, $K = 4$, $\beta = 196$, $\Delta t = 0.0005$, $t/T = 4$	98
Figure 63	Streaklines, $K = 4$, $\beta = 196$, $\Delta t = 0.0005$, $t/T = 8$	99
Figure 64.	Streaklines, $K = 4$, $\beta = 196$, $\Delta t = 0.0005$, $t/T = 12$	100
Figure 65.	C_{IL} versus t/T , $K = 4$, $\beta = 196$, $\Delta t = 0.002$, $t/T = 24$	101
Figure 66.	C_L versus t/T , $K = 4$, $\beta = 196$, $\Delta t = 0.002$, $t/T = 24$	101
Figure 67.	Streaklines, $K = 4$, $\beta = 196$, $\Delta t = 0.002$, $t/T = 24$	102
Figure 68.	Streamlines (Relative Motion Ψ), $K = 1$, $\beta = 196$, $t/T = 7.00$	103
Figure 69.	Streamlines (Relative Motion Ψ), $K = 1$, $\beta = 196$, $t/T = 7.25$	104
Figure 70.	Streamlines (Relative Motion Ψ), $K = 1$, $\beta = 196$, $t/T = 7.50$	105
Figure 71.	Streamlines (Relative Motion Ψ), $K = 1$, $\beta = 196$, $t/T = 7.75$	106
Figure 72.	Streamlines (Relative Motion Ψ), $K = 1$, $\beta = 196$, $t/T = 8.00$	107
Figure 73.	C_L versus t/T , $V_r = 0.4$ $K = 4$, $\beta = 196$	108
Figure 74.	C_{IL} versus t/T , $V_r = 0.4$ $K = 4$, $\beta = 196$	108
Figure 75.	Streaklines, $K = 4$, $\beta = 196$, $t/T = 8$	109
Figure 76.	C_L versus t/T , $V_r = 0.6$, $K = 4$, $\beta = 196$	110
Figure 77.	C_{IL} versus t/T , $V_r = 0.6$, $K = 4$, $\beta = 196$	110
Figure 78.	Streaklines, $V_r = 0.6$, $K = 4$, $\beta = 196$, $t/T = 8$	111

Figure 79.	C_L versus t/T , $V_r = 0.8$, $K = 4$, $\beta = 196$	112
Figure 80.	C_{IL} versus t/T , $V_r = 0.8$, $K = 4$, $\beta = 196$	112
Figure 81.	Streaklines, $V_r = 0.8$, $K = 4$, $\beta = 196$, $t/T = 8-1/8$	113
Figure 82.	Streaklines, $V_r = 0.8$, $K = 4$, $\beta = 196$, $t/T = 8-2/8$	114
Figure 83.	Streaklines, $V_r = 0.8$, $K = 4$, $\beta = 196$, $t/T = 8-3/8$	115
Figure 84.	Streaklines, $V_r = 0.8$, $K = 4$, $\beta = 196$, $t/T = 8-4/8$	116
Figure 85.	Streaklines, $V_r = 0.8$, $K = 4$, $\beta = 196$, $t/T = 8-5/8$	117
Figure 86.	Streaklines, $V_r = 0.8$, $K = 4$, $\beta = 196$, $t/T = 8-6/8$	118
Figure 87.	Streaklines, $V_r = 0.8$, $K = 4$, $\beta = 196$, $t/T = 8-7/8$	119
Figure 88.	Streaklines, $V_r = 0.8$, $K = 4$, $\beta = 196$, $t/T = 9$	120
Figure 89.	C_L versus t/T , $V_r = 1.0$, $K = 4$, $\beta = 196$	121
Figure 90.	C_{IL} versus t/T , $V_r = 1.0$, $K = 4$, $\beta = 196$	121
Figure 91.	Streaklines, $V_r = 1.0$, $K = 4$, $\beta = 196$, $t/T = 8$	122
Figure 92.	C_L versus t/T , $V_r = 1.1$, $K = 4$, $\beta = 196$	123
Figure 93.	C_{IL} versus t/T , $V_r = 1.1$, $K = 4$, $\beta = 196$	123
Figure 94.	Streaklines, $V_r = 1.1$, $K = 4$, $\beta = 196$, $t/T = 8$	124
Figure 95.	C_{IL} and C_L versus V_r , $K = 4$, $\beta = 196$, $n = 2$ C_{IL} (open circles), C_L (full squares)	125
Figure 96.	C_{IL} and C_L versus V_r , $K = 4$, $\beta = 196$, $n = 8$ C_{IL} (open circles), C_L (full squares)	125
Figure 97.	C_d and C_m versus V_r , $K = 4$, $\beta = 196$, $n = 8$, C_d numerical (full circles), C_m numerical (full squares) C_d experiment (open circles), C_m experiment (open squares)	126
Figure 98.	Flow Visualization for $K = 4$, $V_r = 0.8$, $t = 8-3/8$	127
Figure 99.	Flow Visualization for $K = 4$, $V_r = 0.8$, $t = 8-4/8$	128
Figure 100.	Flow Visualization for $K = 4$, $V_r = 0.8$, $t = 8-5/8$	129
Figure 101.	Flow Visualization for $K = 4$, $V_r = 0.8$, $t = 8-6/8$	130
Figure 102.	Flow Visualization for $K = 4$, $V_r = 0.8$, $t = 8-7/8$	131

LIST OF SYMBOLS

A	= amplitude of sinusoidal oscillations
A_p	= acceleration parameter = $1/(S/R) = D (dU/dt)/V^2$
A_{pn}	= $D^n (d^n U/dt^n)/V^{n+1}$
a	= transformation parameter
C_{IL}	= inline force coefficient
C_L	= transverse force coefficient
C_d^u	= Fourier-averaged drag coefficient
C_m	= inertia coefficient = $1 + k_{ij}^u$
D	= diameter
F_{IL}	= inline force
F_L	= transverse force
K	= Keulegan-Carpenter Number = $U_m T/D$
K^+	= K by current = $K(1 + U_o/U_m) = K + U_o T/D$
k_{ij}^u	= Fourier-averaged added mass coefficient
n	= order of polynomial (see Eq 17)
p_s	= pressure on cylinder
p_∞	= pressure at outer boundary

\bar{p}_s	= pressure coefficient = $(p_s - p_\infty) / \rho U_\infty^2$
R	= cylinder radius
Re	= Reynolds number VU/ν , or $U_m D/\nu$
Re^+	= Re modified by current = $Re(1 + U_o/U_m) = Re + U_o D/\nu$
r	= radial distance
S	= displacement of fluid
S/R	= relative displacement of fluid
T	= period of oscillations
t	= time
t_v	= time at end of acceleration period
U	= time dependent velocity
U_m	= maximum velocity in pure sinusoidal flow
U_o	= collinear steady current velocity
V	= constant velocity reached at the end of the acceleration period
V_r	= current ratio = U_o/U_m
β	= $D^2/\nu T = Re/K$
$\Delta\alpha$	= disturbance oscillation applied to the ambient flow, (in degrees)
$\Delta\xi$	= computational grid spacing

- Ω = relative displacement of fluid during the acceleration period
 $= (S/R)_v = 0.5 (dU/dt) t_v^2 / R = 0.5 V t_v / (R)$
- μ = dynamic viscosity
- ν = kinematic viscosity
- ρ = density
- θ = angular position
- ψ = stream function
- ω = vorticity

ACKNOWLEDGMENTS

For his support and guidance both as teacher and friend I express my greatest appreciation to Distinguished Professor T. Sarpkaya. He has not only introduced me to "The Wind and Beyond", but taught me how and given me the desire to get there.

Many others have given me help along the way. When we discovered interesting flow characteristics in the numerical experiments and desired physical experimental verification, Mr. Jack McKay quickly completed the flow visualization apparatus. Dave Marco and Tony Circelli have given me tremendous support using the ME and AERO computer labs. John Ekaterinaris and Dr. Kwok of NASA provided the avenue for use of the CRAY supercomputers. LT Kent Fredrickson initially got the computer program running and conducted the first runs upon which I built. Professor Dalton and Dr. Xuegeng Wang supplied the initial program. For each of these people I have the deepest gratitude for this work would not have been possible without their help.

Finally my loving appreciation goes to both my daughter and wife for their continual support and understanding.

I. INTRODUCTION

Numerical experimentation in fluid dynamics, through the use of finite-difference, finite-element, and discrete-vortex methods, has attracted considerable attention during the past two decades and produced laminar flows difficult to measure and turbulent flows hard to verify and impossible to generalize. The reasons for this are relatively simple. Numerical solutions based on the full Navier-Stokes equations are not stable at high Reynolds numbers and the instability is non-linearly related to the particular flow, input parameters and the discretization conditions. Also, the real flow at the computed Reynolds numbers may be turbulent, at least in some regions of the flow, and the numerical experiment does not imitate the physical experiment. Furthermore, the observed physical and numerical instabilities do not necessarily correspond to each other. Assuming that the calculations for a given flow are carried out at sufficiently small Reynolds numbers, where the flow is known to remain stable and laminar, one quickly discovers that it is practically impossible to measure, to any credible degree of accuracy, most or all of the predicted quantities (except the Strouhal number and the photographs of the flow patterns). One may also raise the question as to whether the two-dimensional numerical calculations could or should ever be compared with physical experiments attempting to mimic two dimensionality through the use of various passive or active devices (e.g., end plates on cylinders).

Evidently, one's view of the state of the numerical modelling depends to a large extent on one's objectives. For example, if the objective is to obtain

some approximate answers and flow kinematics, one might be perfectly satisfied with the existing codes. If the objective is to match the measured and calculated results (e.g., lift and drag coefficients), one might achieve the desired objective by fine tuning a number of model parameters (e.g., the order of approximation of the velocity and/or vorticity gradients, particularly near the wall, mesh size, time step, type of discretization, outer boundary, just to name a few). If one's objectives are to perform numerical experiments for sake of numerical experiments, with no concern with the compatibility of the numerical and experimental results, then one can objectively asses the model instead of attempting to attribute to it artificial powers of prediction.

As far as the turbulent flows are concerned, some or all of the predictions of the numerical calculations for a given flow depend on the closure model used. Some models do better than others for some flows and worse than others for other flows. No model, however sophisticated, has a corner on the numerical market. Among the numerous theoretical, numerical, and experimental investigations, impulsively-started steady flow about a circular cylinder has occupied a prominent place partly because of its intrinsic interest towards the understanding of the evolution of separation, vortex formation, growth, and partly because it provided the most fundamental case for the comparison and validation of various numerical methods and codes. In recent years, attention has turned to a broader class of relatively manageable time-dependent flows about bluff bodies: Non-impulsively-started flows, sinusoidally oscillating flows, co-existing flows (uniform flow plus oscillating flow), flow from one steady state to another (at a lower or higher Reynolds number through the use of prescribed changes in velocity), and so on. The

solution of these problems at sufficiently high Reynolds numbers will have far reaching theoretical and practical consequences. As noted above, this is not yet the case, and the solutions must necessarily be confined to cases where the accurate prediction of physical experiments and the instant gratification are not the real objectives. However, it is hoped that even the approximate solutions will have enough information to elucidate the physics of the phenomenon.

It is clear from the foregoing that the objectives of the present investigation are to carry out extensive sensitivity analysis on a given code, based on the very popular vorticity/stream-function formulation of the Navier-Stokes equations, through the use of a circular cylinder immersed in an impulsively-started flow, in a non-impulsively started flow, in a sinusoidally-oscillating flow, and in a co-existing flow (current plus sinusoidal oscillations). The expectations are that the results will point out the strengths and weaknesses of the code, for the particular type of formulation used, explain the reasons between the various numerical predictions of the same problem, and, hopefully, shed some light on the physics of flows heretofore uncalculated.

II. BACKGROUND STUDIES

Numerous numerical experiments have been performed on flow about circular cylinders in an attempt to predict the Strouhal number, the pressure distribution, and the evolution of the lift and drag forces in impulsively-started steady ambient flow. Here, only the more recent and relatively more accurate examples will be described briefly. Ta Phuoc Loc (1980) solved the complete unsteady Navier-Stokes equation in vorticity/stream-function form using a combination of second and fourth-order compact finite-difference schemes. He obtained short-time symmetric-wake solutions at Reynolds numbers of 300, 550, and 1,000 and achieved good agreement with flow visualization results for both vortex size and center position. His calculations also showed clearly the small secondary vortices just behind the separation points.

Lecointe and Piquet (1984) used several compact schemes with the Navier-Stokes vorticity/stream function formulation to solve laminar flows around circular cylinders up to a Reynolds number of 9500. They studied both start-up and unsteady periodic phenomena. The predicted wake-region shape showed good agreement with experimental flow visualizations. Ta Phuoc Loc and Bouard (1985) performed calculations at $Re = 3,000$ and $9,500$ using a fourth-order finite-difference technique to solve the Poisson equation for the stream function and a second-order technique for the vorticity-transport equation. They found good agreement between their predictions and flow visualization. The calculations were confined, out of necessity, to relatively short times during which the wake became neither asymmetrical

nor turbulent. Chamberlain (1987) used a second-order fast Poisson solver based on FFT methods and found an accurate solution which agreed well with the previous numerical and physical experiments. Rumsey (1988) used an upwind-biased implicit approximate factorization algorithm to calculate the impulsively-started unsteady flow over a circular cylinder at a Reynolds number 1200 and a Mach number of 0.3. Rumsey's results were in very good agreement with the previous calculations and showed, predictably enough, only a slight compressibility effect.

All numerical calculations using finite-difference, finite-element, or vortex-element methods {see e.g., Sarpkaya and Shoaff (1979), van der Vegt (1988), Sarpkaya (1989), Chang and Chern (1990)} have assumed an impulsively-started flow. No computational attempt was made to investigate the effect of the initial acceleration, prior to the establishment of a steady uniform flow, on the characteristics of the resulting time-dependent flow.

Several experimental investigations {Bouard and Coutanceau (1980), Sarpkaya (1966), and Sarpkaya (1978)} of impulsively-started flow around circular and rectangular cylinders have been carried out. Bouard and Coutanceau (1980) investigated the shape and growth rate of the wake region behind the cylinder for Reynolds number between 40 and 10,000. Sarpkaya (1966, 1978) examined the evolution of the wake region and the development of the lift and drag forces with time for cylinders between Reynolds numbers of 15,000 and 120,000. Nagata et al. (1985) studied the start-up flow at Reynolds numbers between 250 and 1200, with the majority of the experiments performed at $Re = 1200$. They gave detailed results for the time-evolution of the vortical region, boundary-layer parameters, and profile shapes at this

Reynolds number. Sarpkaya and Kline (1982) examined the impulsively-started flow about four types of bluff bodies. Sarpkaya and Ihrig (1986) performed experiments and vortex-element analysis of impulsively-started flow about rectangular prisms and pointed out emphatically that other than numerical experiments, there is no mechanical system which is capable of generating a truly impulsive flow. In fact, efforts to generate impulsive or uniformly-accelerated flow at high Reynolds numbers may be hampered by the generation of compression and rarefaction waves and regions of intense cavitation (in liquids).

A finite difference analysis of the Navier-Stokes equations for a sinusoidally-oscillating ambient flow about a circular cylinder at K (Keulegan-Carpenter Number) = $U_m T/D = 5$ ($Re = 1000$) and $K = 7$ ($Re = 700$) has been attempted by Baba & Miyata (1987). Their results have shown that the calculations can be carried out only for short times (less than two cycles of flow oscillation) with a non-super computer. Murashige, Hinatsu and Kinoshita (1989) have used a similar method to analyze three cases ($K = 5, 7$, and 10) at higher Reynolds numbers around 10^4 . The flow was perturbed by artificial means to trigger an asymmetry. At $K = 10$, a transverse vortex street appeared, in agreement with experimental observations. Mostafa (1987), using multi-discrete vortices (with core), simulated the sinusoidally oscillating flow about a circular cylinder and the decelerating flow about cambered plates. His calculations for $K = 12$ have reproduced correctly and for the first time the transverse vortex street observed experimentally. However, the calculated forces were somewhat larger than those measured. The numerical simulation of steady flow past a circular cylinder undergoing in-

line and/or transverse oscillations through the use of two-dimensional unsteady Navier-Stokes equations was undertaken by Lecointe et al. (1987) for relatively small amplitudes ($A/D = 0.13$). Justesen (1991) recently presented results obtained from a numerical solution to a stream function-vorticity formulation of the Navier-Stokes equations for the flow around a circular cylinder in planar oscillating flow at small Keulegan-Carpenter numbers in the subcritical Reynolds number range. Justesen introduced a straining parameter "a" in order to better resolve the large gradients near the cylinder surface. This is in addition to the logarithmic straining, commonly used as part of the transformations, for a better resolution of the gradients near the body. Evidently, Justesen's transformation for $a = 0$ defaults to the logarithmic straining. However, "a" becomes another disposable parameter, dependent on at least K and Re . Justesen had to choose judiciously the value of the straining parameter for each K in order achieve drag and inertia coefficients in satisfactory agreement with those obtained experimentally. A systematic numerical variation of the governing parameters for an arbitrary $U(t)$ is extremely difficult.

III. NUMERICAL REPRESENTATION

A. COMPUTATIONAL METHOD

Here only a brief description of the computational method is presented. A more in depth description is given by Wang (1989).

The fluid is assumed to be two-dimensional, incompressible and viscous. The governing equations for the solution are the Navier-Stokes equations, with the stream function and the vorticity as independent variables. To achieve a higher density of mesh points near the cylinder surface, the computational domain is transformed from the physical plane (polar coordinates, see Fig. 1) to a rectangular plane (Fig. 2). In the rectangular plane, the mesh is maintained at a uniform grid spacing. It is necessary to have more mesh points closer to the cylinder surface because in this region the gradients of both the vorticity and the stream function are the largest.

A third-order in time, second-order in space, three-level predictor-corrector finite-difference scheme is used to solve the vorticity-transport equation. A Fast Poisson Solver based on the High Order Difference approximation with Identity Expansion (HODIE) and the Fast Fourier Transformation (FFT) provided by the IMSL mathematics library is used to solve for the stream function.

The unsteady Navier-Stokes equations in the polar coordinates, as defined by the vorticity transport equation and the vorticity/stream-function equation are,

$$\frac{\partial \omega}{\partial t} - \frac{1}{r} \left[\frac{\partial}{\partial r} \left(\omega \frac{\partial \psi}{\partial \theta} \right) - \frac{\partial}{\partial \theta} \left(\omega \frac{\partial \psi}{\partial r} \right) \right] = \nu \nabla^2 \omega \quad (1)$$

and

$$\nabla^2 \psi = \omega \quad (2)$$

where

$$\nabla^2 = \frac{\partial^2}{\partial r^2} + \frac{1}{r} \frac{\partial}{\partial r} + \frac{1}{r^2} \frac{\partial^2}{\partial \theta^2} \quad (3)$$

ω and ψ are the vorticity and the stream function, ν is the kinematic viscosity, t is the time and, r and θ are polar coordinates directions (see Figure 1). The velocity components in the r and θ directions are defined by

$$u = -\frac{1}{r} \frac{\partial \psi}{\partial \theta} \quad \text{and} \quad v = \frac{\partial \psi}{\partial r} \quad (4)$$

The boundary conditions for the physical problem are:

(1) no slip and zero normal velocity on the surface of the cylinder

$$\psi = \frac{\partial \psi}{\partial r} = 0 \quad \text{on} \quad r = R \quad (5)$$

and (2) the potential flow at infinity is defined as

$$\psi = U \left(r - \frac{R}{r} \right) \sin \theta \quad (6)$$

and

$$\omega = 0 \quad \text{at} \quad r = \infty$$

where U is the external flow and R is the radius of the cylinder.

The coordinate transformations required to go from the physical domain to the computational domain are:

$$r = R \exp(a\xi) \quad \text{and} \quad \theta = a\eta \quad (7)$$

where R is the radius of the cylinder and ' a ' is a transformation parameter.

The transformation of the non-dimensionalized vorticity-stream function equations and their finite difference form through the use of the central difference approximation for vorticity and a two-step, three-level, predictor-corrector scheme, with a third order accuracy in time, are described in detail in Wang (1989) and in Fredrickson (1990) and will not be repeated here.

B. CALCULATION OF THE FORCE COEFFICIENTS

The in-line and transverse force coefficients are determined from the combined contributions of the shear and pressure forces acting on the cylinder. The viscous forces are calculated from $\tau_s = \mu\omega$. The total in-line force then reduces to

$$F_{IL} = -\int_0^{2\pi} p_s \cos(\theta) R d\theta - \int_0^{2\pi} \mu\omega \sin(\omega) R d\theta \quad (8)$$

and the total lift force as

$$F_L = -\int_0^{2\pi} p_s \sin(\theta) R d\theta - \int_0^{2\pi} \mu\omega \cos(\omega) R d\theta \quad (9)$$

After dividing the in-line and the lift-force equations by $(0.5 \rho U^2 D)$ and defining

$$\bar{p}_s = \frac{2(p_s - p_\infty)}{\rho U_\infty^2} \quad (10)$$

the force coefficients reduce to

$$C_{IL} = -\frac{1}{2} \int_0^{2\pi} \bar{p}_s \cos(\theta) R d\theta - \frac{2}{Re} \int_0^{2\pi} \mu \bar{\omega} \sin(\omega) R d\theta \quad (11)$$

and

$$C_L = -\frac{1}{2} \int_0^{2\pi} \bar{p}_s \sin(\theta) R d\theta - \frac{2}{Re} \int_0^{2\pi} \mu \bar{\omega} \cos(\omega) R d\theta \quad (12)$$

The pressure coefficient is determined from the Navier-Stokes equations in terms of dimensionless vorticity. Once integrated with respect to θ , one has

$$\bar{p}_s(\theta) = \bar{p}_s(0) + \frac{4}{Re} \int_0^{2\pi} \left(\frac{\partial \bar{\omega}}{\partial \bar{r}} \right)_{r=1} d\theta \quad (13)$$

Equation (13) is substituted into equations (11) and (12) to determine the numerical scheme for the in-line and transverse force coefficients,

$$C_{IL} = -\frac{2}{Re} \int_0^{2\pi} \left\{ \left[\int_0^\theta \left(\frac{\partial \bar{\omega}}{\partial \bar{r}} \right)_{r=1} d\theta \right] \cos(\theta) + \bar{\omega} \sin(\theta) d\theta \right\} d\theta \quad (14)$$

and

$$C_L = -\frac{2}{Re} \int_0^{2\pi} \left\{ \left[\int_0^\theta \left(\frac{\partial \bar{\omega}}{\partial \bar{r}} \right)_{r=1} d\theta \right] \sin(\theta) + \bar{\omega} \cos(\theta) d\theta \right\} d\theta \quad (15)$$

The radial derivative of the vorticity on the surface of the cylinder, appearing in Equations (14) and (15), is determined through the use of discrete pointwise approximations of various orders, ranging from second to tenth order. For a second order approximation, one has

$$\left(\frac{\partial \bar{\omega}_i}{\partial \bar{r}} \right)_{r=1} = \frac{-3\omega_i + 4\omega_{i+1} - \omega_{i+2}}{2\Delta\xi} + O(\Delta\xi^2) \quad (16)$$

For higher order polynomials Equation (16) may be written as

$$\left(\frac{\partial \bar{\omega}_i}{\partial \bar{r}} \right)_{r=1} = \frac{A\omega_i + B\omega_{i+1} + C\omega_{i+2} + D\omega_{i+3} + E\omega_{i+4} + \dots}{\Delta\xi} + O(\Delta\xi^n) \quad (17)$$

in which the coefficients A –K are given in Table 1 below.

Table 1: Coefficients of the Polynomial in Eq. (17)

	n=2	n=4	n=6	n=8	n=10
A	-3/2	-25/12	-49/20	-761/280	-7381/2520
B	2	4	6	8	10
C	-1/2	-3	-15/2	-14	-45/2
D		4/3	20/3	56/3	40
E		-1/4	-15/4	-35/2	-105/2
F			6/5	56/5	252/5
G			-1/6	-14/3	-35
H				8/7	120/7
I				-1/8	-45/8
J					10/9
K					-1/10

C. CALCULATION OF THE DRAG AND INERTIA COEFFICIENTS

If one were to associate the total force with a velocity-square-dependent drag force and an acceleration-dependent inertial force then the coefficient associated with the latter may be interpreted as some measure of the added mass. But one must bare in mind that such a decomposition is far from being unique.

It has been customary to express the fluid force acting on a body moving in a fluid otherwise at rest as

$$F(t) = \frac{1}{2} \rho C_d^u A_p \left| \{ (U_o + U(t)) \} \right| \{ (U_o + U(t)) \} + \rho k_{ij}^u \nabla \frac{dU(t)}{dt} \quad (18)$$

where U_o represents the steady velocity; $U(t)$, the time-dependent oscillations; C_d^u , the Fourier-averaged drag coefficient and k_{ij}^u , the Fourier-averaged added-mass coefficient. It is customary to use an inertia coefficient C_m for a fluid in motion about a body at rest through the use of $C_m = 1 + k_{ij}^u$.

The Fourier averages of the drag and added-mass coefficients over a period of T may be calculated by multiplying both sides of Equation (8) once with $U(t)$ and once with dU/dt to yield

$$C_d^u = \frac{2 \int_0^T F(t) U(t) dt}{\rho A_p \int_0^T \left| \{ (U_o + U(t)) \} \right| \{ (U_o + U(t)) \} U(t) dt} \quad (19)$$

and

$$(C_m - 1) = k_{11}^u = \frac{\int_0^T F(t) \frac{dU(t)}{dt} dt}{\rho \int_0^T [dU(t)/dt]^2 dt} \quad (20)$$

which may be evaluated readily provided that sufficiently reliable data are available for $F(t)$, U_0 , $U(t)$, and $dU(t)/dt$.

1. Governing Parameters

A simple dimensional analysis of the flow under consideration shows that the time-averaged force coefficients (C_d^u and k_{ij}^u) are functions of a relative amplitude or Keulegan-Carpenter number, Mach number, Reynolds number, and a parameter involving U_0 (e.g., $U_0 T/D$ or $U_0/[U(t)]_{\max}$). There are numerous possibilities regarding the definitions of the relative amplitude or Keulegan-Carpenter number and the Reynolds number. The purpose of the search for a more suitable Keulegan-Carpenter number and/or Reynolds number is to enhance the correlation of the data to reduce the number of the governing parameters, possibly eliminating $U_0 T/D$ as an independent parameter. The list of possible Reynolds numbers and Keulegan-Carpenter numbers is long and will not be given here. Suffice it to note that the two force-coefficients for the flow about a cylinder may be written as

$$\begin{matrix} C_d^u \\ k_{ij}^u \end{matrix} = f_i(K, Re, VK) \quad (21)$$

or as

$$C_d^u = f_i(K^+, Re^+, VK) \quad (22)$$
$$k_{ij}^u$$

in which

$$K = U_m T/D \quad , \quad Re = U_m D/\nu \quad , \quad VK = U_o T/D$$

$$K^+ = K(1 + U_o/U_m) = K + U_o T/D$$

$$Re^+ = Re(1 + U_o/U_m) = Re + U_o D/\nu \quad (23)$$

IV. DISCUSSION OF RESULTS

A. INTRODUCTION

The numerical experiments were carried out through the use of a VAX-2000, a VAX-3520, a CRAY Supercomputer and the IMSL library. The results will be discussed in terms of impulsively-started flows, non-impulsively started flows, oscillating flows, and co-existing flows (oscillation plus current), following a brief description of their general behavior.

The extensive literature that exists on unsteady flows about cylinders has either concentrated on the initial symmetric state or on the asymmetric late time vortex shedding. However, no systematic attempt was made to determine the upper limit of the early stages, the upper and lower limits of the intermediate indeterminable state, or the lower limit of the quasi-steady-state, in terms of the parameters characterizing the artificial disturbance imposed on the flow. It has long been recognized that the symmetric state becomes increasingly unstable and the flow sooner or later bifurcates into an asymmetric state. This bifurcation is not an instantaneous event but takes place rather gradually even if the disturbance is imposed suddenly. However, the interesting feature of all the numerical calculations is that the numerical noise and truncation errors are ever present and continue to work on the propensity of the flow to become naturally asymmetrical even though the results are far from being natural. Had one been able to devise a sufficiently accurate numerical scheme and a greater-precision computer, one could maintain a longer symmetric state. Evidently, the onset of asymmetry in

calculations depends on the characteristics of the physical disturbances. The two types of disturbances used can never be made identical, but they may be made to mimic each other. Thus, it is the hope of the numerical experimenter that the early stages of an impulsively started flow is relatively immune to truncation errors and the imposed, reasonable, artificial perturbation can, therefore, be expected to compare with the physical experiments. However, once the flow becomes asymmetrical the period of transition into a quasi-steady-state depends, to varying degrees of intensity, on the parameters characterizing the numerical disturbance. For small perturbations, the quasi-steady-state may eventually be arrived at smoothly without the in-line and transverse force coefficients overshooting first and then reducing to their terminal values. The rather unfortunate aspect of the numerical dilemma is that the quasi-steady-state is not just a function of the characteristics of the perturbation. If it were, one would have conducted a series of numerical experiments, arrived at a fairly stable state, and would have concluded that the flow no longer remembers how it was started and how it ever became asymmetrical. Even though this is the ultimate goal of the numerical experiments, the effects of the unavoidable truncation errors are ubiquitous and continue to influence, to varying degrees of importance, the entire history of the computed flow. At lower Reynolds numbers the history effects are relatively smaller and the flow remains essentially at a quasi-steady state once it arrives there.

It is in view of the realization of the foregoing facts that the results reported herein dealt with extensive sensitivity calculations to determine the effects of the type and intensity of the perturbations, the grid size, the time

increment, and the effect of the outer boundary of the computational domain on the numerical experiments.

B. CHARACTERIZATION OF PERTURBATIONS

The problem associated with the assignment of a perturbation is not the making of suitable choices among a limited number of equally sound characterizing parameters, but rather the difficulty of choosing a reasonable one from among an infinite set of perturbations and applying it at the right time interval. Faced with this problem, previous investigators used many types of artificial disturbances. In fact, there are as many original disturbances as there are original papers. In the present study, sinusoidal disturbances of varying intensities were used. The first application of such a disturbance was to change the direction of the ambient flow (one half a degree in either direction) one full sinusoidal cycle in the range of $3 < S/R < 5$ where S/R is the relative displacement of the fluid. The amplitude of the sine wave was the only free parameter. It is worth noting that the this type of disturbance gradually returns the perturbed quantity to its initial state (Fredrickson 1990). This type of disturbance was desired for the present model but required a long time to induce vortex shedding. Increasing the amplitude of the change of flow direction was not desirable. As Fredrickson showed, the resulting flow was greatly affected by the perturbation strength. A perturbation of the same form was used but introduced in the range $3 < S/R < 13$ for a duration of $\Delta(S/R) = 10$. Part of the reason for this selection was that it introduces an oscillation frequency that corresponds to a Strouhal number of 0.20, a frequency which is much closer to the natural frequency of the flow. Figure 3 shows, for example, that the disturbance introduced over $\Delta(S/R) = 10$, as

described above, induces vortex shedding sooner than the one introduced over $\Delta(S/R) = 2$ with an intensity ten times larger. Figure 4 shows the effect of the change of amplitude of the disturbance and the change of duration of the disturbance on the lift coefficient. Clearly, both parameters have interesting influences on the lift coefficient. A disturbance of small amplitude applied over a longer range ($3 < S/R < 13$) has far greater effect on the evolution of the lift than a disturbance ten times the amplitude applied over a shorter period ($3 < S/R < 5$). Finally, a very large disturbance applied over the longer period precipitates the lift buildup but the resulting amplitude of oscillation is nearly identical to that obtained with the smaller disturbance. It is because of these reasons that a disturbance of amplitude 0.5 degrees was introduced over the range $3 < S/R < 13$ throughout the calculations reported herein unless otherwise noted.

C. IMPULSIVE/NON-IMPULSIVE FLOW

Among the numerous theoretical, numerical, and experimental investigations, "impulsively-started" steady flow about a circular cylinder has occupied a prominent place partly because of its intrinsic interest towards the understanding of the evolution of separation, vortex formation, and growth, partly because of its practical importance in various aerodynamic applications (e.g., the impulsive flow analogy, flow about missiles, dynamic stall), and partly because it provided the most fundamental case for the comparison and validation of various numerical methods and codes. However, neither "impulsive start" nor "impulsive stop" is physically realizable. The flow must be accelerated from rest to a constant velocity or decelerated from a constant velocity to rest, or to another velocity, in a prescribed manner. This

fact gives rise to a series of new questions such as: (i) What is the effect of the initial acceleration, prior to the establishment of a steady uniform flow, on the characteristics of the resulting time-dependent flow? (ii) Are there critical values of the governing parameters above or below which the flow may be regarded as *almost* impulsively-started? (iii) How does the rate of accumulation of vorticity, as well as its cross-wake transfer, depend on the initial history of the motion? The purpose of this section is to explore some of these questions through the use of a series of numerical experiments. In doing so, however, one needs to introduce some new parameters such as

$$A_p = D (dU/dt)/V^2 \quad (24)$$

or

$$A_{pn} = D^n (d^n U/dt^n)/V^{n+1} \quad (25)$$

in order to account for the initial history of the fluid motion. The other parameters are the Reynolds number $Re = VD/\nu$ and the relative displacement of the ambient flow, given by

$$S/R = 0.5 (dU/dt) t^2/R = 0.5 V t^2/(Rt_v) \quad \text{for } t \leq t_v \quad (26)$$

and

$$S/R = 0.5 (V t_v/R) + (t - t_v) V/R \quad \text{for } t > t_v \quad (27)$$

and

$$(S/R)_v = \Omega = 0.5 (dU/dt) t_v^2/R = 0.5 V t_v/(R) \quad (28)$$

where U is the time-dependent velocity in the interval $(0 < t < t_v)$, V is the constant velocity arrived at the end of the **constant acceleration** period, R is the radius of the cylinder, t is the time, t_v is the duration of the acceleration

period, and $\Omega = (S/R)_v$ is the relative displacement of the fluid at the end of the acceleration period. A systematic physical and numerical experimentation for an arbitrary $U(t)$ is extremely difficult in view of the parameters involved. Thus, to make progress one must begin with the simplest unsteadiness, namely with constant dU/dt , so as to be able to incorporate progressively more complex variations of velocity with time.

As it will be discussed in detail later, there are important flow features between the impulsively and non-impulsively started flows. It is because of this reason that first the characteristics of impulsively-started flows will be discussed. Subsequently, the case of non-impulsively-started flow will be taken up. Finally, the limits of the governing parameters will be determined through a comparison of the corresponding pressure, vorticity, etc. plots.

D. IMPULSIVELY-STARTED FLOW

Among the numerous calculations performed, only two representative impulsive-flow situations will be discussed in some detail. Figures 5 through 7 show the drag coefficient, lift coefficient, and the streaklines for $\Omega = 0.10$, $Re = 1,000$, $\Delta t = 0.02$, and $\Delta \xi = 1/64$. A drag overshoot occurs at about $S/R = 3$ and is followed by a rapid decrease in C_d . Even though, the drag oscillations in the interval $40 < S/R < 60$ are representative of regular vortex shedding, the numerical instabilities and truncation errors take over at times larger than about 60 and the drag oscillations degenerate into unrealistic oscillations. Evidently, the use of a stream function/vorticity formulation for use at such relatively high Reynolds numbers is not quite warranted. In fact, it is to delineate the regions of stability of the numerical code that the calculations have been performed at such high Reynolds numbers.

In pursuit of understanding the limitations of the CODE , the calculations have been performed at three other Reynolds numbers. Figures 8 through 10 show the comparative evolution of the drag and lift coefficients for suitable relative motions. The drag coefficient for $Re = 500, 750,$ and $1,000$ are fairly similar and all exhibit secondary vortices. However, the case of $Re = 250$ is significantly different and the streamlines do not show secondary vortices. The reasons for this are not yet clear. The lift coefficient shows nearly similar behavior with small phase differences, as one would expect. Finally, Figures 11 (for $0 < S/R < 100$) and 12 (for $0 < S/R < 5$) show the effect of the order of the polynomial used in the calculation of the vorticity gradient on the wall.

E. NON-IMPULSIVELY-STARTED FLOW

These deal primarily with flows which are subjected to constant acceleration for a prescribed distance of Ω and then maintained at constant velocity throughout the remainder of the calculations. A detailed experimental investigation of such flows has been recently given by Sarpkaya (1990).

Figures 13–17 show typical in-line force, pressure distribution, streamlines, and the vorticity distribution for $\Omega = 1$ and $Re = 1,000$. Figure 15 shows the development of the primary and the secondary vortices at $S/R = 3$. Similar results are shown in Figs. 18–24 for $\Omega = 2$ at representative S/R values. The comparison of Figs. 16, 20 and 22 show that the larger the Ω , the larger the S/R at which the secondary vortices grow. Figures 25–32 and the Figures 33–37 show the evolution of non-impulsively started flows for $\Omega = 3$ and $\Omega = 10$ respectively. It is particularly noteworthy that the secondary vortices which appear at $S/R = 10$ (Fig. 35, the end of the acceleration period),

disappear shortly thereafter at $S/R = 10.2$ (Fig. 36) due to the instant transition of flow to a constant velocity and then reappear again at $S/R = 11.6$ (Fig. 37).

In general, the fundamental character of the non-impulsively-started flows may be best described in terms of the evolution of the secondary vortices. Although much of the same patterns are observed in the impulsive cases, the said phenomenon was studied much more extensively in the non-impulsive regime. As noted earlier, the time to the development of secondary vortices is longer and not so sudden. Figures 30 and 31, for example, shows the development of the streamlines just at the time the secondary vortices begin to appear. The streamlines before secondary vortex development are more sylph like behind the cylinder and bulge as the vorticity grows stronger. The secondary vortices are driven to form between the cylinder and the primary vortices. Once the initial acceleration is completed the secondary vortices are no longer impeded by the adverse pressure gradient and rapidly grow to a maximum size that corresponds to that seen in the numerical calculations of the post acceleration drag peak. This peak is not strong enough to be seen in the experiments and is probably unimportant other than for the understanding of the growth of a vortex subjected to acceleration for a specific period of time.

The appearance and disappearance of secondary vortices in Figures 35-37 is not surprising as one would expect them to appear sooner or later provided that the acceleration period is long enough for a given rate of acceleration. Although not pursued further, it is expected that for a sufficiently slow acceleration the secondary vortices would not at all appear (even disappear) after the constant velocity is reached. The disappearance of the secondary

vortices is attributable to the sudden pressure change behind the cylinder which drives the primary vortices back towards the cylinder increasing their strength and decreasing the secondary vortex strength.

The form of the drag overshoot is related to the development of the secondary vortices behind the cylinder. A careful examination of Figures 13-37 shows that even though a second drag overshoot occurs in each case, it becomes less perceptible at lower acceleration rates (higher Ω).

The Figures 13-32 also show that the impulsive versus non-impulsive case may be separated by an Ω value between 2 and 3. This is slightly lower than the value of 3.7 identified by Sarpkaya (1990) on the basis of his experiments at much higher Reynolds numbers. The pressure plots (see Figs. 19 and 26) show marked differences between these two values which may correlate with the drag overshoot in the experimental results. The plots at $\Omega = 3$ show that the form of the pressure is well established before the acceleration has ended and changes little thereafter. This is not the case for $\Omega = 2.0$ where there is a larger change in the form of the wall pressure after a constant velocity is reached. Figures 15, 20 and 28 show plots of the vorticity for Ω of 1.0, 2.0 and 3.0 at the end of the acceleration point confirm that the secondary vortices have developed much more for $\Omega = 3.0$ but hardly at all for the other two cases. Although these values do not correlate exactly with the experiments, their characteristic behavior seems to be the same. It is also interesting to note that the second drag overshoot is always accompanied by the first appearance of the secondary vortices in the streamline plots. This is probably purely coincidental as the vorticity plots exhibit full development by this stage and the vorticity is the actual contributory element to the drag. The

streamline plots merely show that the vorticity has become strong enough to be perceptible. Previously, it was thought that the post acceleration drag overshoot occurred as a result of the accumulation of excess vorticity in the primary vortices and the subsequent annihilation of vorticity in the overlapping regions of vorticity. The figures noted above suggest that not only the rapid accumulation of vorticity but also the evolution of the secondary vortices affect the actual drag overshoot. The overshoot occurring at higher Ω values in the numerical experiments are probably over shadowed by other phenomena in the experiments, particularly when the vortex shedding commences immediately after the acceleration is removed. For higher acceleration rates (lower Ω), the flow in physical experiments remains nearly symmetrical for a longer time period, allowing the secondary vortices to play their part. For the lower acceleration rates, however, the onset of vortex shedding destroys the secondary vortices before they can affect the evolution of the fluid resistance. The post acceleration drag overshoot for the slower accelerations in the numerical results is fairly small and is not likely to have much of an effect even if the experimental flow remained nearly symmetric.

F. OSCILLATING FLOWS

The efforts to arrive at coherent descriptions of the interactions between oceans and the structures inserted therein have a long history. The past two decades have seen an explosion of interest in the broad subject of ocean hydrodynamics. As a result of this activity, there is arising an improved and more realistic understanding of the physical characteristics of some time-dependent flows about bluff bodies and their mathematical formulation. On

the one hand attention has been focussed on controlled laboratory experiments which allow for the understanding of the separate effects of the governing and influencing parameters, and on the other hand on mathematical and numerical methods which allow for the nearly exact solution of some wave loading situations.

The hydrodynamic loading situations which are well understood are those which do not involve flow separation. Thus, they are amenable to nearly exact analytical treatment. These concern primarily the determination of the fluid forces on large objects in the diffraction regime where the characteristic dimension of the body relative to the wave length is larger than about 0.2. The use of various numerical techniques is sufficient to predict accurately the forces and moments acting on the body, provided that the viscous effects and the effects of separation for bodies with sharp edges are ignored as secondary.

The understanding of the fluid-structure interactions which involve extensive flow separation and dependence on numerous parameters such as Reynolds number, Keulegan-Carpenter number, relative roughness, relative motion of the body, proximity effects, hydroelastic response, etc. is far from complete (Sarpkaya & Isaacson 1981). There are several reasons for this. First, although the physical laws governing the motion (the Navier-Stokes equations) are well known, valid approximations necessary for numerical and physical model studies are still unknown. Even the unidirectional steady flow about a bluff body remains theoretically unresolved. Much of our understanding of vortex shedding behind bluff bodies came from steady-flow experiments, highly idealized models, and limited numerical solutions. Most

of the numerical studies based on the use of the Navier-Stokes equations and some suitable spatial and temporal differencing schemes are limited, out of necessity, to low Reynolds number flows. A second reason why progress has been slow is that the bluff body problems involving *wake return* are an order of magnitude more complex and there has been only a handful of limited applications of the methods based on Navier-Stokes equations, as noted in the introduction.

The formation of a wake gives rise not only to a form drag, as it would be the case if the motion were steady, but also to significant changes in the inertial forces. The velocity-dependent form drag is not the same as that for the steady flow of a viscous fluid, and the acceleration-dependent inertial resistance is not the same as that for an unseparated unsteady flow of an inviscid fluid. In other words, the drag and inertial forces are interdependent as well as time-dependent. These effects are further compounded by the diffusion and decay of vortices and by the three-dimensional nature of vorticity due to turbulent mixing, finite spanwise coherence, and the random nature of the vortices (which give rise to cycle-to-cycle variations and numerous flow modes even under controlled laboratory conditions). The stronger and better correlated the returning vortices, the sharper and more pronounced the changes are in pressure distribution on the body and in the integrated quantities such as the lift, drag, and inertia coefficients.

Figures 38 and 39 show dramatically the large changes that can occur over a very short time in a sinusoidally oscillating flow. The perturbation was applied during the first cycle of the oscillation. The remaining parameters

were $K = 1.5$, $Re = 450$, and $\beta = 300$. Figure 38 shows the streamlines at $t/T = 4$ and Fig. 39, at $t/T = 4.004$.

Figures 40 through 43 show the total streamlines for $K = 3$ and $\beta = 196$, at times $t/T = 6.0, 6.25, 6.5$, and 6.75 . Figures 44 through 47 show, for the same parameters and times, the differential streamlines, as seen by an observer moving with the cylinder, (i.e., the difference between the total stream function and the ambient potential function, corresponding to the purely sinusoidal flow). Even though it is not quite obvious, the flow at this particular K value becomes eventually asymmetrical.

Figures 48 through 51 show the total stream function values for $K = 4$ and $\beta = 196$, at times $t/T = 6.0, 6.25, 6.5$, and 6.75 , and the Figures 52-55 show the differential stream function values at the corresponding times. The last eight figures clearly show that the flow becomes asymmetrical and the vortex trajectories exhibit an exceedingly complex structure. Thus, it is clear that one would not be able to arrive at a simple description of the time-dependent flow and of the forces exerted on the body. It is also equally clear that an empirical equation, such as the so-called "Morison's equation" [see, Eq. (18) and Sarpkaya & Isaacson 1981] cannot adequately represent the measured or the calculated force in terms of two time-averaged coefficients. The fact that it comes close to doing so, at least in certain ranges of the Keulegan-Carpenter number, is a remarkable testimony to the strong influences of the drag and inertia components of the force, when one or the other tends to dominate the flow.

Figure 56a shows a comparison of the instantaneous in-line force for $K = 1.5$, $Re = 450$, and $\beta = 300$ for various orders of polynomial used to calculate

the vorticity gradient on the wall. It is clear that the force curves are quite similar and the order of the polynomial does not materially affect the amplitude of the total force. However, a closer perusal of Fig. 56a and a close-up plot of Fig. 56b show that the phase of the force relative to the ambient flow is shifted by a few degrees. This, seemingly insignificant phase shift becomes exceedingly important if one wishes to determine the parts of the force which may be attributed to the velocity-square dependent drag and the acceleration-dependent inertia [see Eqs. (19) and (20)]. This matter has been explored in greater depth through the use of orders of polynomial varying from 2 to 10. Table 2 shows the C_d and C_m values for $K = 1.5$, and $\beta = 300$ for $\Delta\xi = 1/64$ and $\Delta\xi = 1/128$ for various values of the exponent n .

Table 2 Dependence of C_d and C_m on the Wall-Vorticity Gradient

Order of polynomial	<u>$\Delta\xi = 1/64$</u>		<u>$\Delta\xi = 1/128$</u>	
	C_d	C_m	C_d	C_m
2	5.33	1.92	2.68	2.07
4	2.86	2.25	1.44	2.13
6	1.55	2.27	1.15	2.12
8	1.30	2.23	1.21	2.12
10	1.50	2.20	1.23	2.12

Experimental Values: $C_d = 1.15$ and $C_m = 2.12$

Table 2 shows that the drag and inertia coefficients may be made to agree with the experimental values through the judicious selection of the exponent n and the node spacing. However, this should not be taken to mean that the

same exponent will yield equally satisfactory agreement between the numerical and physical experiments. It turns out that one should seek other values of the exponent as in the case of Justesen (1991) (other values of the stretching parameter) to match the measured and calculated values of the drag and inertia coefficients. However, it is of some importance to note that the desire to separate the total in-line force into a drag and inertial force components is that of the investigator and not that of nature. Thus, small phase differences stemming from the influence of the exponent should not be taken to mean that the total force as a function of time will significantly depend on the exponent. In fact, as noted above, the calculated time-dependent force is quite similar for all values of the exponent. Thus, the results show that regardless of the method of discretization and other care a numerical scheme should not be expected to resolve all aspects of a given problem to the same degree of accuracy. Furthermore, the kind of accuracy depicted in Table 2 should not be expected and is not warranted through the use of a high-order polynomial since the rest of the discretization is accurate only to second order.

In order to test the power of precision of the use of the eight-order exponent obtained in the previous case, shown in Table 2, calculations have been performed at other K values. Figure 57a shows that at relatively small Keulegan-Carpenter numbers where the force is inertia-dominated, the inertia coefficient C_m is not significantly affected by the order of the polynomial. However, the drag coefficient is affected dramatically. Furthermore, what was an ideal value as an exponent for the $K = 1.5$ case turns out to be rather unsatisfactory for the other values of K (2, 3, and 4). In

fact Table 3 shows that the experimental values of the drag and inertia coefficients are bracketed by the values of $n = 2$ and $n = 8$.

Table 3 Dependence of C_d and C_m on the Exponent n .

	$K = 1$	$K = 2$	$K = 3$	$K = 4$
C_d (Theory [*])	1.95	0.95	0.70	
C_d (Exper. ⁺)		1.95	1.5	1.55
C_d ($n=2$)	5.96	3.3	2.56	2.26
C_d ($n=8$)	2.18	0.82	0.053	0.32
C_m (Theory [*])	2.16	2.16	2.16	
C_m (Exper. ⁺)		2.18	2.11	2.0
C_m ($n=8$)	2.05	2.01	1.9	1.74
C_m ($n=8$)	2.19	2.19	2.11	1.98

*Theory by Wang (1968), +Experiments (Bearman et al. 1985).

Thus, it is clear that the numerical schemes are not reliable enough to predict the precise phase shift between the ambient velocity and the maximum force. However, they are very reliable or robust enough as far as the total force coefficient is concerned. This result has been somewhat anticipated in the discussion of the previous works in connection with the numerical work

carried out by Justesen (1991) and his use of the so-called stretching parameter "a."

Figure 57b shows the amplitude of the time-dependent force for $K = 2, 3$, and 4. Apparently, the total-force coefficient does not measurably depend on the exponent, as noted earlier.

Figures 58a through 59b represent a study on the effect of the amplitude of disturbance on the in-line and transverse forces. Figures 58a and 58b show that a ten fold increase in the amplitude of the disturbance has very little influence on the said forces. Figure 59a also shows that the in-line force is practically unaffected but, as Fig. 59b shows, the transverse force undergoes amplitude and frequency modulations, dependent on the disturbance, primarily due to vortex shedding at higher K values.

Figure 60, obtainable only through the use of a super-computer because of time requirements, is an interesting comparison of the in-line forces calculated for $K = 1$ and $\beta = 196$ using two significantly different time intervals: $\Delta t = 0.002$ and $\Delta t = 0.0001$. Clearly, there is no perceptible difference between the two calculations. The drag and inertia coefficients for the two calculations are nearly identical, showing once again, at least for one K value, that they are more strongly influenced by the vorticity gradient on the wall than by the time increment and that the smallness of the time increment does not necessarily improve the drag coefficient or the vorticity gradient. A similar comparison for $K = 4$ and $\beta = 196$ is shown in Figs. 61a through 67 using $\Delta t = 0.0005$ and $\Delta t = 0.002$. It should be noted that the in-line force exhibits not only a mean Strouhal frequency but also its higher order harmonics. This may be due to the actual behavior of the flow at the stated K

and Re values or a consequence of the numerical instability, devoid of physics of the phenomenon. In any case, it demonstrates the consequences of the use of a supercomputer to either discover new phenomena or help define the limits of a model.

An additional study was undertaken to determine the onset of separation to the extent possible. Originally, it was surmised on the basis of experiments that the separation in sinusoidally oscillating flow sets in when K is equal to about 1.5. The recent numerical work of Justesen (1991) has shown that the separation is present and occurs at all K values. To this end, calculations were carried out with $K = 1$, $\beta = 196$, $\Delta t = 0.002$, and $\Delta \xi = 1/64$. The resulting relative streamlines are shown in Figs. 68 through 72 at suitable time intervals. Figure 68 shows the asymmetry of the flow and the development of two separation regions. In Fig. 70, the separation regions have shifted to the other half of the cylinder. However, the most interesting feature of these calculations is that the flow continues to evolve even after as many as seven cycles. For example, at $t/T = 8$, a Kelvin-oval like vortex pattern evolves. If the calculations were pursued to much larger times, additional regions of separation and stagnation points within the body of the fluid may have been observed. In any case, the fact which emerges from this study is that the lower limit of K observed experimentally is not the lowest K at which separation commences. It seems that $K = 1.5$ limit is an artifact of the experiments and most likely that of the surface tension and flow visualization techniques. Even though the calculations have not been carried out at K values smaller than one, there is every reason to believe that separation will occur at any K . This remains to be investigated in the future.

G. OSCILLATING FLOW WITH CURRENT

The in-line oscillations of a cylinder in uniform flow has been the subject of intense interest in recent years [see, e.g., Sarpkaya & Isaacson (1981) and Sarpkaya & Storm (1985)] in connection with the understanding of the behavior of hot-wire anemometers and the fluid loading of structures subjected to gusts and other types of unsteady flows. Evidently, the determination of the forces acting on a cylinder undergoing harmonic in-line oscillations is just as important as the understanding of its kinematics. The fact that there is a strong relationship between vortex shedding and the drag and inertia coefficients, one would anticipate that the biasing of the shedding of the vortices by the current will cause profound changes in both the drag and inertia coefficients, relative to their no-current values.

Numerical experiments have been carried out with $K = 4$, $\beta = 196$, $Re = 784$, $\Delta t = 0.002$ and various values of $V_r = U_o/U_m$ where $U = U_o + U_m \sin(2\pi t/T)$ and U_o is the collinear steady current velocity. Evidently, this is a rather limited exploration of a highly complex problem and requires much more numerical and experimental work. The purpose of the present calculations was not to provide a detailed comparison between the measured and calculated forces but rather to attempt to establish a relationship between the shedding of vortices and the relative magnitudes of the current. The particular value of K chosen for the calculations ($K = 4$) was one for which separation was known to occur and for which a few experimental data points were available at comparable β , Re , and V_r values.

Figures 73 through 94 show the evolution of the lift and in-line force coefficients as a function of t/T and the streaklines at $t/T = 8$ for $V_r = 0.4$ (Figs.

73-75), for $V_r = 0.6$ (Figs. 76-78), for $V_r = 0.8$ (Figs. 79-88), for $V_r = 1.0$ (Figs. 89-91), and for $V_r = 1.1$ (Figs. 92-94).

The streaklines show that the wakes are comprised of three rows of heterostrophic vortices. They differ only in detail from one V_r to another. At lower V_r values, where the sinusoidal oscillation is relatively important, the shedding of the vortex couples become more and more alternating. One pair goes to one side of the cylinder, next pair goes to the central street, and the third pair goes to the other side of the street. Then the events repeat themselves. At higher V_r values however, (see Figs. 81-88) the vortex pairs on both sides of the cylinder as well as those along the axis come into existence almost simultaneously. At still larger values of V_r (see Figs. 91 and 94 at $V_r = 1$ and 1.1 , respectively) the flow is dominated increasingly by the current. This leads to the alternate shedding of the vortex pairs which become situated along two off-axis lines. The central vortex pairs become very weak and fairly stretched out. The vortex pairs rotate and orient themselves as if they were going to be part of an ordinary Karman vortex street (see Fig. 91). Further downstream, the wake loses all traces of the oscillation and resembles that one created by a steady stream past a circular cylinder. The lift coefficient plots show the increasing asymmetry of the wake with V_r . At lower V_r values the in-line force coefficient remains essentially constant and periodic. At larger V_r values, however, the in-line force becomes not only asymmetrical but also highly dependent on the particular cycle under consideration. It appears that many more cycles of flow will have to be calculated to arrive at quasi-steady values of the in-line and transverse force coefficients.

Figures 95 through 97 show the maximum in-line force, drag, and inertia coefficients as a function of V_r . The only difference between the Figures 95 and 96 is that the former is calculated using a second order polynomial for the radial vorticity gradient, and the latter using an eighth order polynomial. A comparison of the two figures shows that there is very little difference between the two plots. In other words, the maximum in-line force coefficient is not sensitive to the order of the polynomial used, as noted earlier in connection with purely sinusoidal flows. Figure 97 shows a comparison of the calculated and experimental (Verley 1979) drag and inertia coefficients. The computed values were based on an eight order polynomial representation of the radial vorticity gradient. As expected, the inertia coefficients agree extremely well. As far as the drag coefficients are concerned, the agreement is not as good but certainly better than expected in view of the fact that the drag coefficient is dependent on the order of the polynomial used to calculate the vorticity gradient. Nevertheless, the trend of the data is well predicted. It was possible to carry out extensive numerical experiments to find the most appropriate value of the exponent n so as to achieve better agreement between the measured and calculated coefficients. However, this was deemed to be an unproductive effort since the purpose of the investigation was not an exercise in coefficient matching but rather the understanding of the kinematics of the flow and the role played by the vortices in time dependent flows. It is for this purpose that flow visualization experiments have been performed and some of the results will be described below briefly.

Figures 98 through 102 show the results of the flow visualization obtained with $K = 4$ and $V_r = 0.8$ at times $t/T = 8-3/8, 8-4/8, 8-5/8, 8-6/8$, and $8-7/8$. The symmetric growth and motion of the vortices are clearly visible. These figures should be compared with Figures 82-87. The similarities are rather striking in spite of the fact that β was 196 in the calculations and about 600 in the experiments. Figure 101 shows clearly not only the symmetrically developing vortices but also the heterostrophic pairs shed in the previous cycle.

V. CONCLUSIONS

The investigation reported here warranted the following conclusions:

1. Even the higher order finite difference formulations of the governing equations can be solved for only relatively small Reynolds numbers. This is partly due to stability and computer constraints, and in part due to the difficulty of specifying appropriate perturbations forcing the flow to bifurcate into an asymmetric quasi- steady-state.
2. For almost impulsively-started flows the drag overshoot occurs near $S/R=4$. For $(S/R)v>5$, this overshoot is obscured by the effect of acceleration and continues to increase the drag to values larger than the drag overshoot at $(S/R)v=4$.
4. The early stages of the flow, i.e. $S/R<15$ can be calculated within the limits of the accuracy of the computational scheme. The results are essentially independent of the characteristics of the perturbation even if they were imposed at the start of the motion.
5. The experimentally observed drag overshoot for almost- impulsively started flow occurs in the range $4<S/R<5$, depending on the noise imposed on the flow at the early stages of the motion.
6. There is a range of S/R values, for both impulsively and non-impulsively started flows, which is not amenable to correct numerical simulation. Because this region depends on the parameters characterizing the perturbations which are unknown and unknowable in physical experiments.
7. There is a third region of the flow in which the transient state evolves into a quasi-steady-state. It is assumed, for all intents and purposes that the flow does not remember how it arrived at the quasi-steady-state. It is tacitly assumed that the final state does not depend on the disturbances even though the nonlinear coupling of the disturbances and truncation errors may lead to somewhat different steady states.

8. The numerical experiments with sinusoidally oscillating flows yielded total force coefficients which were not only highly stable but also in agreement with those obtained experimentally.
9. The physical and numerical experiments yielded nearly identical; Inertia coefficients at the corresponding Keulegan-Carpenter numbers and Reynolds numbers regardless of the order of the polynomial used to calculate the radial gradient of the vorticity on the wall. However, the drag coefficient showed strong dependence on the exponent n because the small variations in phase lead to large changes in the instantaneous in-line force in the inertia-dominated regime of the oscillating flow.
10. The numerical experiments with co-existing flows (oscillation plus steady mean flow) produced extremely interesting flow features. For relative current velocities less than about one, the vortices shed nearly symmetrically at each cycle. For relative current velocities larger than about one, the vortex wake returned to the asymmetric mode, as is encountered in a regular Karman vortex street.
11. The calculations of resistance in co-existing flows have shown that the inertia as well as the drag coefficients (using an exponent of $n = 8$) for a Keulegan-Carpenter number of 4 are in surprisingly good agreement with those obtained experimentally at the corresponding relative current velocities.
12. Extensive flow visualization studies yielded vortex patterns in close agreement with those predicted numerically at the corresponding relative current velocities.
13. The foregoing numerical experiments could not have been possible had it not been due to the availability of a VAX-3520 and a CRAY supercomputer. It is also realized that calculations at higher Reynolds numbers and for larger numbers of cycles of flow oscillation will require extremely large CPU times even on a supercomputer.

APPENDIX

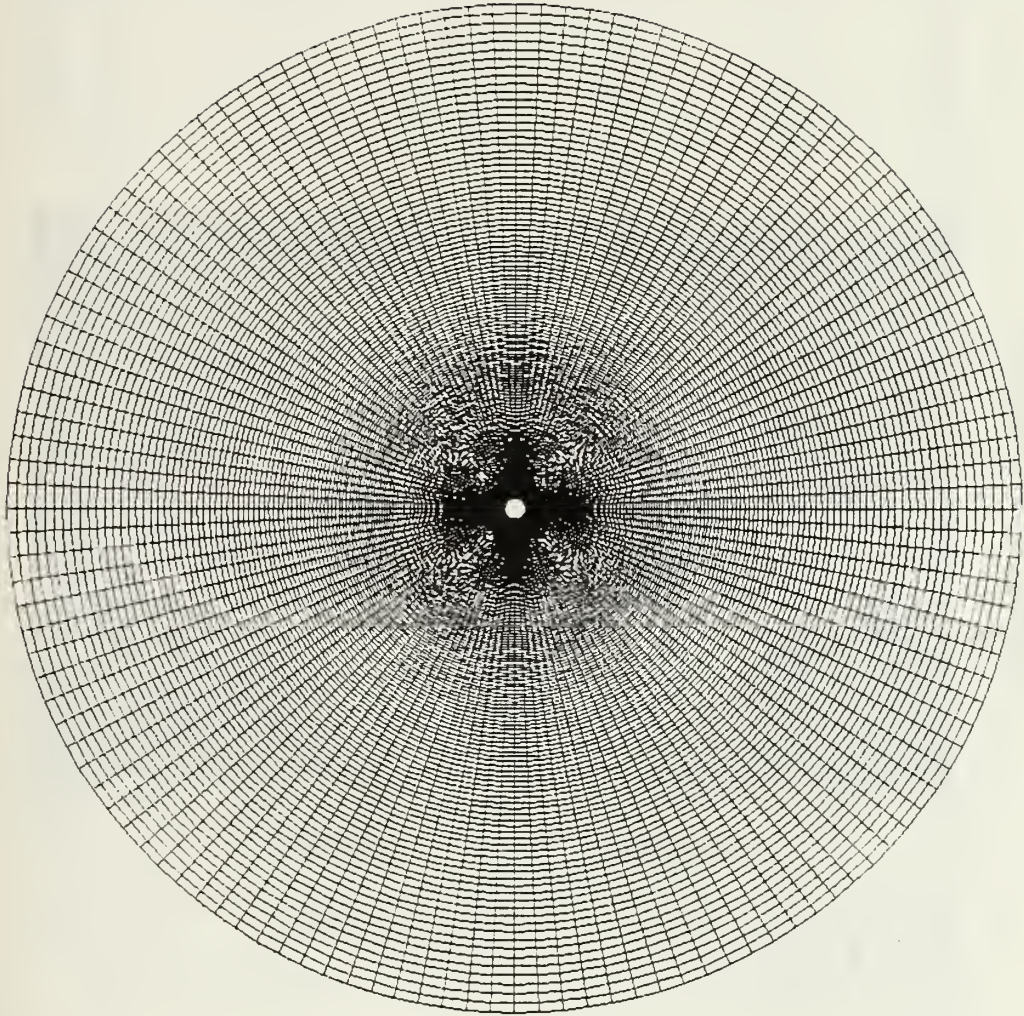


Figure 1. Grid in the Physical Domain

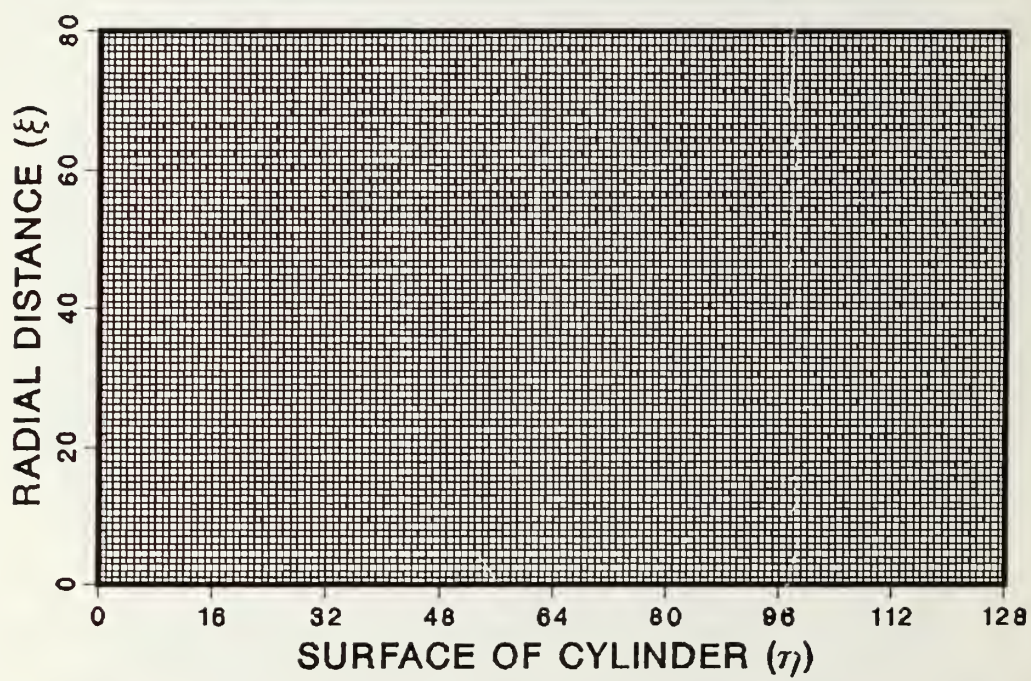


Figure 2. Grid in the Computational Domain

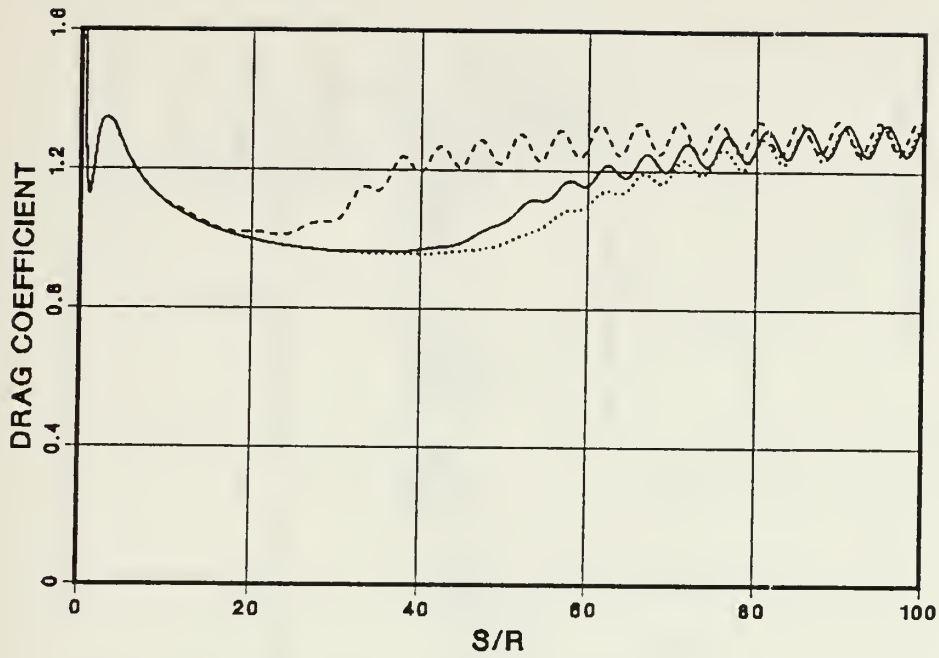


Figure 3. C_{IL} versus S/R , $Re = 200$, — : $\Delta\alpha = 0.5$ ($S/R = 3-10$),
 : $\Delta\alpha = 5.0$ ($S/R = 3-5$), - - - : $\Delta\alpha = 0.5$ ($S/R = 3-10$)

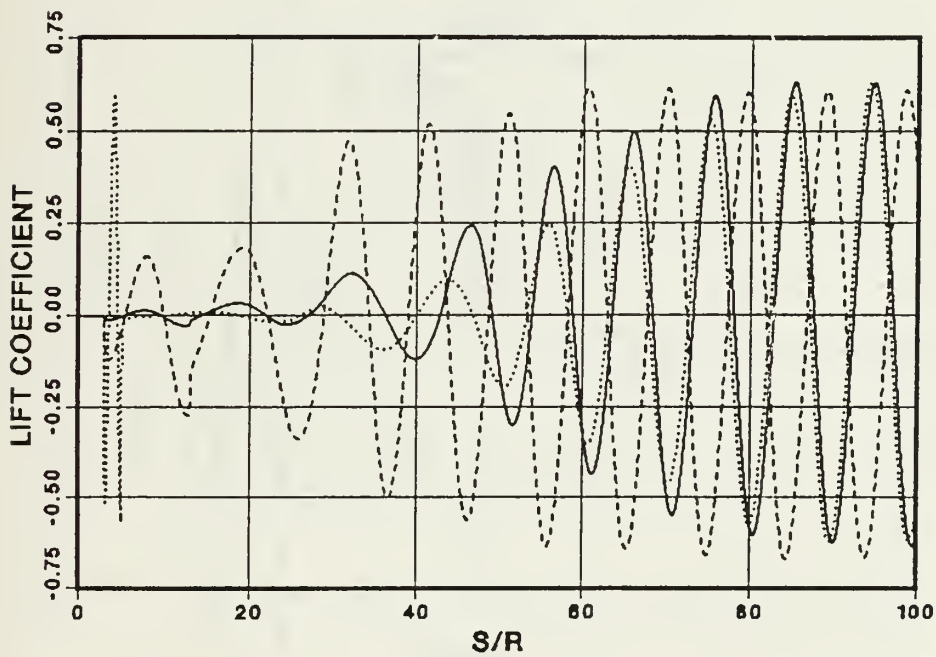


Figure 4. C_L versus S/R , $Re = 200$, (lines same as in Fig. 3)

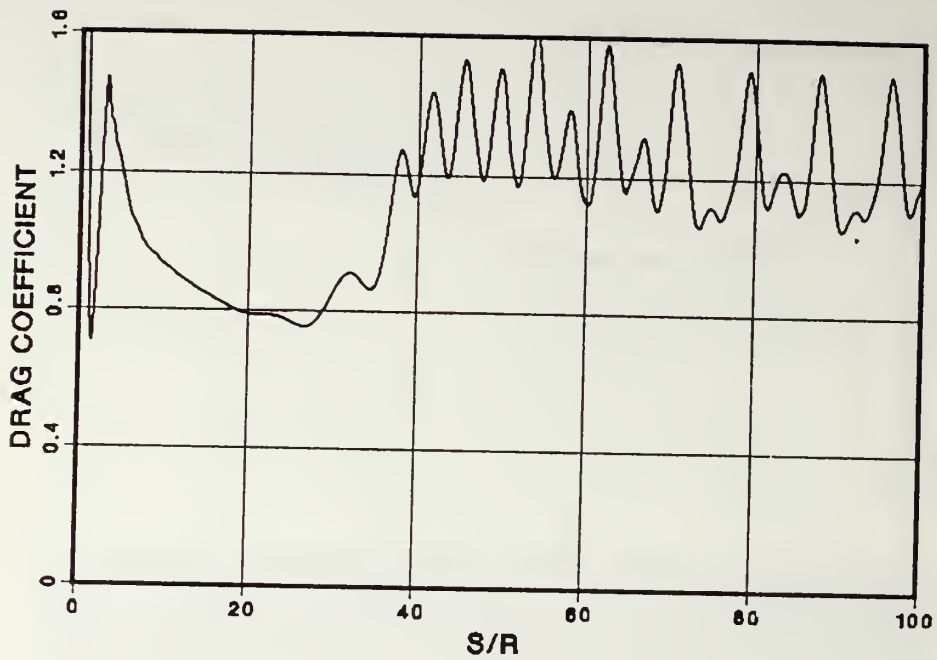


Figure 5. C_{IL} versus S/R , $\Omega = 0.1$, $Re = 1000$, $\Delta\xi = 1/64$

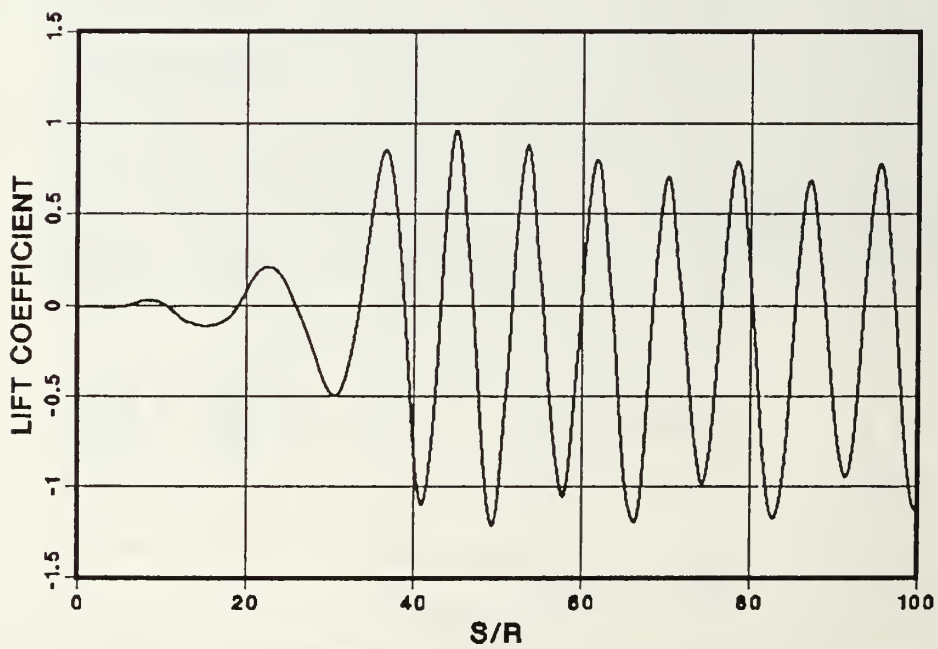


Figure 6. C_L versus S/R , $\Omega = 0.1$, $Re = 1000$, $\Delta\xi = 1/64$



Figure 7. Streaklines, $\Omega = 0.1$, $Re = 1000$, $\Delta\xi = 1/64$

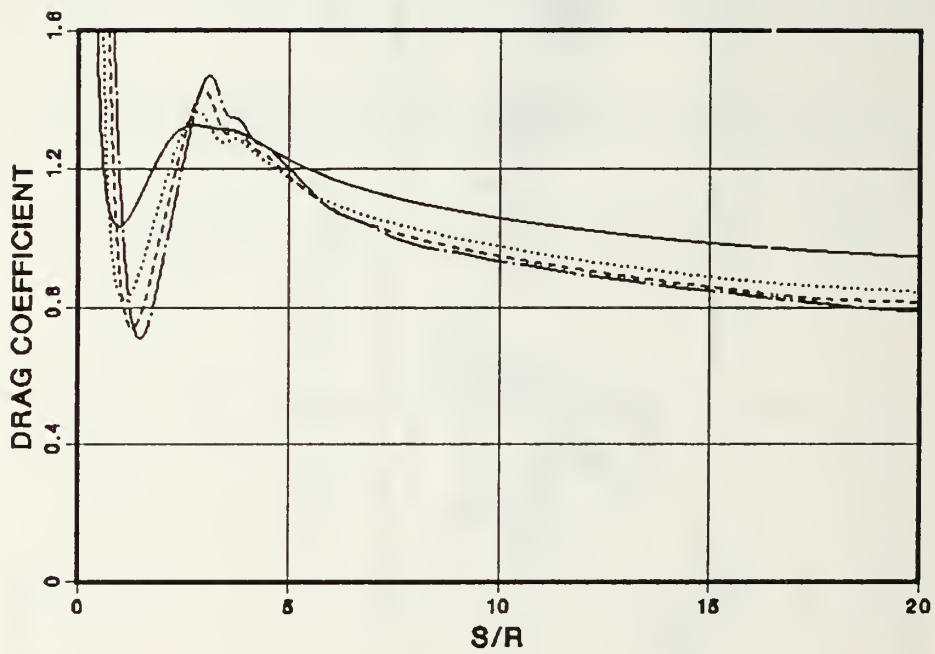


Figure 8. C_{IL} versus S/R , $\Omega = 0.1$, — : $Re = 250$, : $Re = 500$,
 ---- : $Re = 750$, — · — : $Re = 1000$

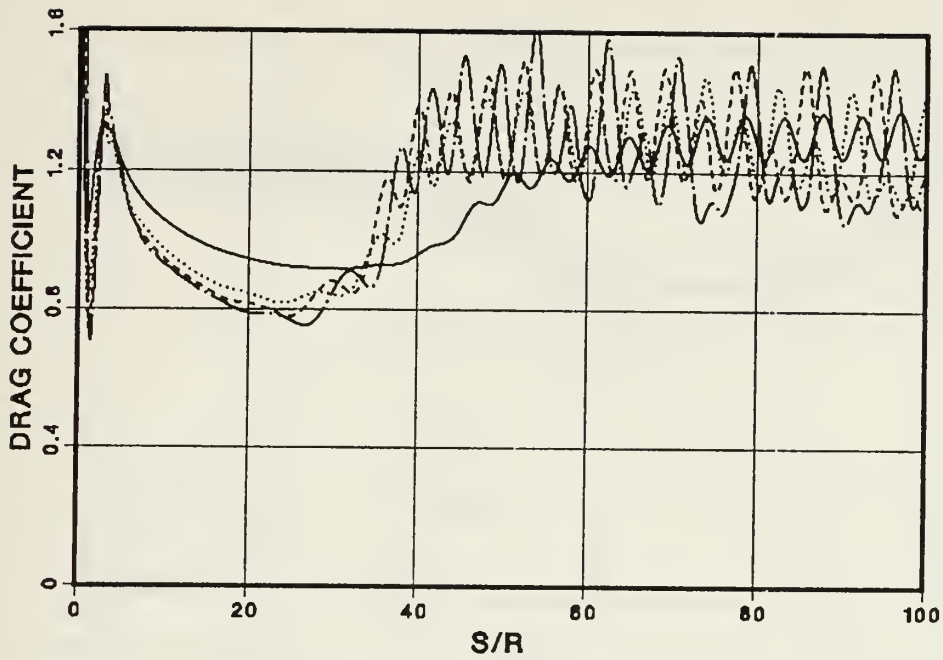


Figure 9. C_{DL} versus S/R , $\Omega = 0.1$, (lines same as in Fig. 8)

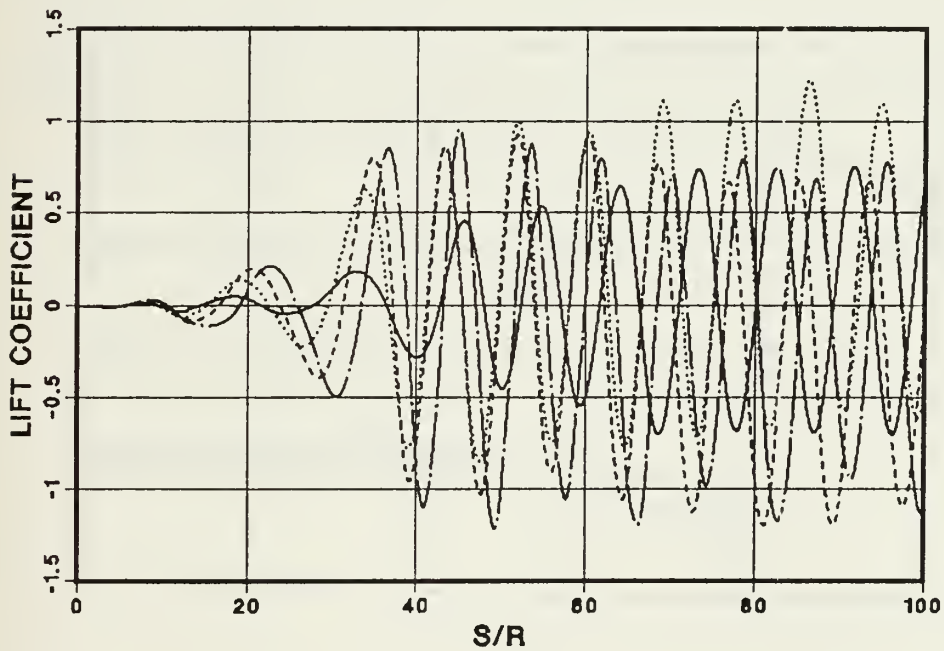


Figure 10. C_L versus S/R , $\Omega = 0.1$, (lines same as in Fig. 8)

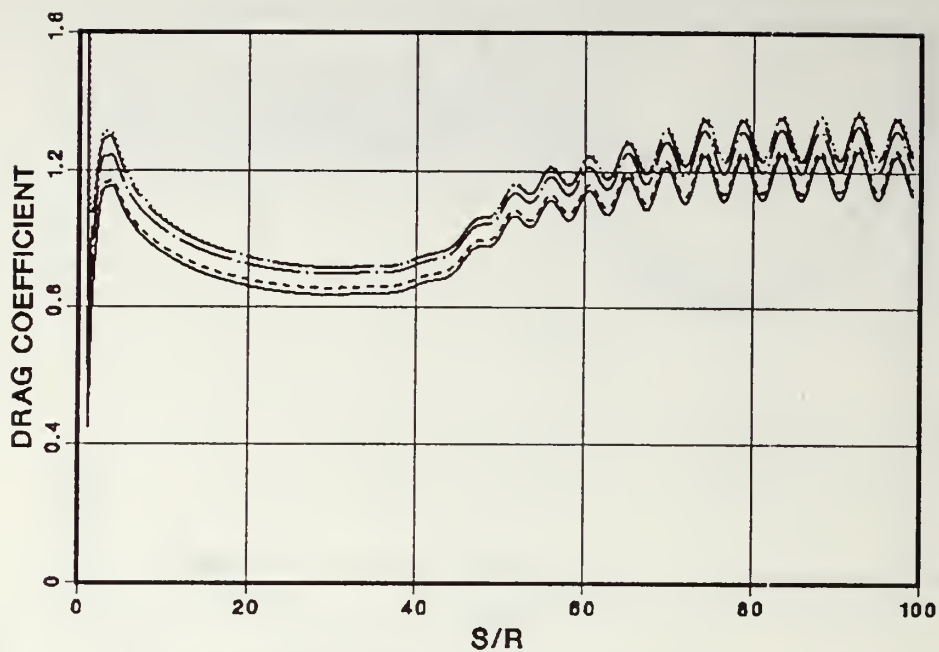


Figure 11. C_{IL} versus S/R , $\Omega = 0.25$, — : $n = 2$, : $n = 4$,
 ----- : $n = 6$, — · — : $n = 8$, — — — : $n = 10$

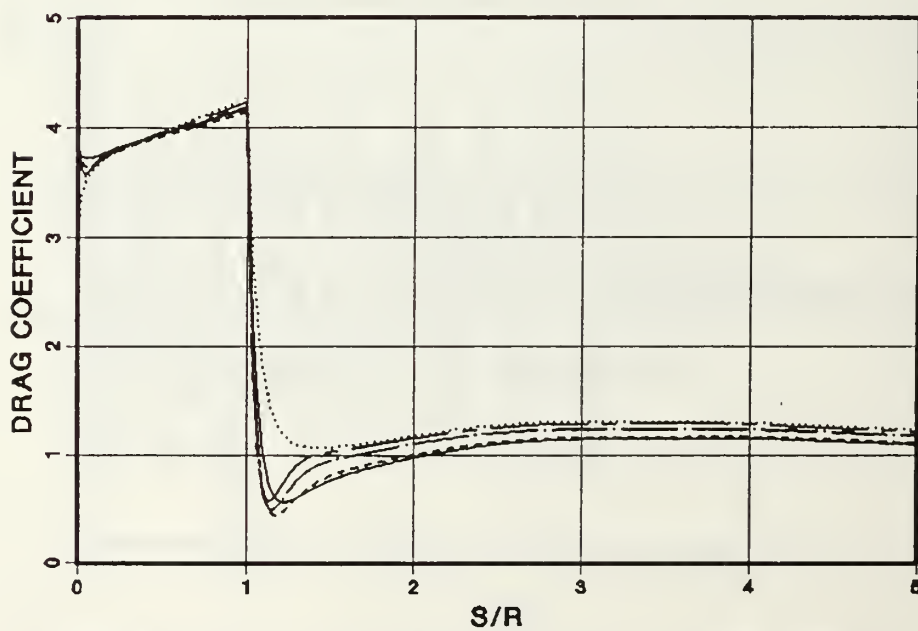


Figure 12. C_{IL} versus S/R , $\Omega = 0.25$, (lines same as in Fig. 11)

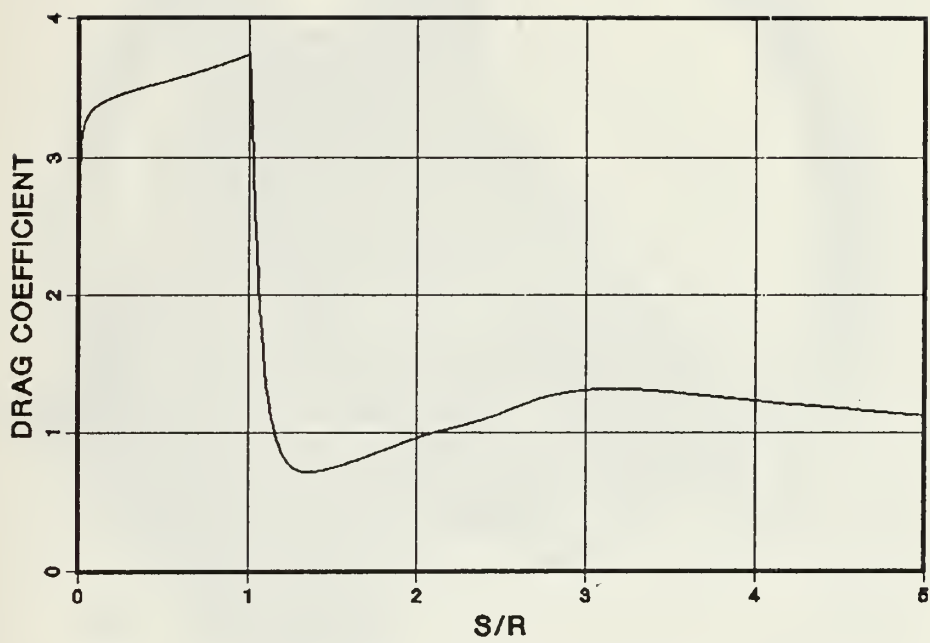


Figure 13. C_{IL} versus S/R , $\Omega = 1$, $Re = 1000$, $\Delta\xi = 1/128$

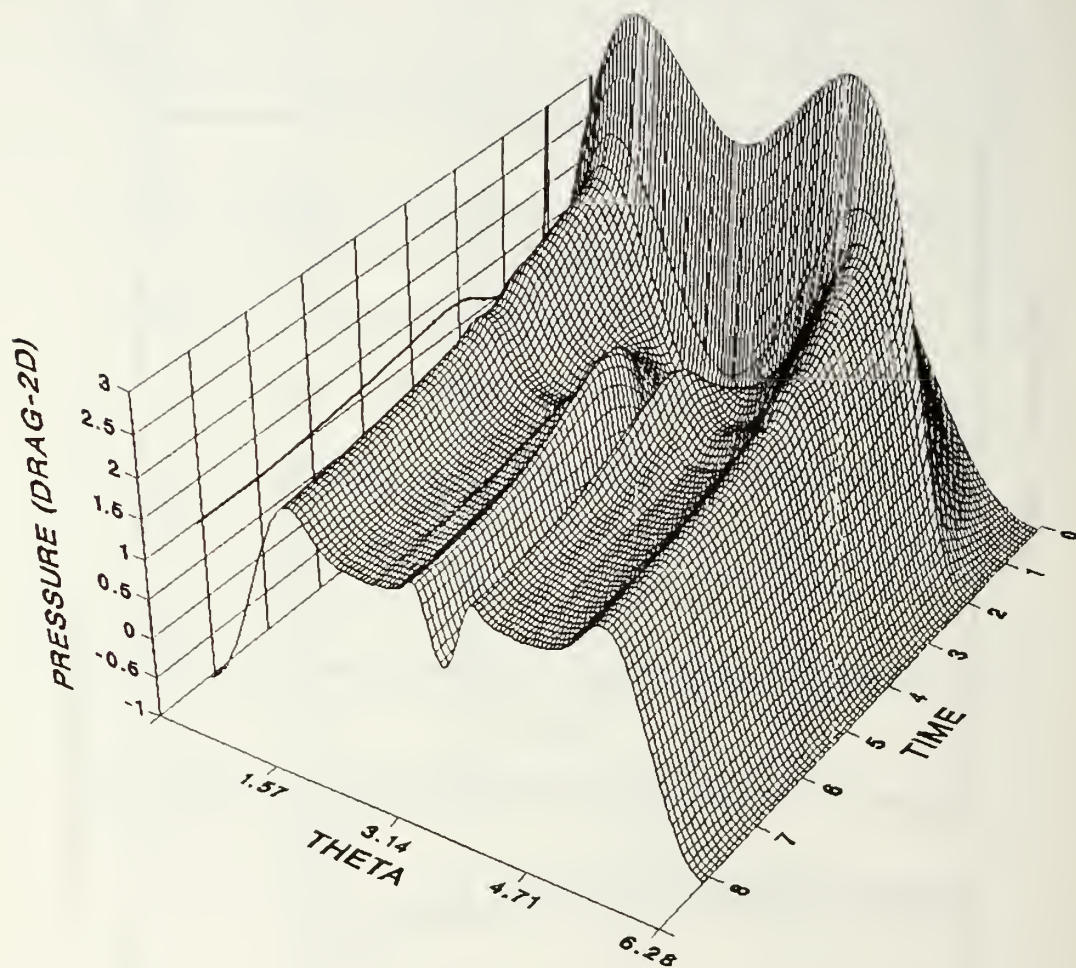


Figure 14. Pressure p_s around Cylinder versus Time(τ), $\Omega = 1$



Figure 15. Vorticity Contours, $\Omega = 1$, $S/R = 1$

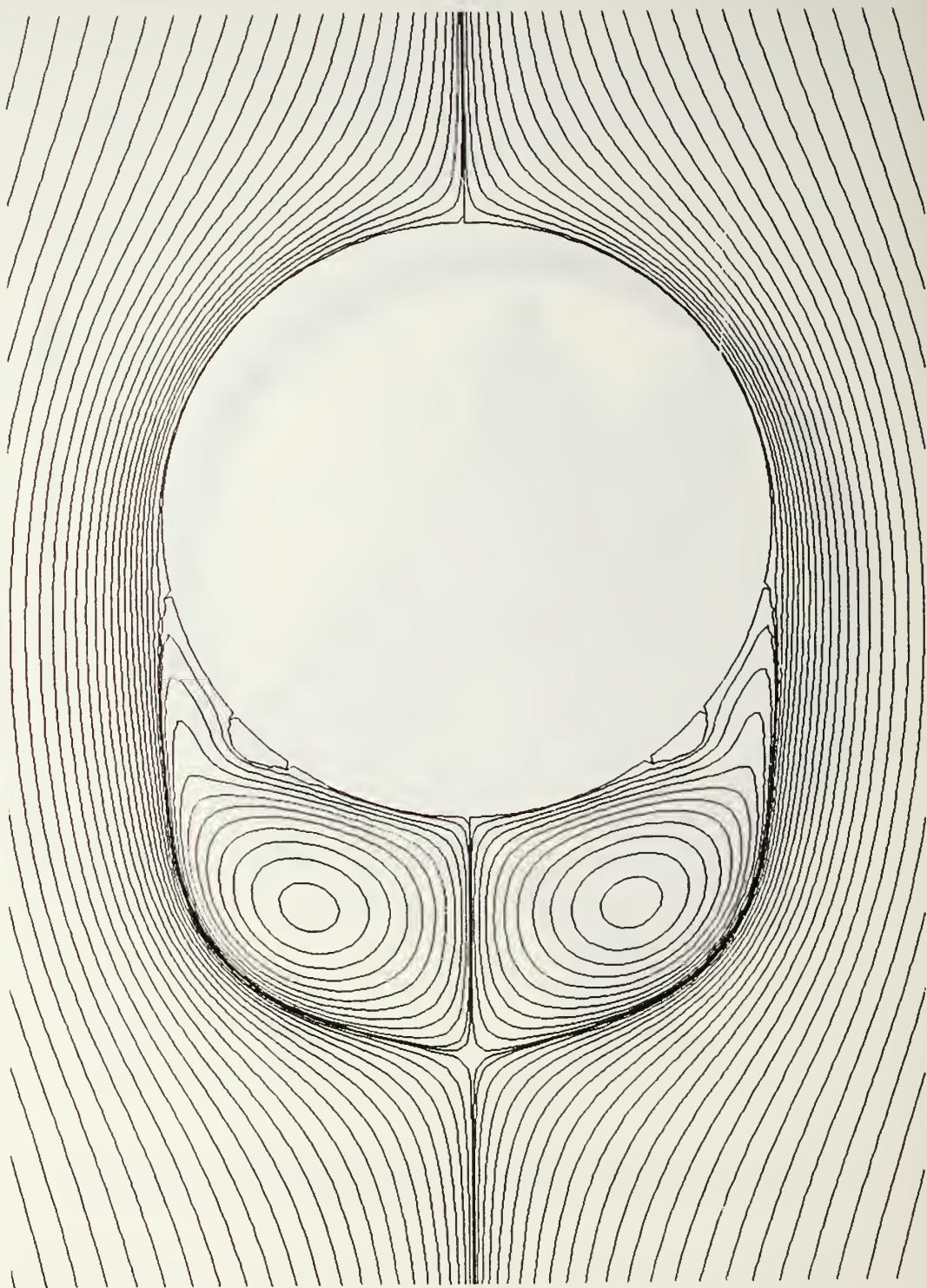


Figure 16. Streamlines $\Omega = 1$, $S/R = 3$

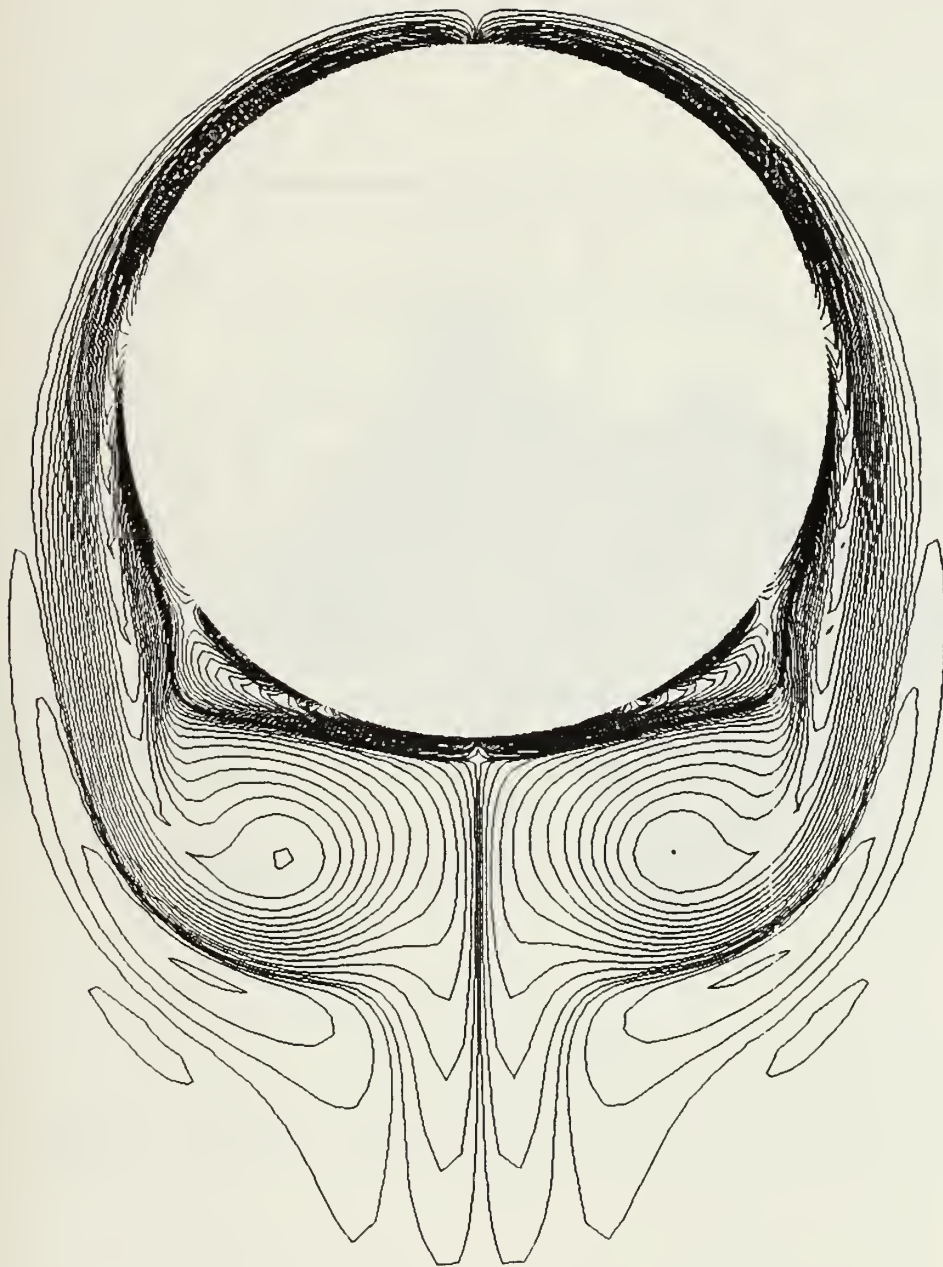


Figure 17. Vorticity Contours, $\Omega = 1, S/R = 3$

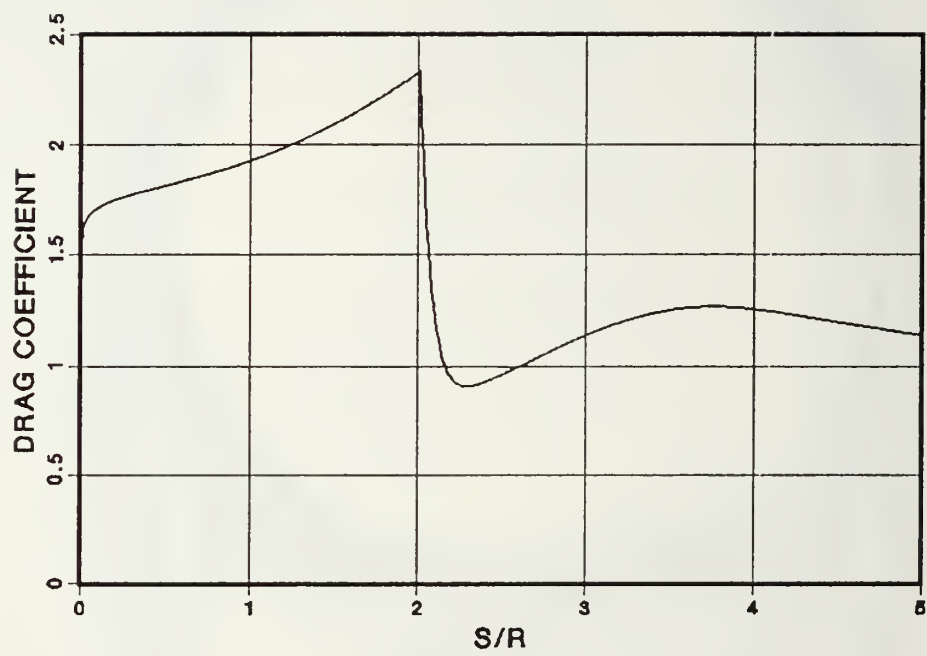


Figure 18. C_{IL} versus S/R , $\Omega = 2$, $Re = 1000$, $\Delta\xi = 1/128$

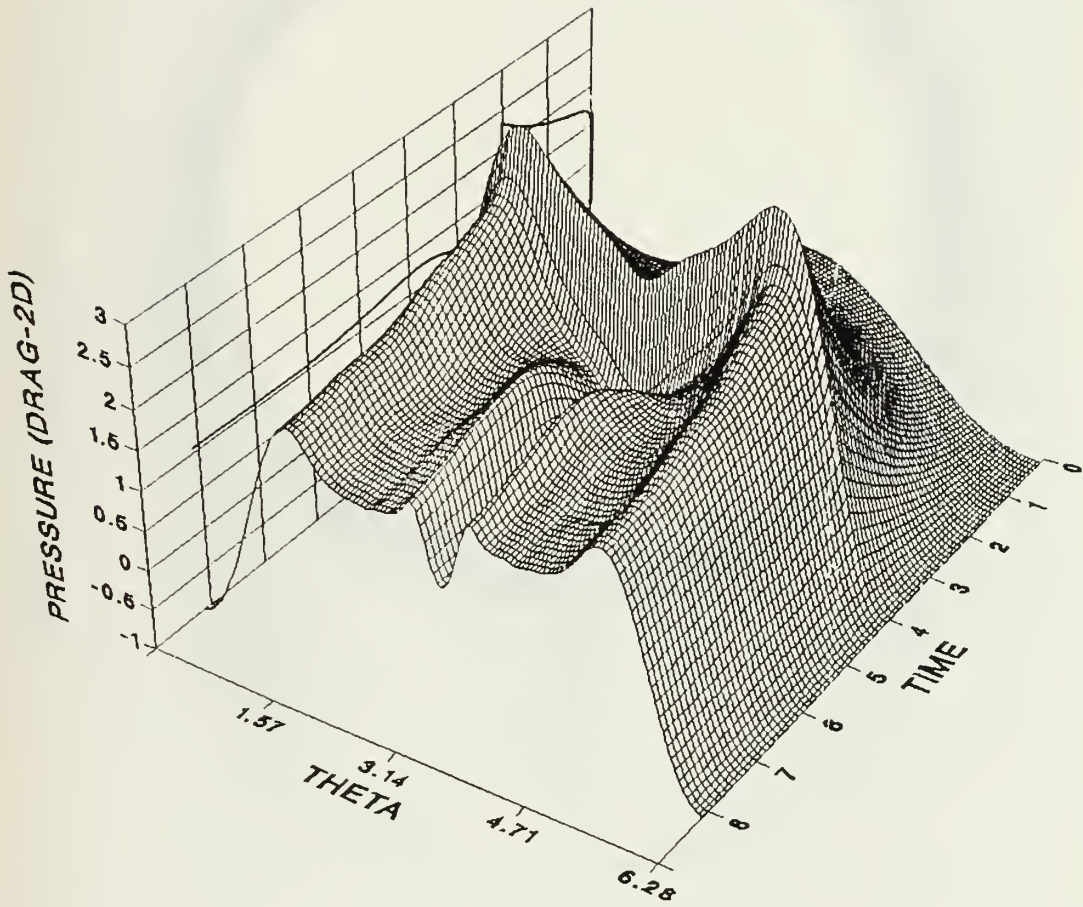


Figure 19. Pressure p_s around the Cylinder versus Time(τ), $\Omega = 2$



Figure 20. Vorticity Contours, $\Omega = 2$, $S/R = 2$

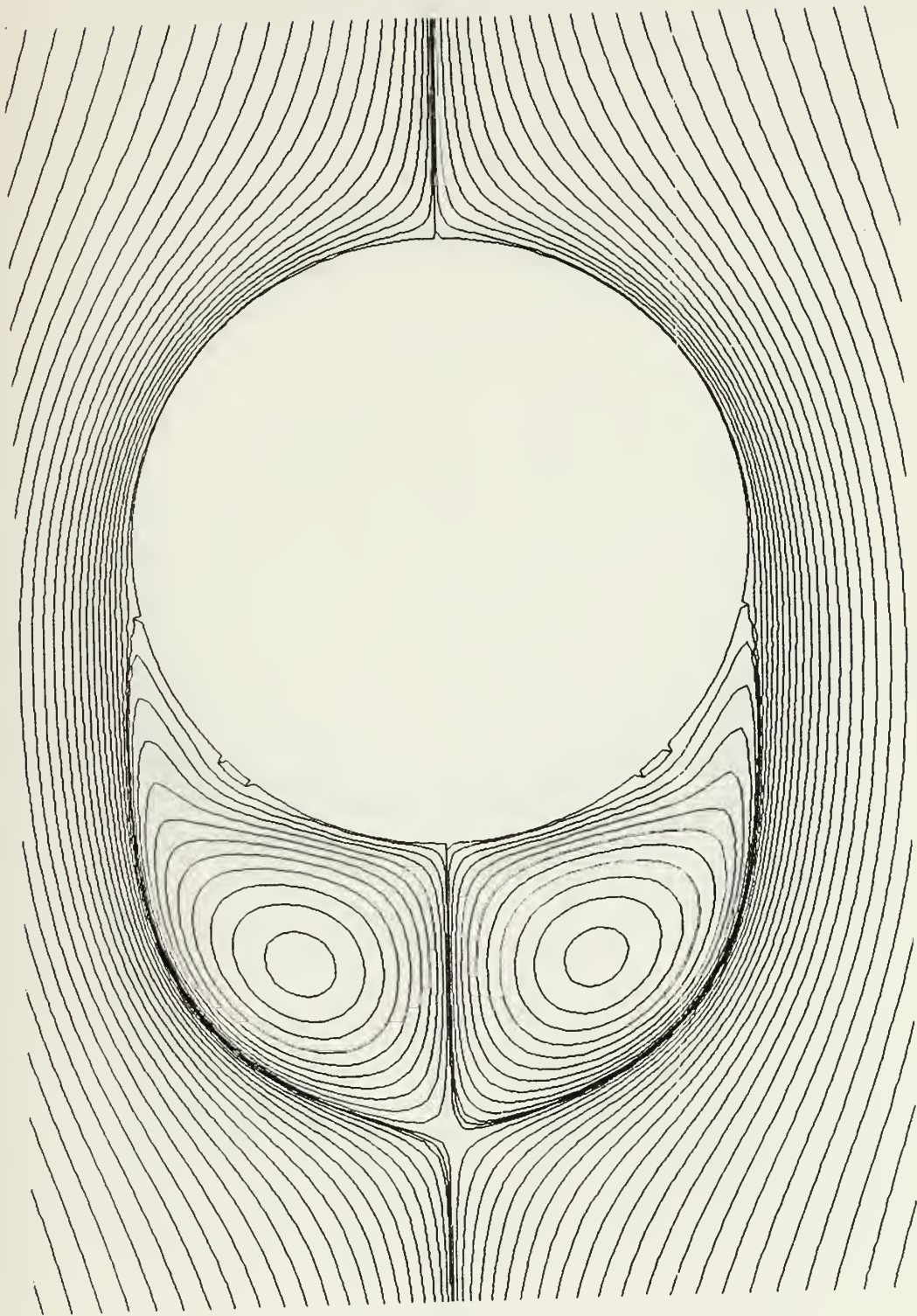


Figure 21. Streamlines $\Omega = 2$, $S/R = 2$



Figure 22. Vorticity Contours, $\Omega = 2$, $S/R = 3.5$

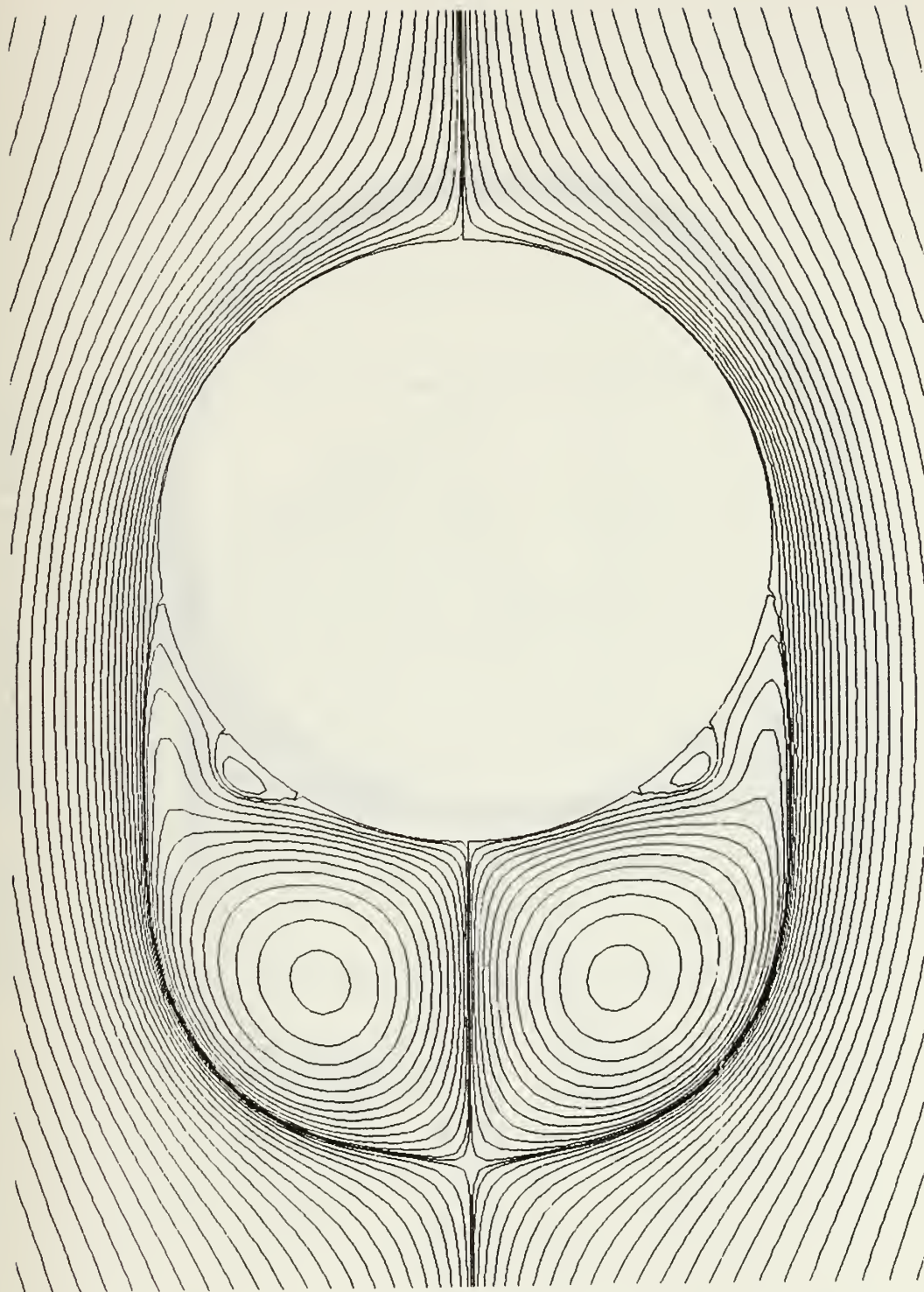


Figure 23. Streamlines $\Omega = 2$, $S/R = 4$



Figure 24. Vorticity Contours, $\Omega = 2$, $S/R = 4$

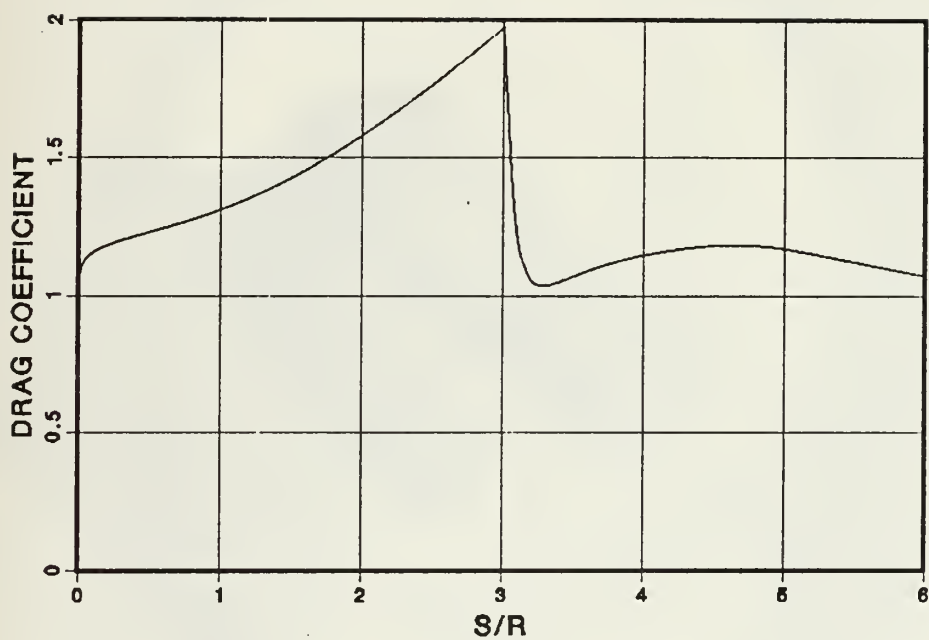


Figure 25. C_{IL} versus S/R , $\Omega = 3$, $Re = 1000$, $\Delta\xi = 1/128$

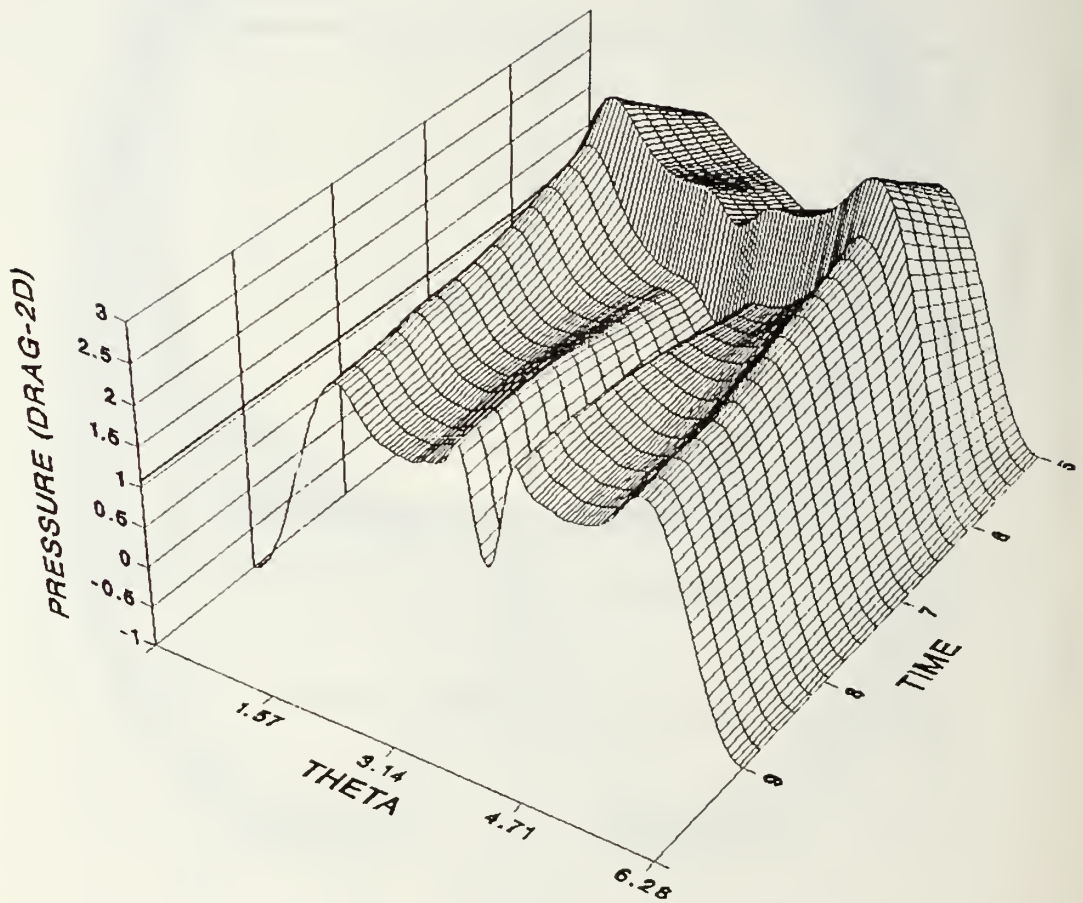


Figure 26. Pressure p_s around the Cylinder versus Time(τ), $\Omega = 3$

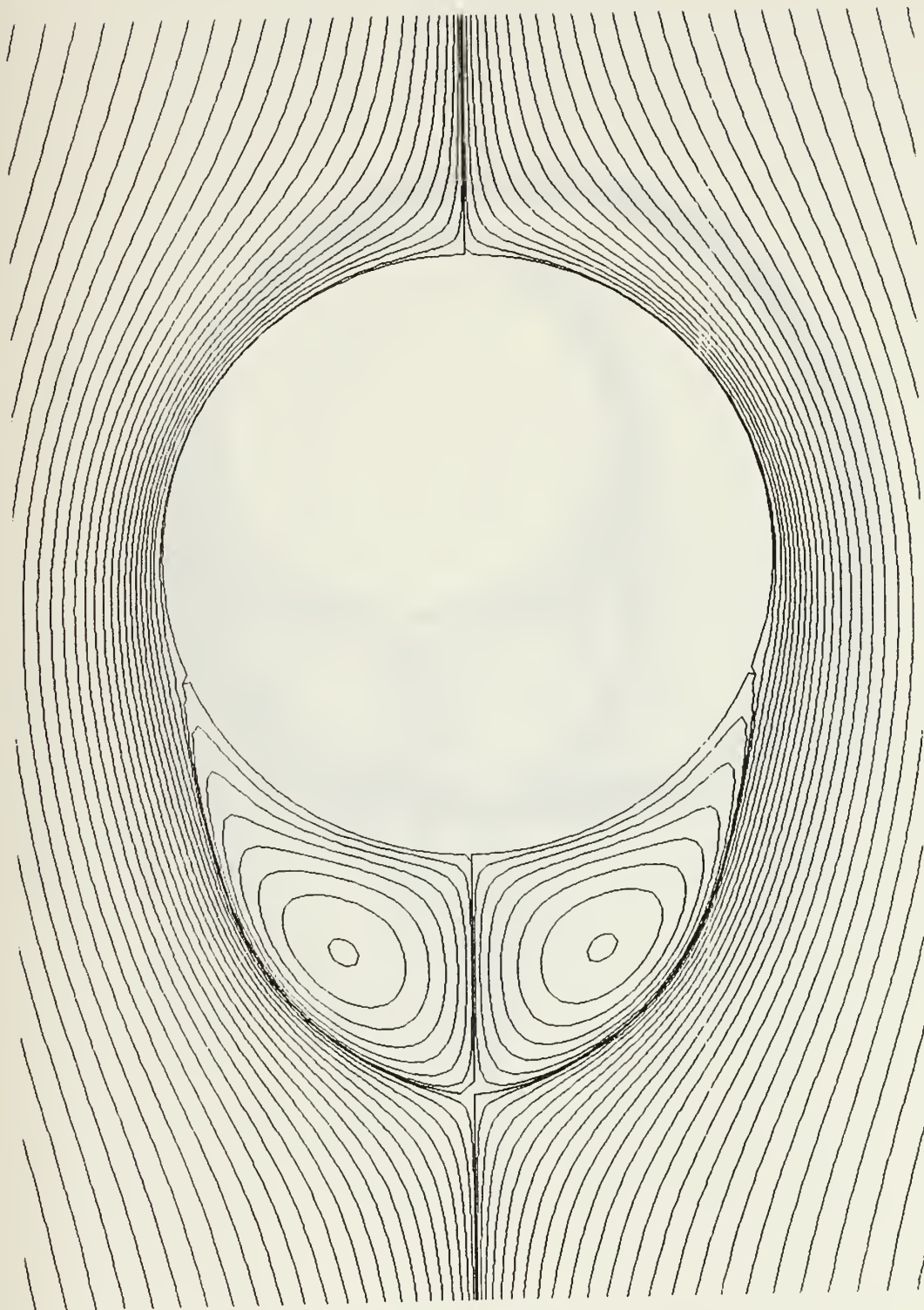


Figure 27. Streamlines, $\Omega = 3$, $S/R = 3$

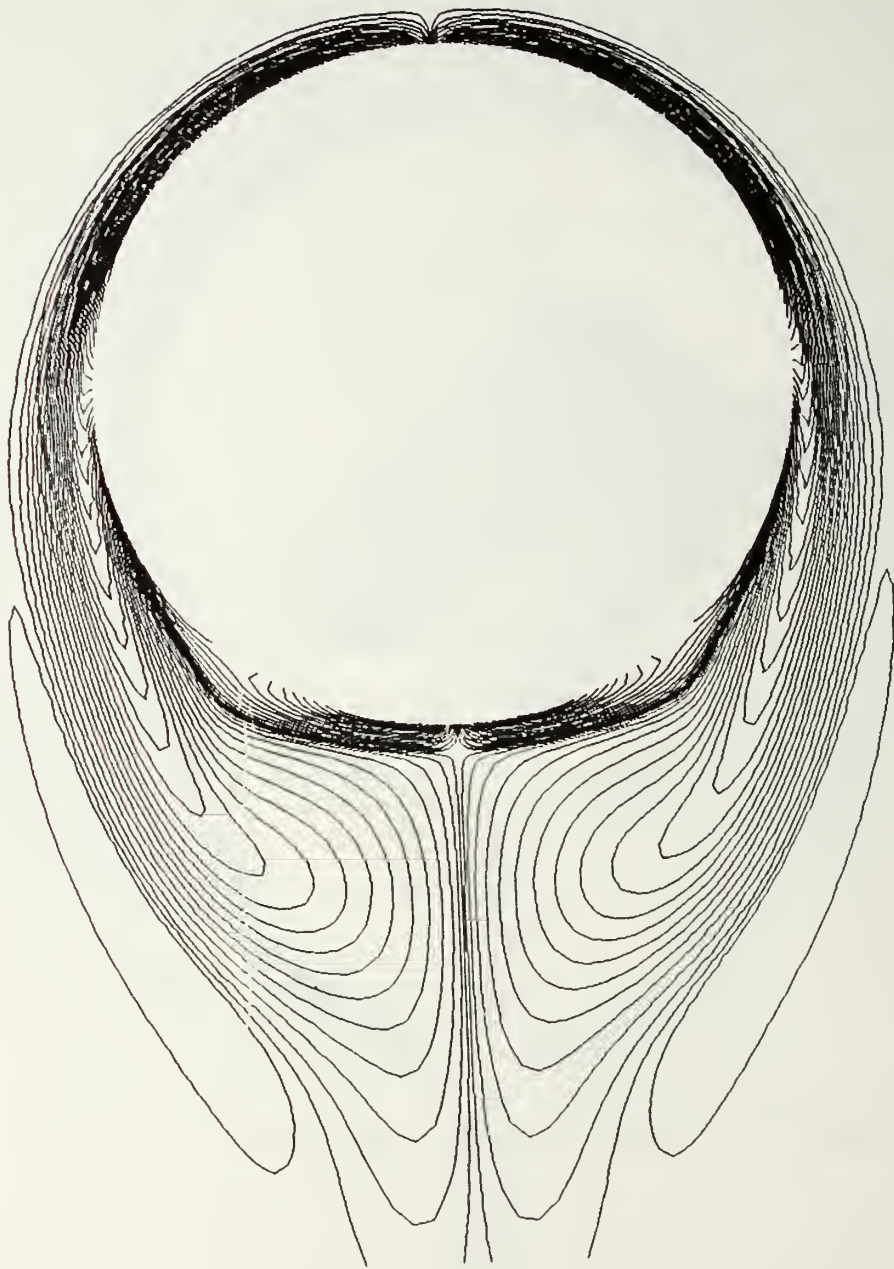


Figure 28. Vorticity Contours, $\Omega = 3$, $S/R = 3$

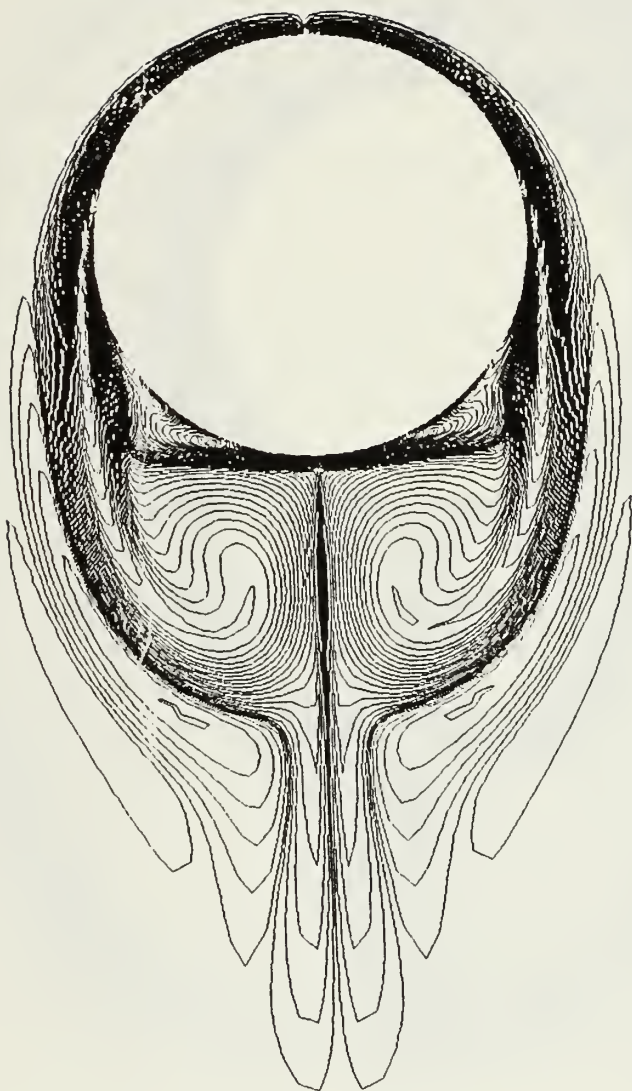


Figure 29. Vorticity Contours, $\Omega = 3$, $S/R = 4.4$

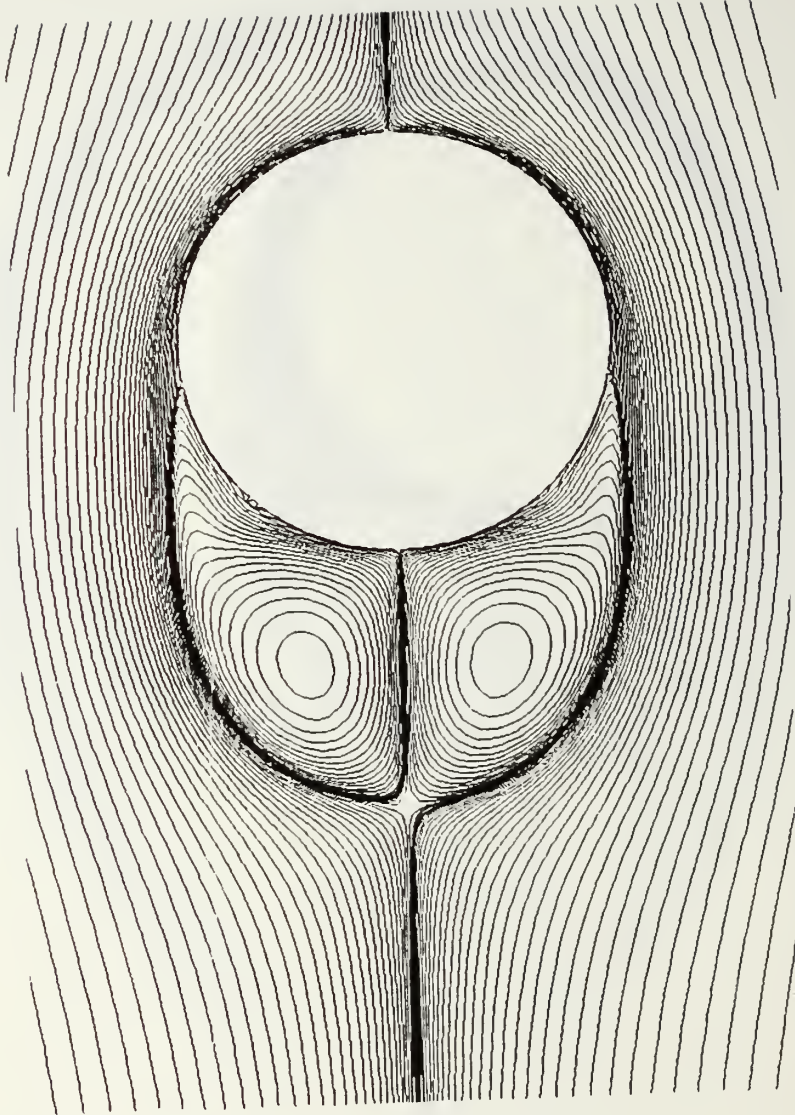


Figure 30. Streamlines, $\Omega = 3$, $S/R = 4.4$

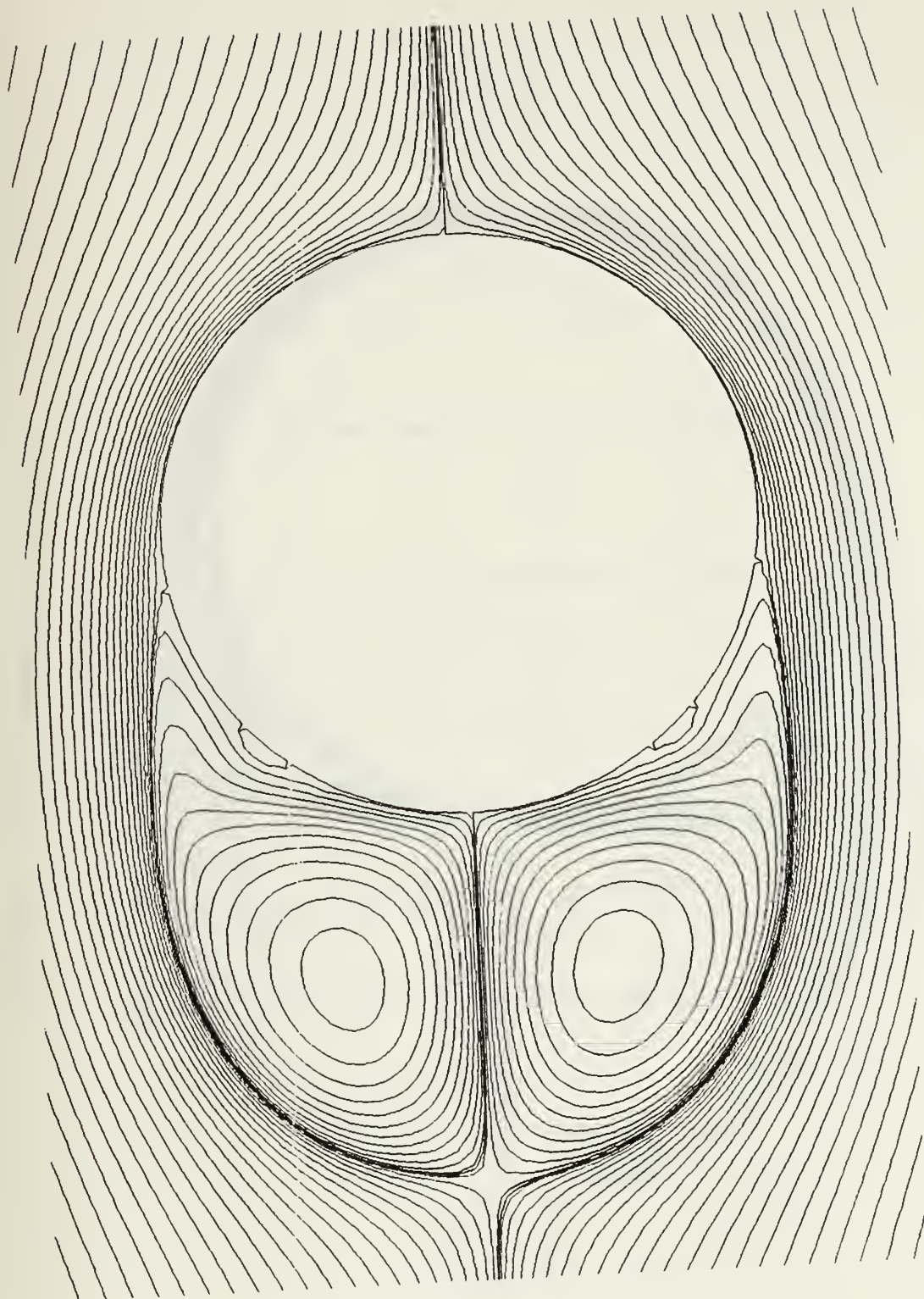


Figure 31. Streamlines $\Omega = 3$, $S/R = 4.6$

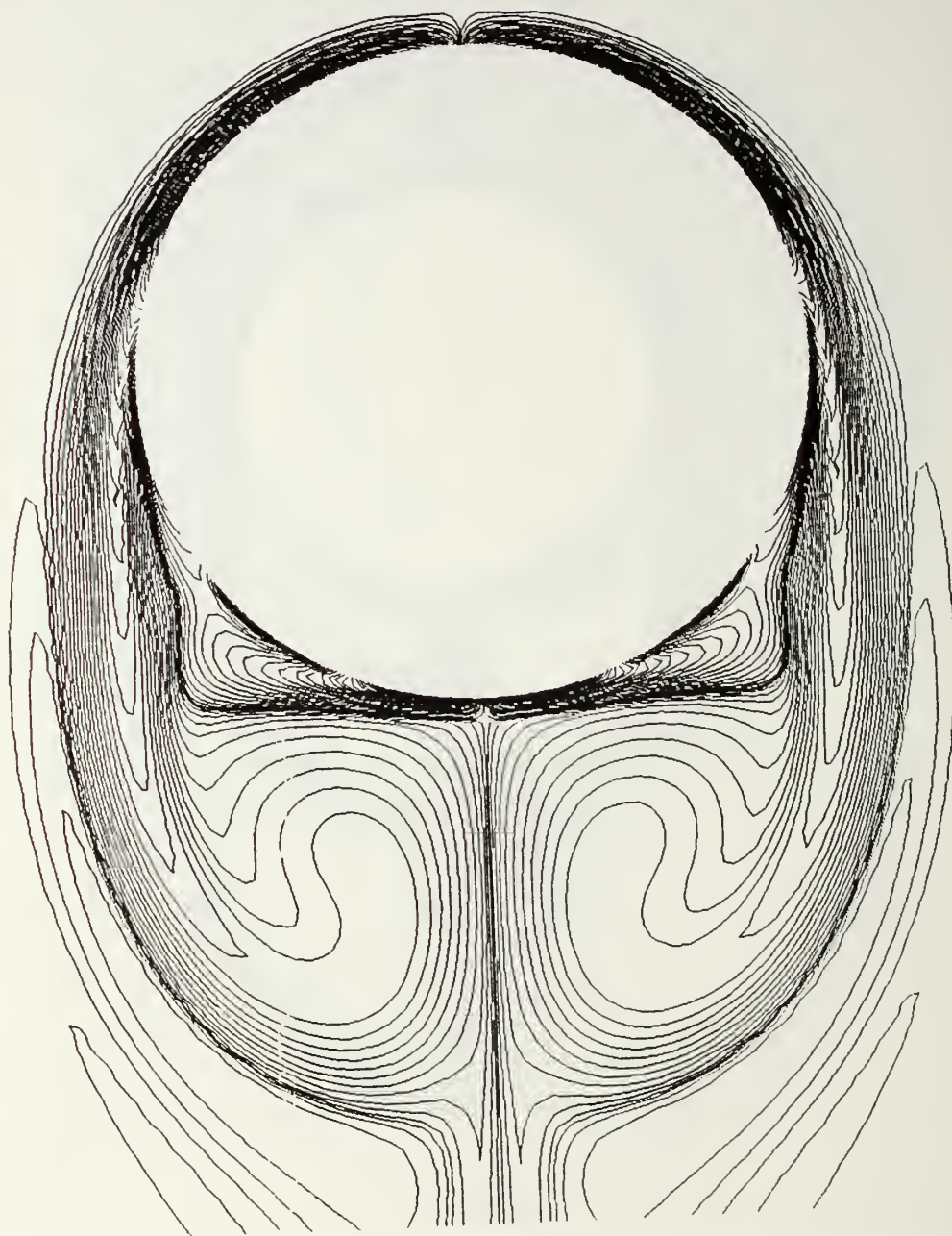


Figure 32. Vorticity Contours, $\Omega = 3$, $S/R = 4.6$

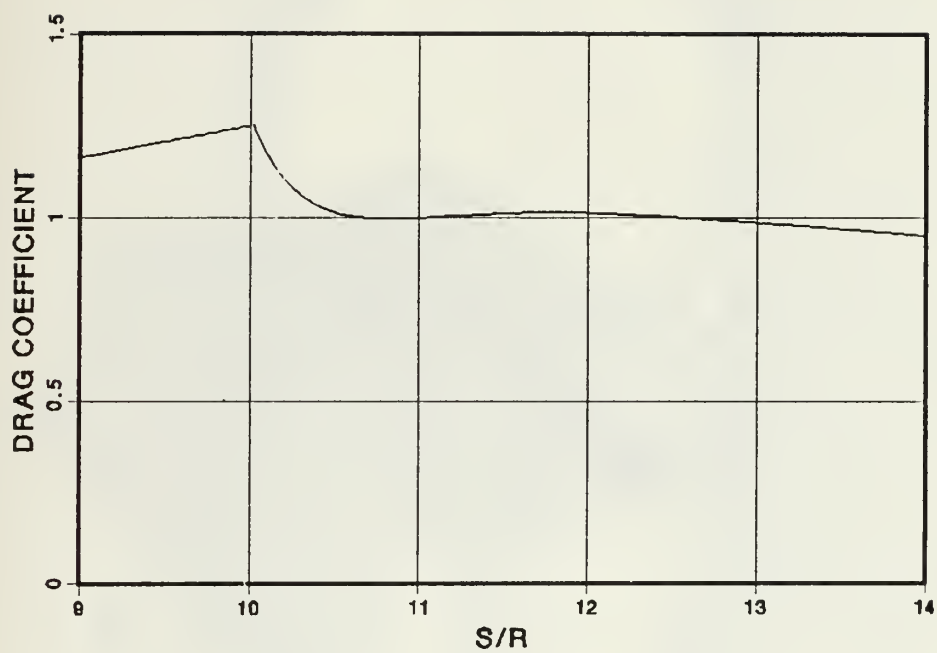


Figure 33. C_{IL} versus S/R , $\Omega = 10$, $Re = 1000$, $\Delta\xi = 1/128$

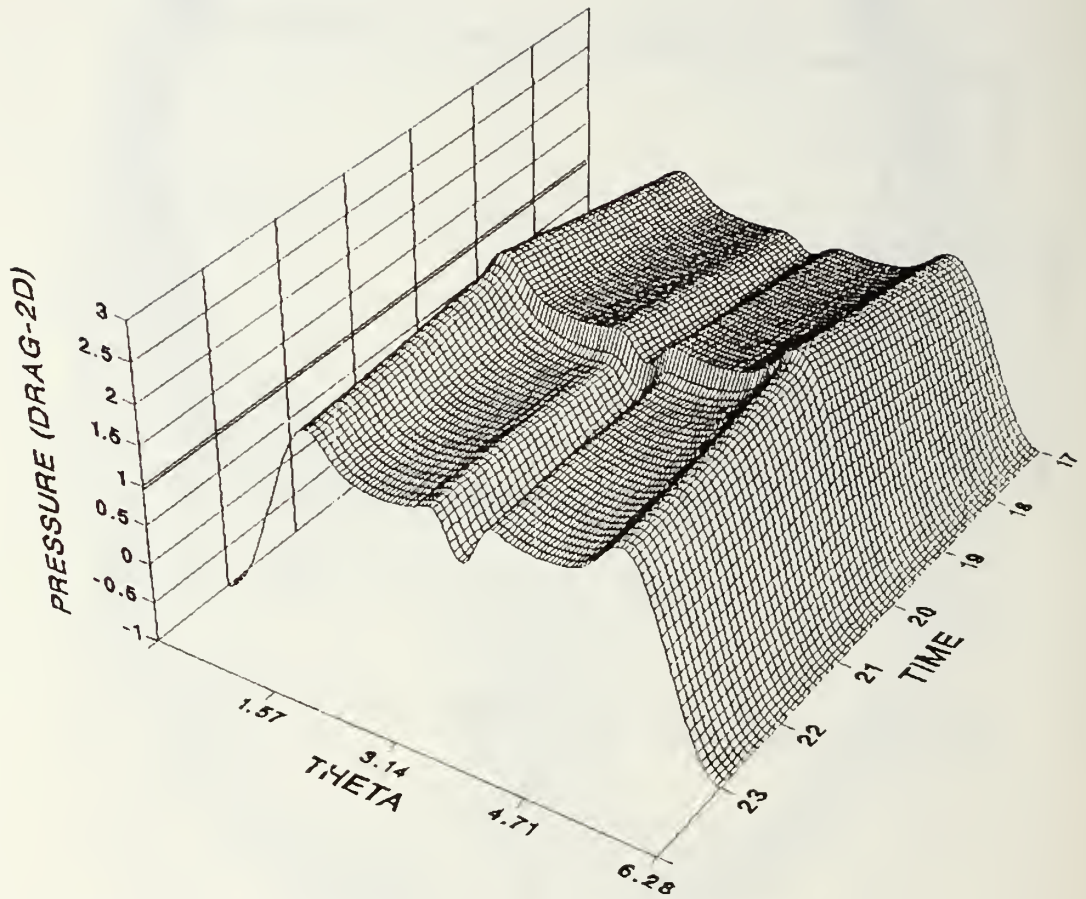


Figure 34. Pressure p_s around the Cylinder versus Time(τ), $\Omega = 10$

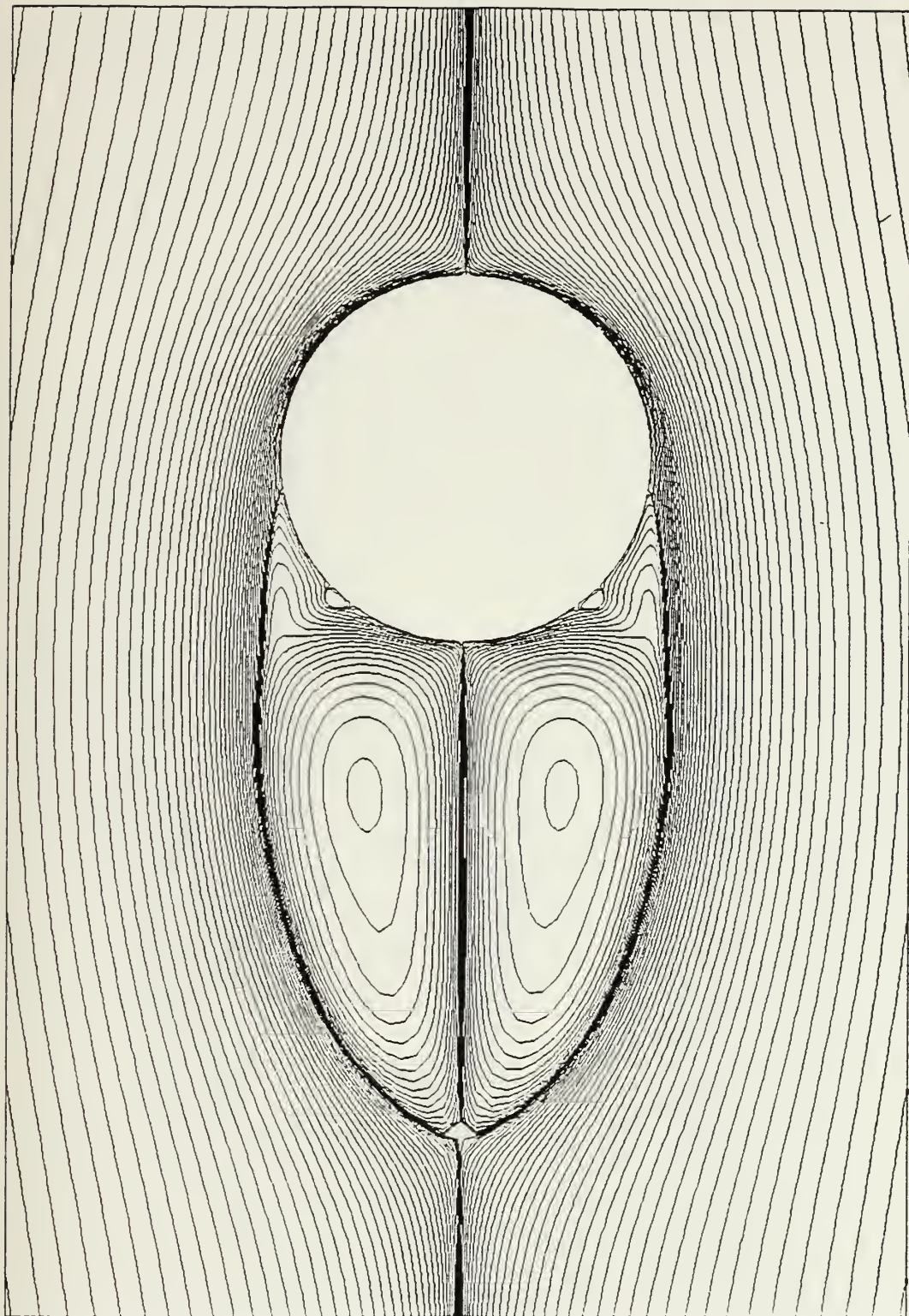


Figure 35. Streamlines, $\Omega = 10$, $S/R = 10$

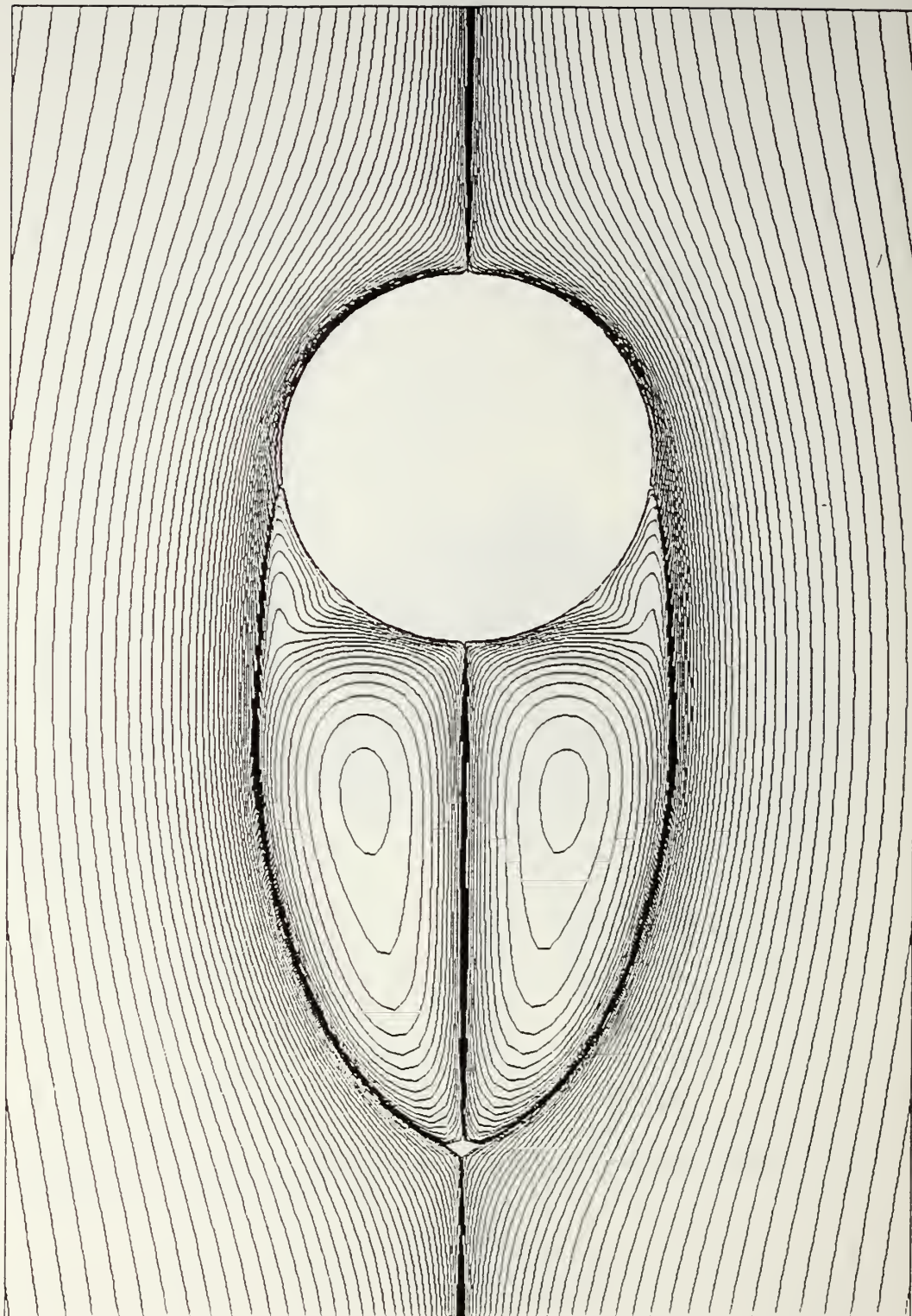


Figure 36. Streamlines, $\Omega = 10$, $S/R = 10.2$

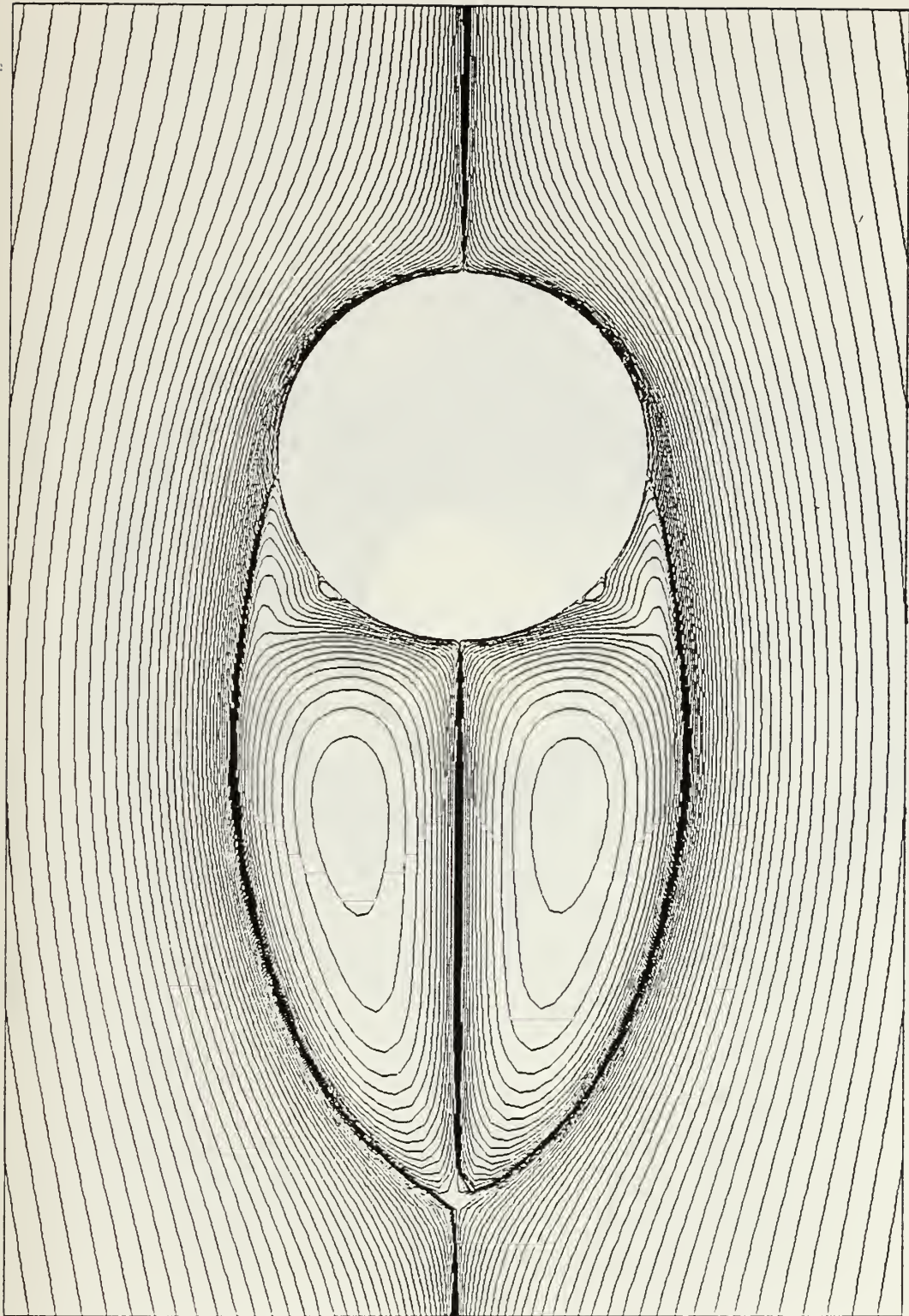


Figure 37. Streamlines, $\Omega = 10$, $S/R = 11.6$

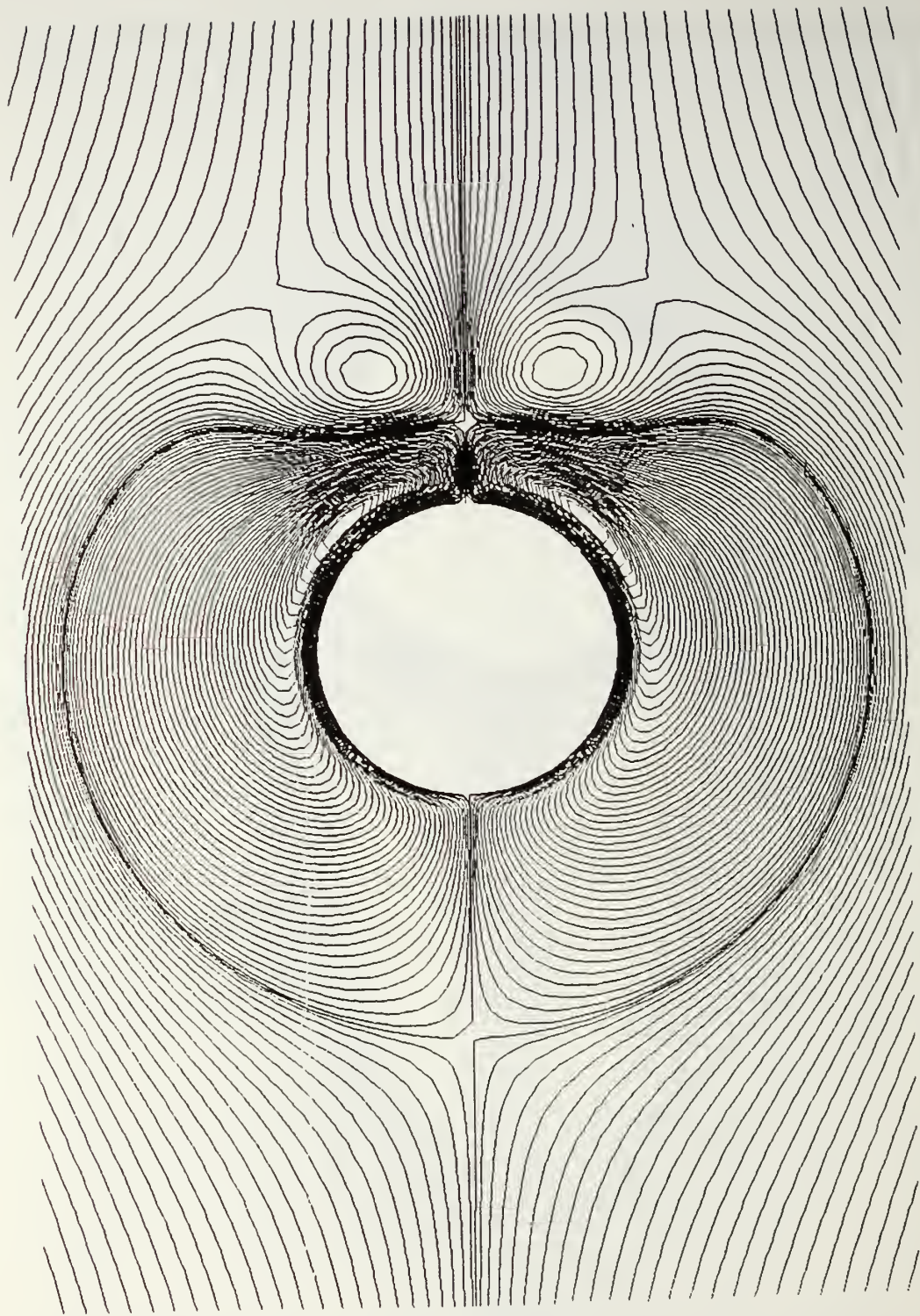


Figure 38. Streamlines (Total Ψ), $K = 1.5$, $\beta = 300$, $t/T = 4$

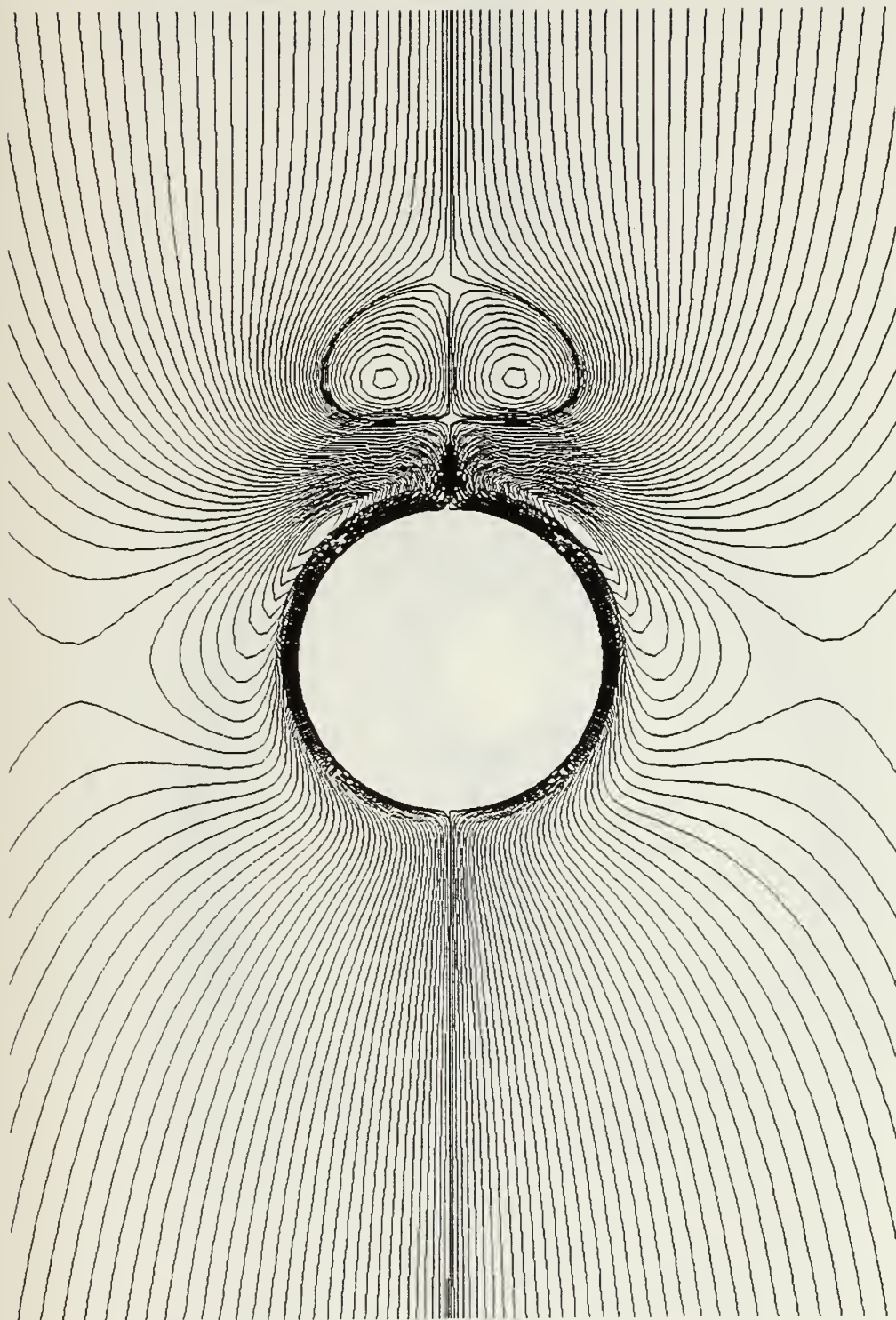


Figure 39. Streamlines (Total Ψ), $K = 1.5$, $\beta = 300$, $t/T = 4.004$

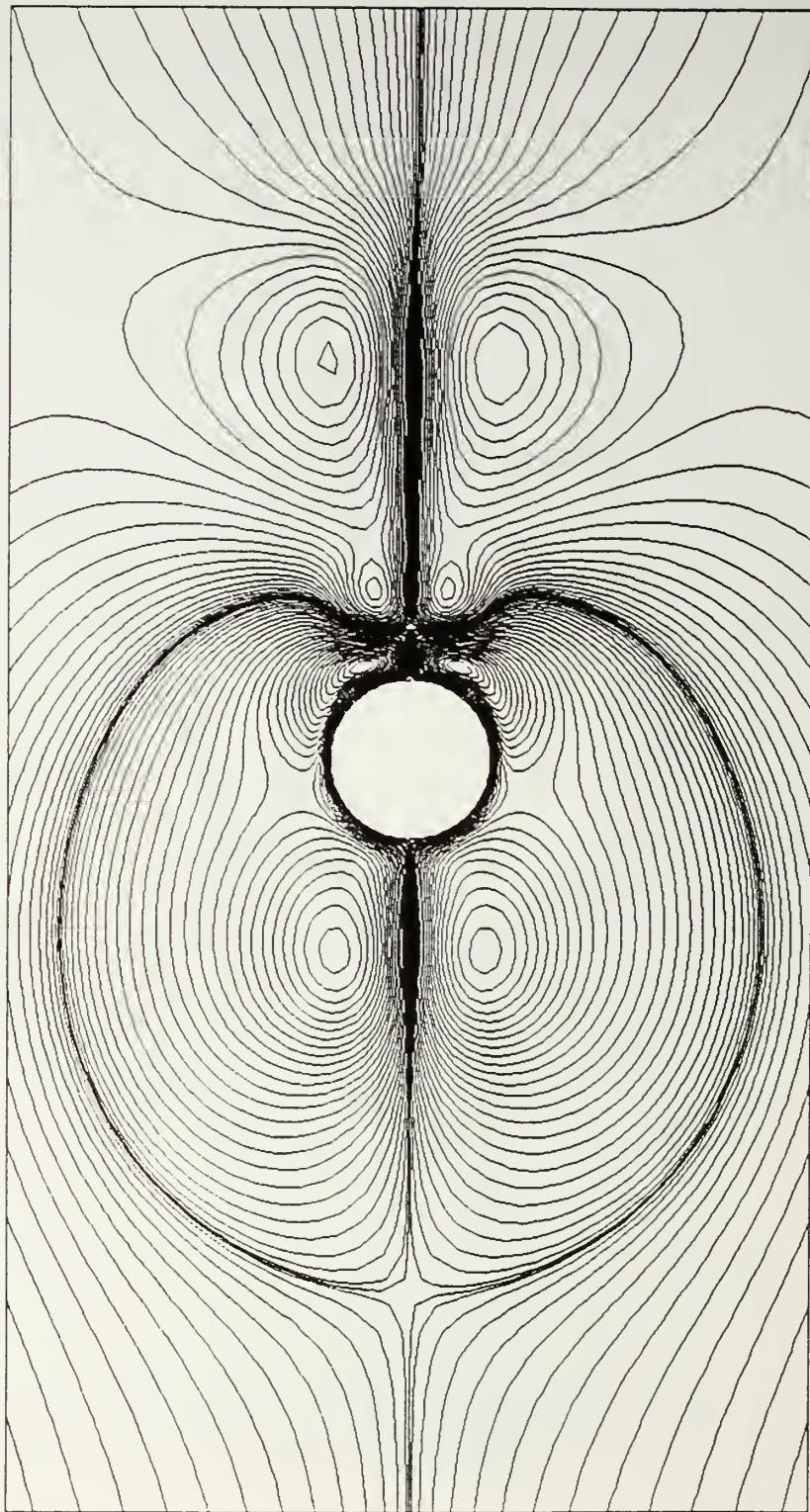


Figure 40. Streamlines (Total Ψ), $K = 3$, $\beta = 196$, $t/T = 6$

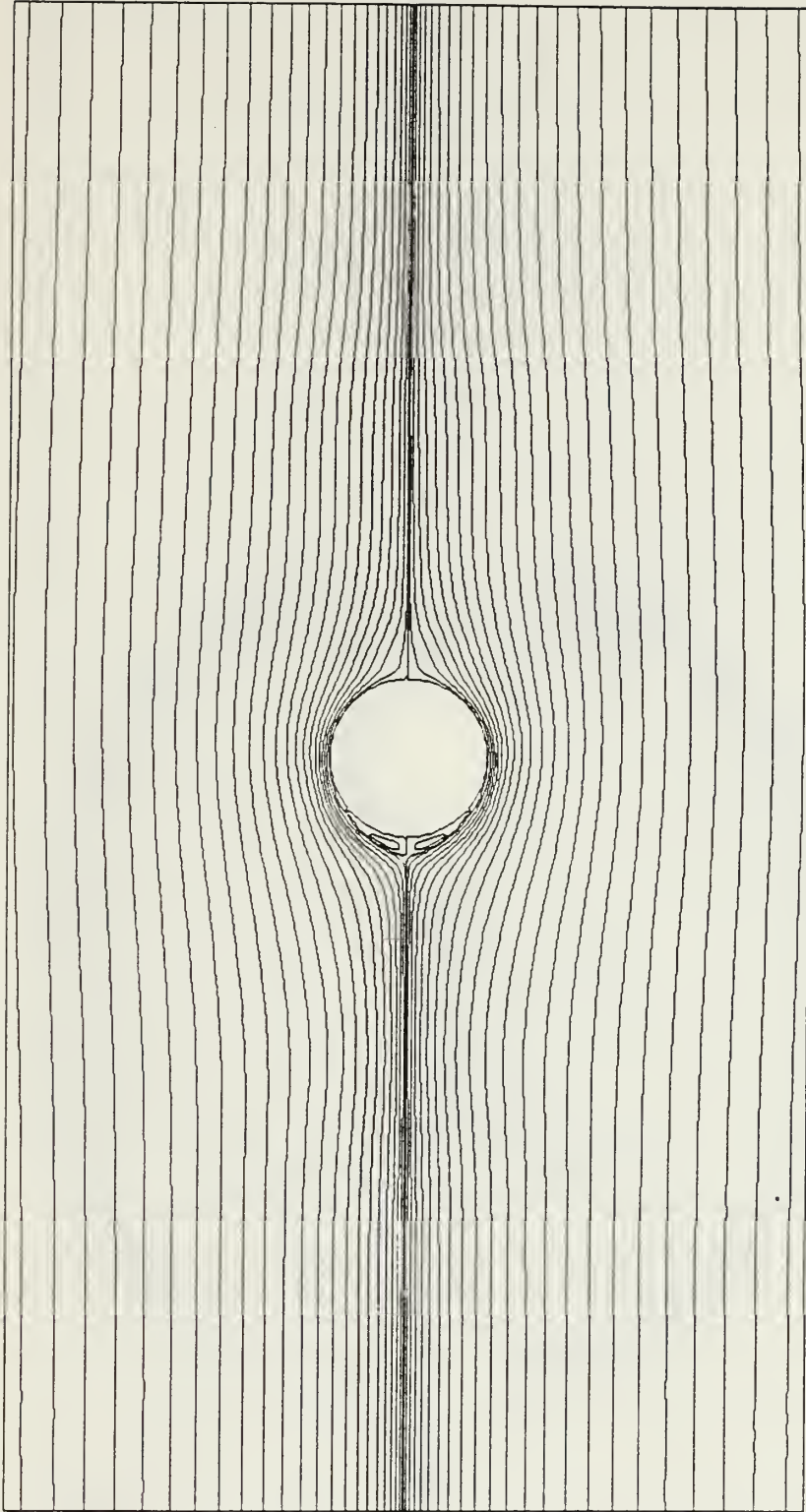


Figure 41. Streamlines (Total Ψ), $K = 3$, $\beta = 196$, $t/T = 6.25$

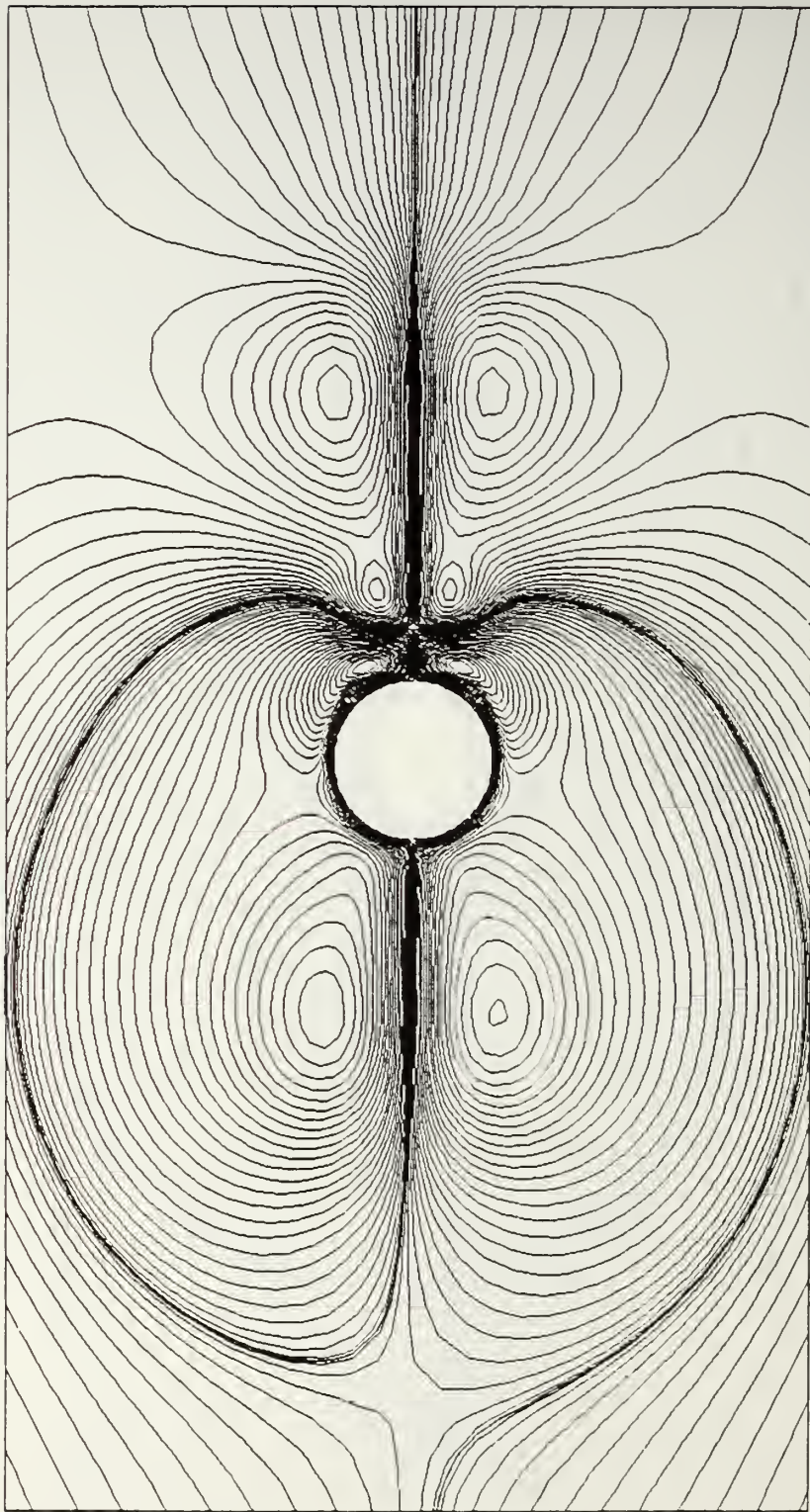


Figure 42. Streamlines (Total Ψ'), $K = 3$, $\beta = 196$, $t/T = 6.5$

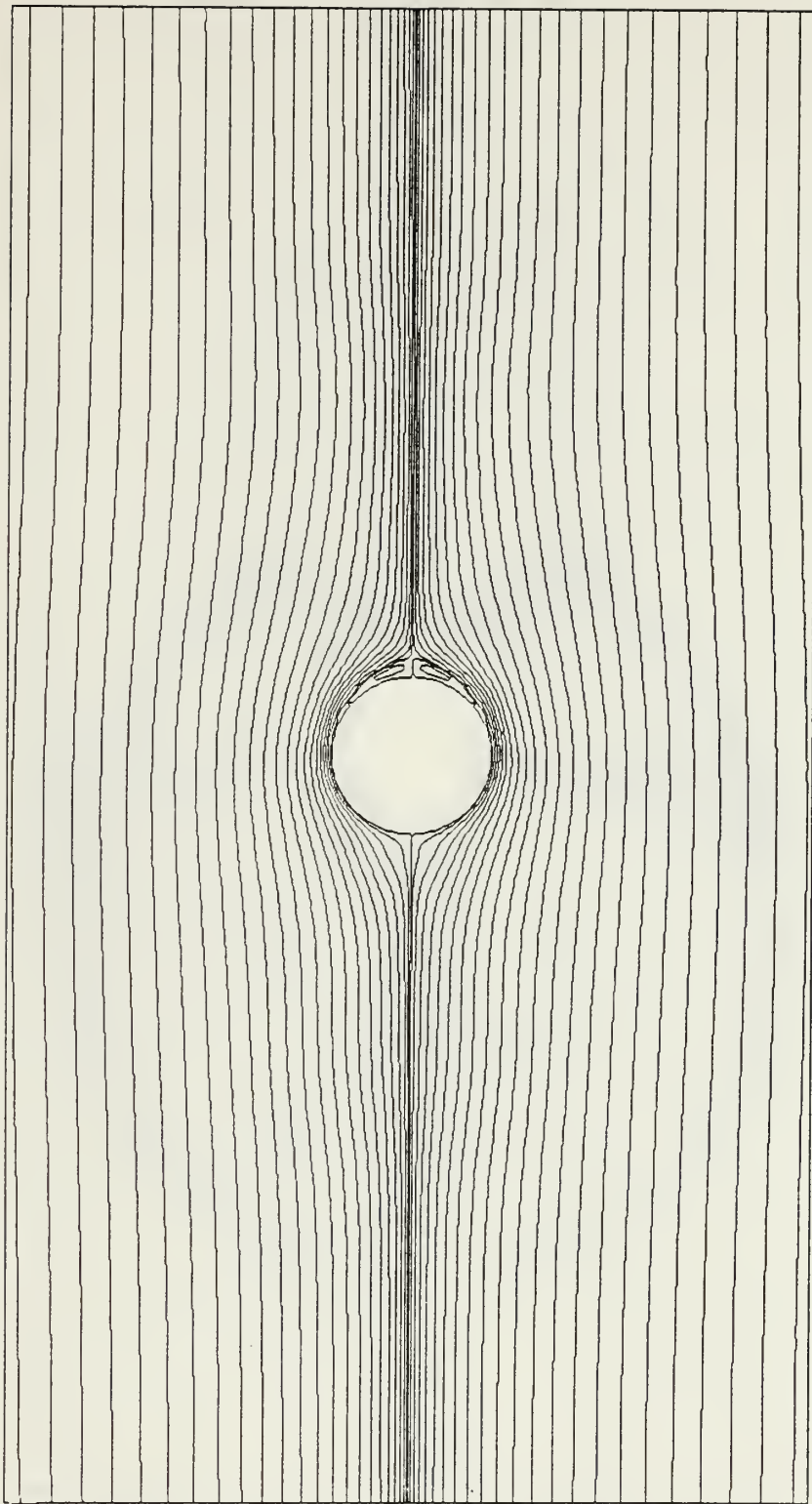


Figure 43. Streamlines (Total Ψ), $K = 3$, $\beta = 196$, $t/T = 6.75$

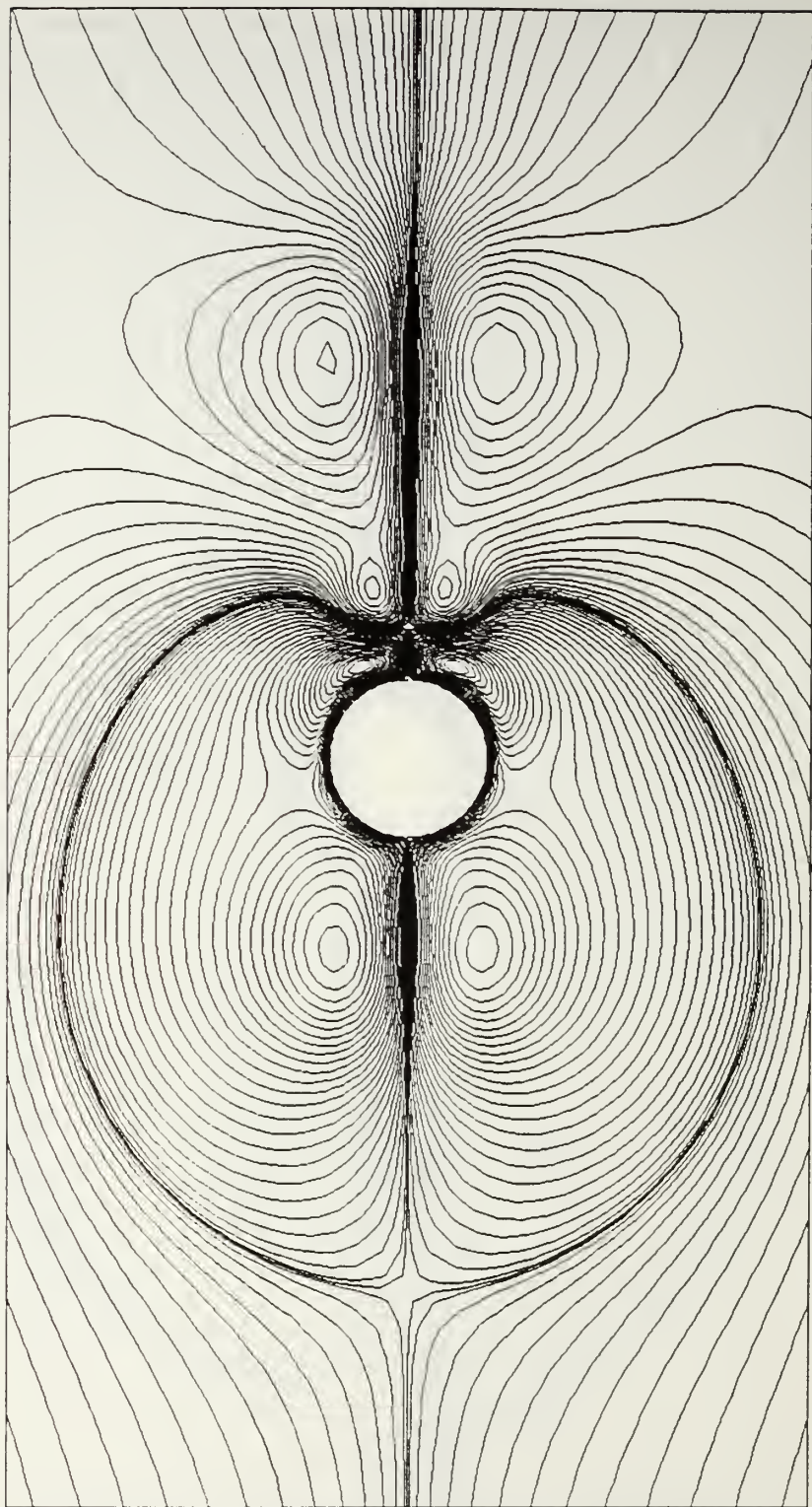


Figure 44. Streamlines (Relative Motion Ψ), $K = 3$, $\beta = 196$, $t/T = 6$

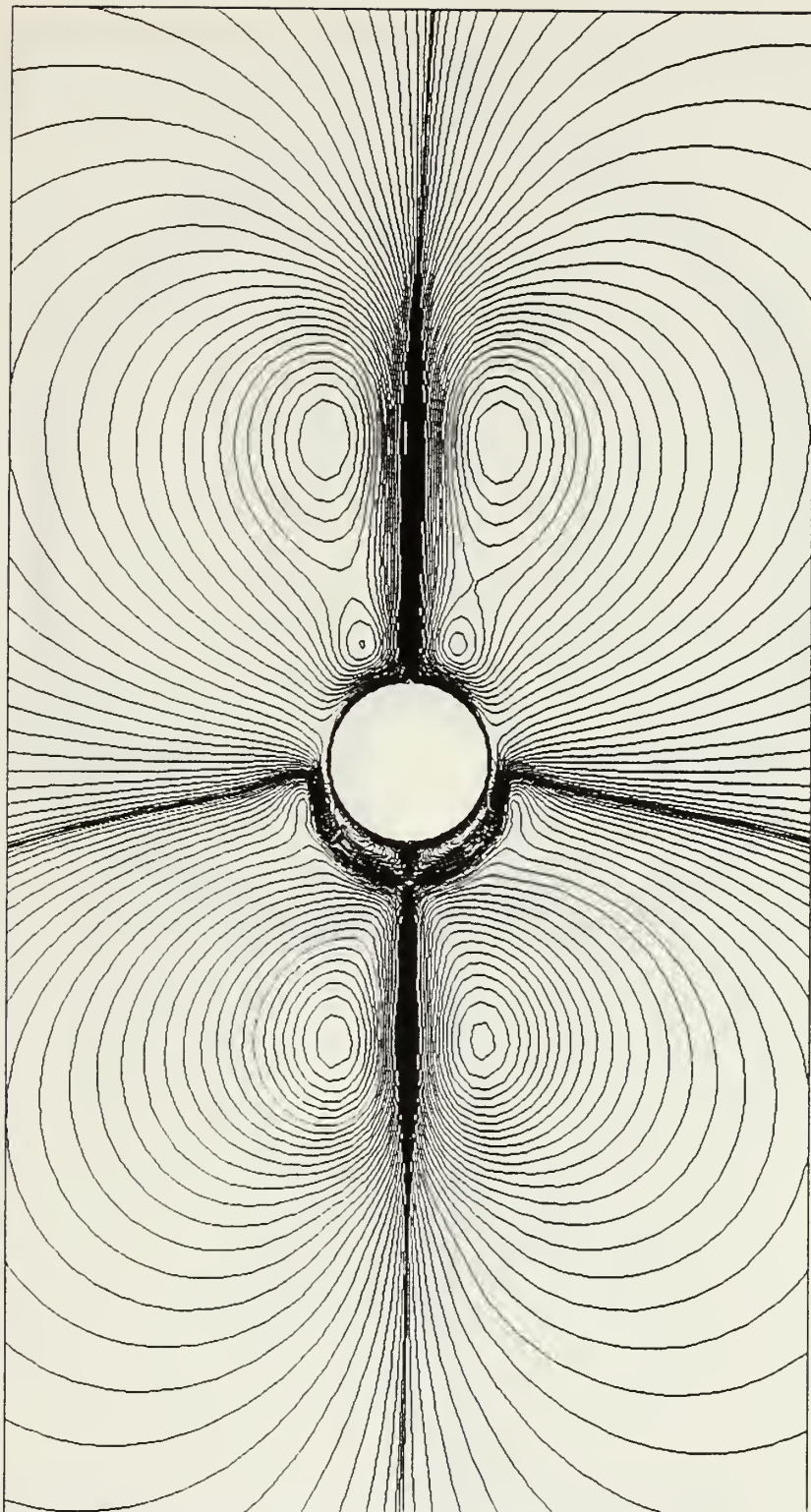


Figure 45. Streamlines (Relative Motion Ψ), $K = 3$, $\beta = 196$, $t/T = 6.25$

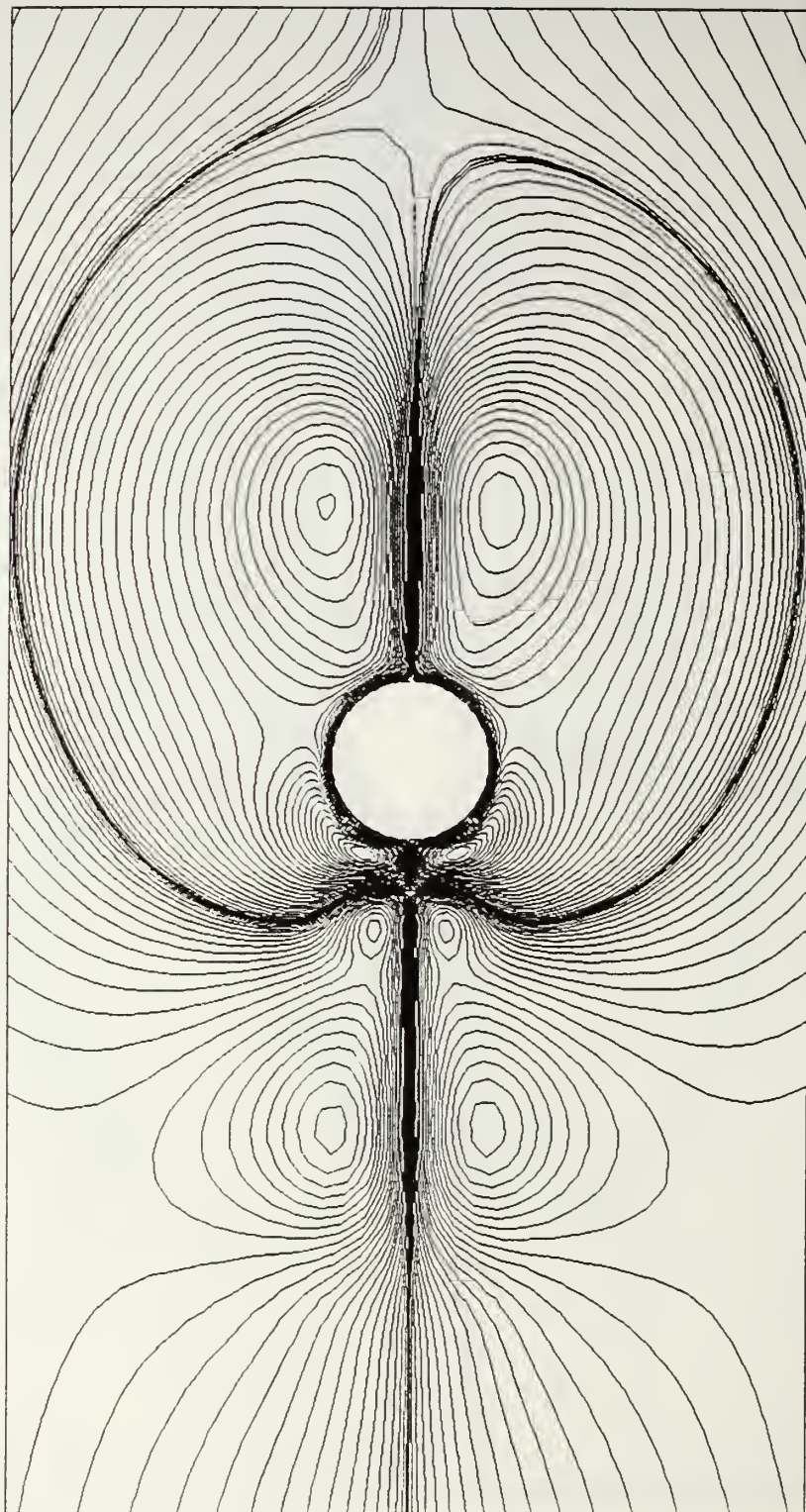


Figure 46. Streamlines (Relative Motion Ψ), $K = 3$, $\beta = 196$, $t/T = 6.5$

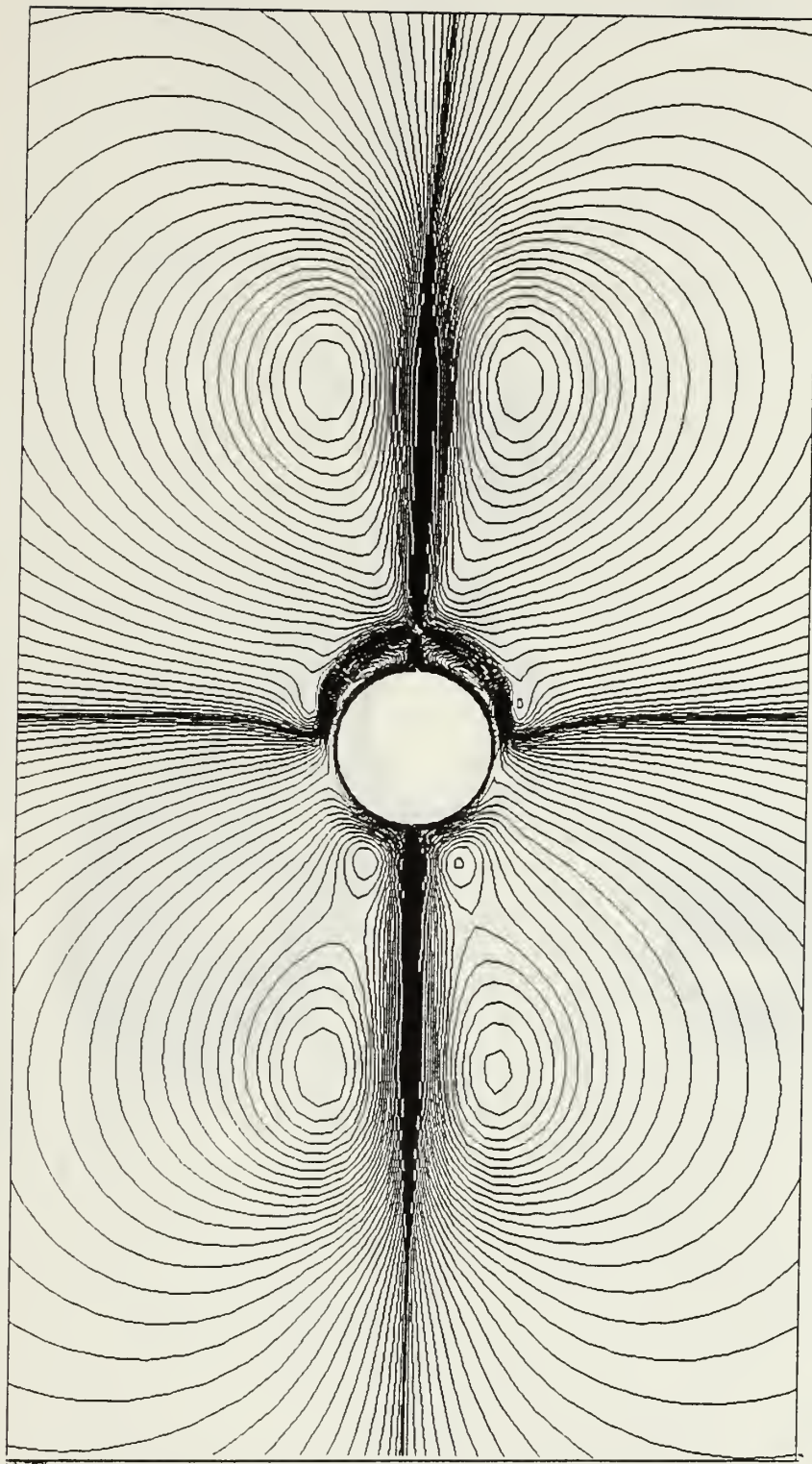


Figure 47. Streamlines (Relative Motion Ψ'), $K = 3$, $\beta = 196$, $t/T = 6.75$

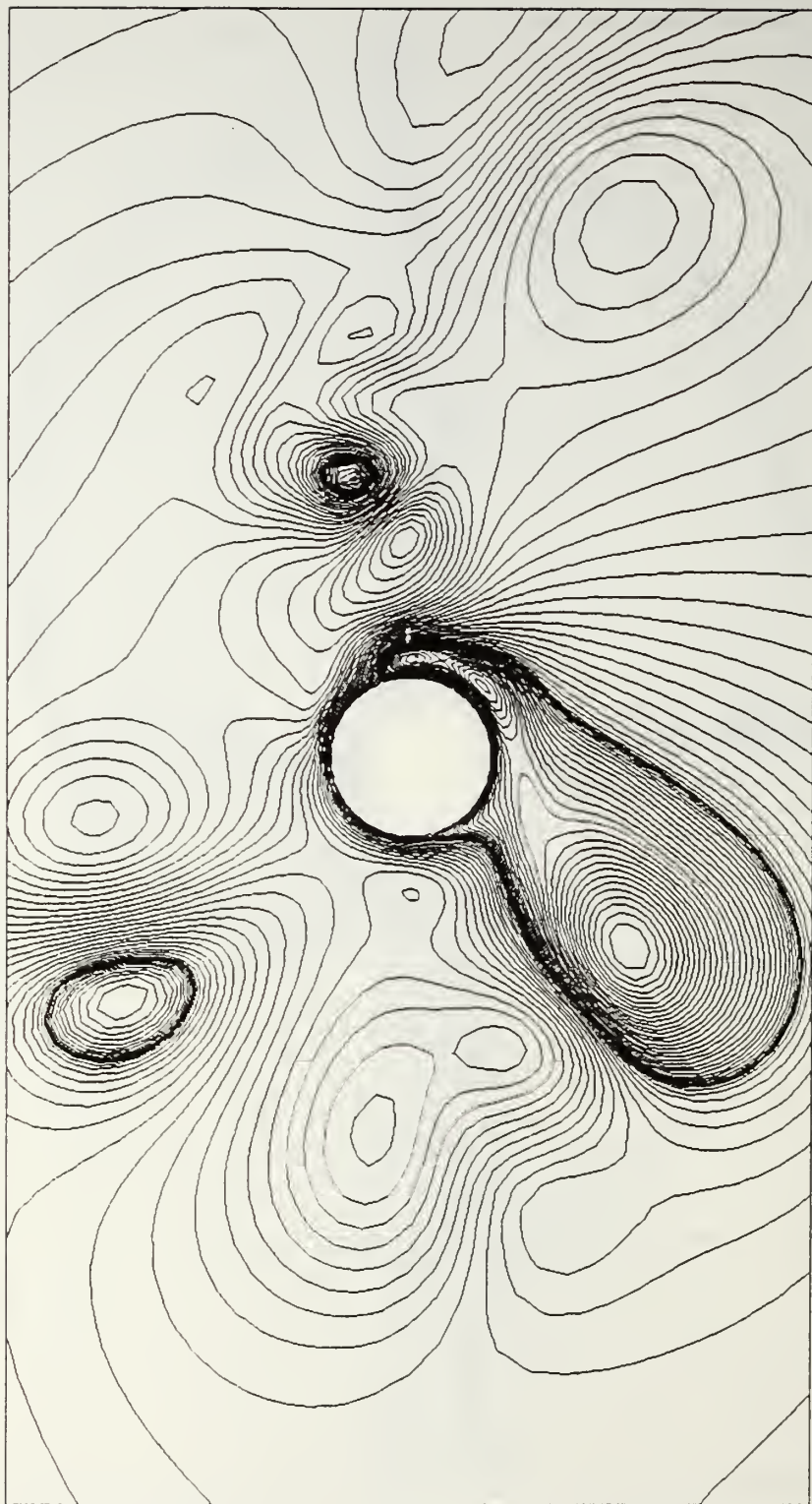


Figure 48. Streamlines (Total Ψ), $K = 4$, $\beta = 196$, $t/T = 6$

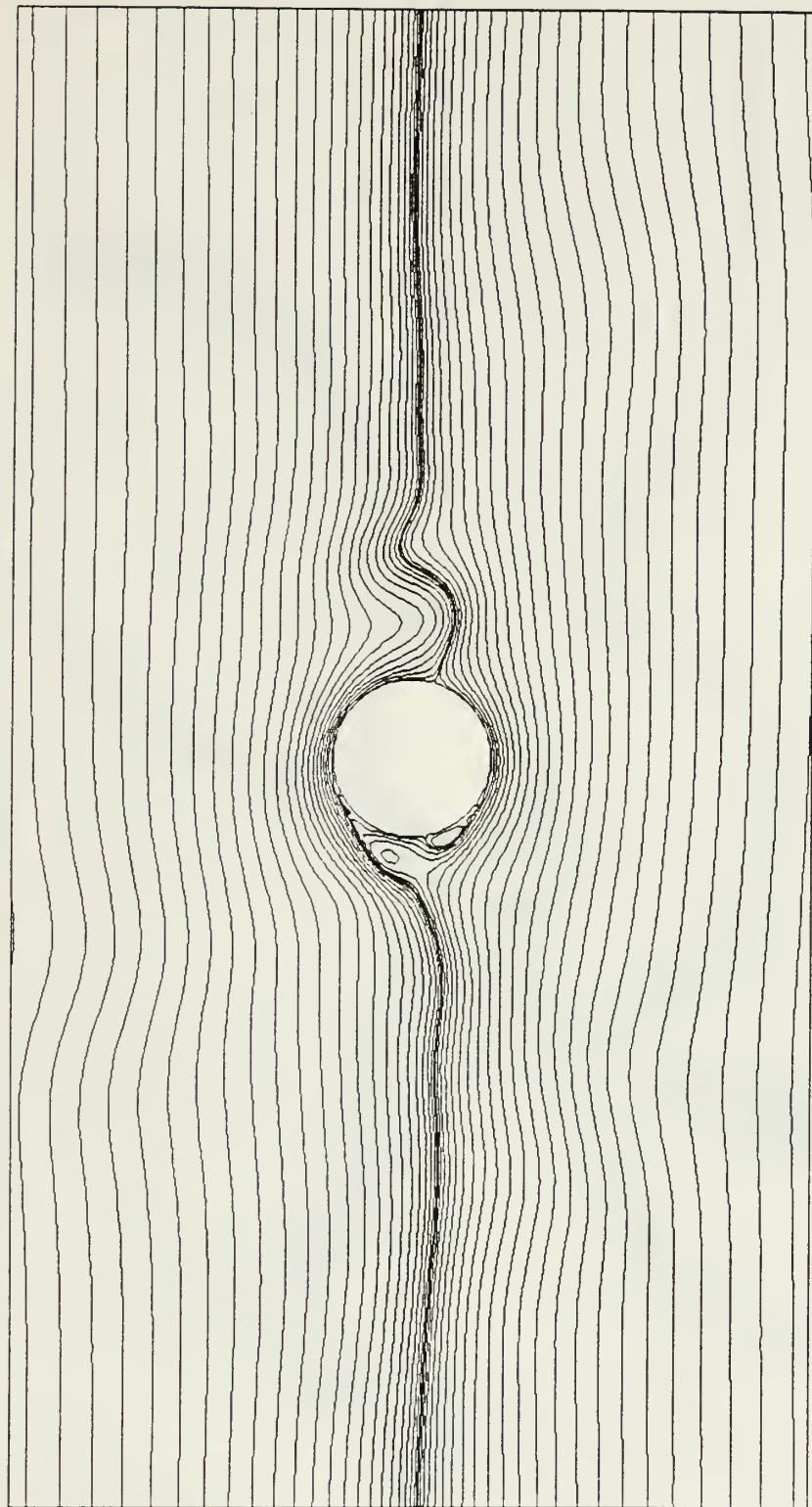


Figure 49. Streamlines (Total Ψ), $K = 4$, $\beta = 196$, $t/T = 6.25$

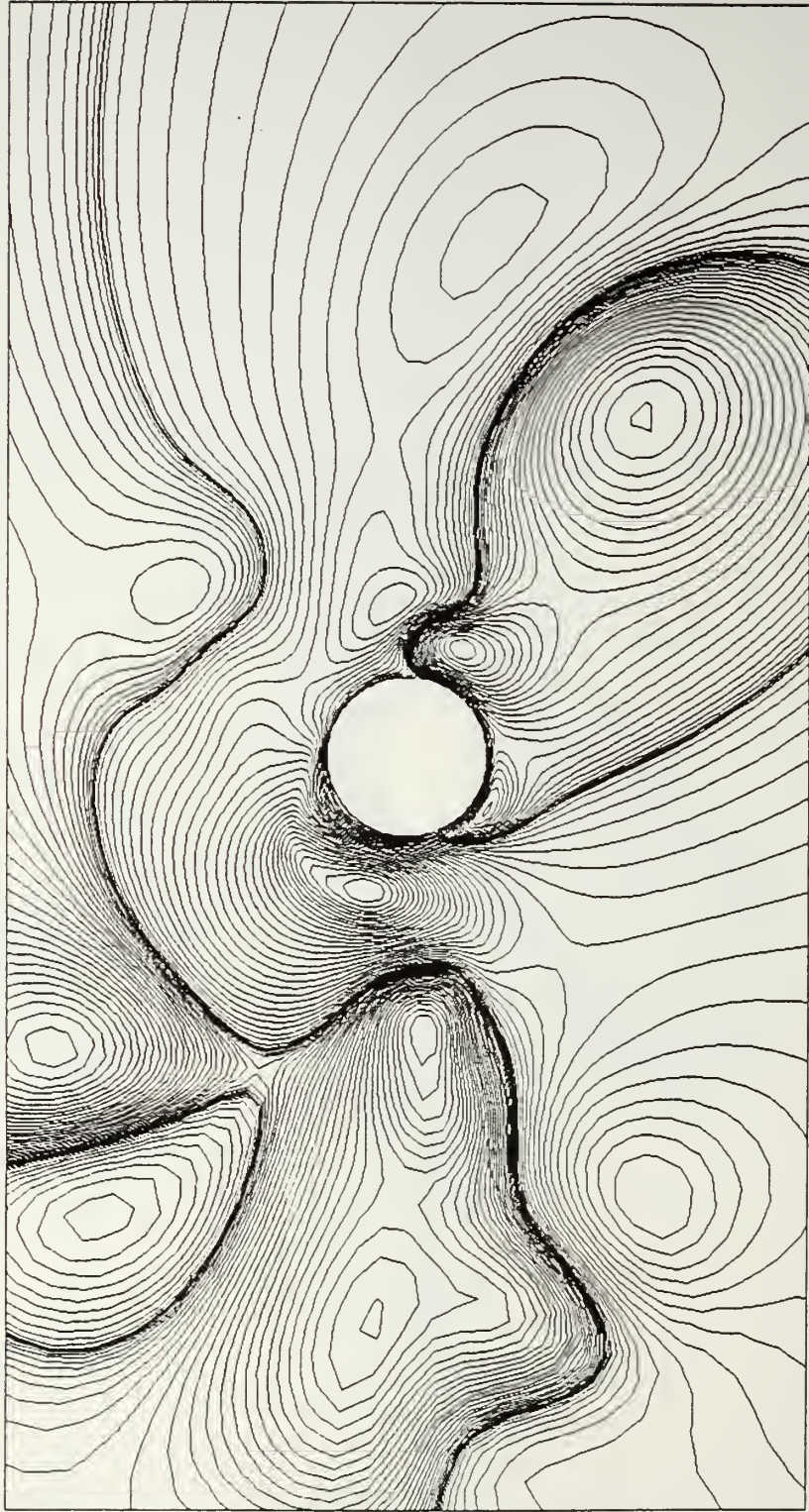


Figure 50. Streamlines (Total Ψ'), $K = 4$, $\beta = 196$, $t/T = 6.5$

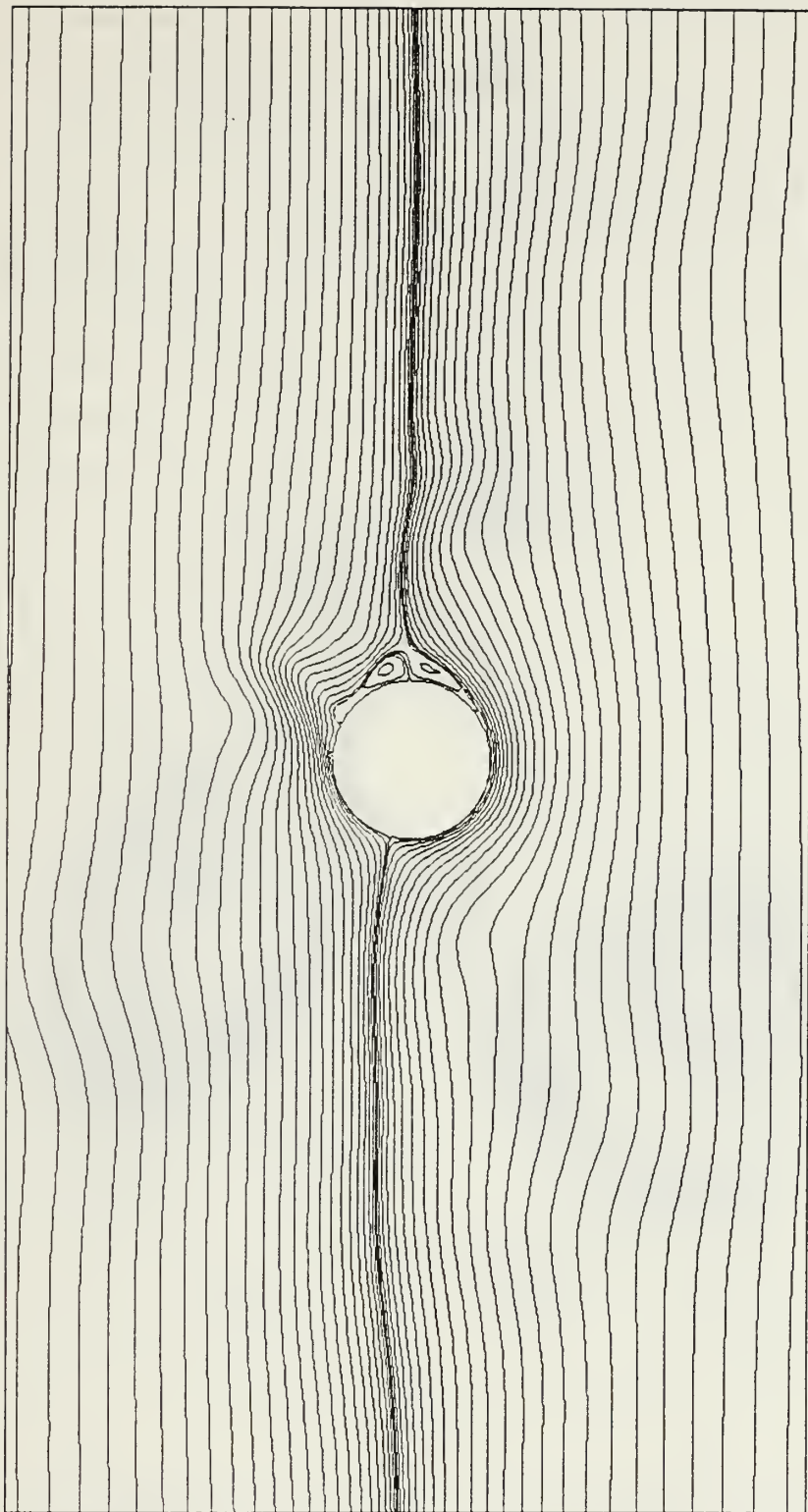


Figure 51. Streamlines (Total Ψ), $K = 4$, $\beta = 196$, $t/T = 6.75$

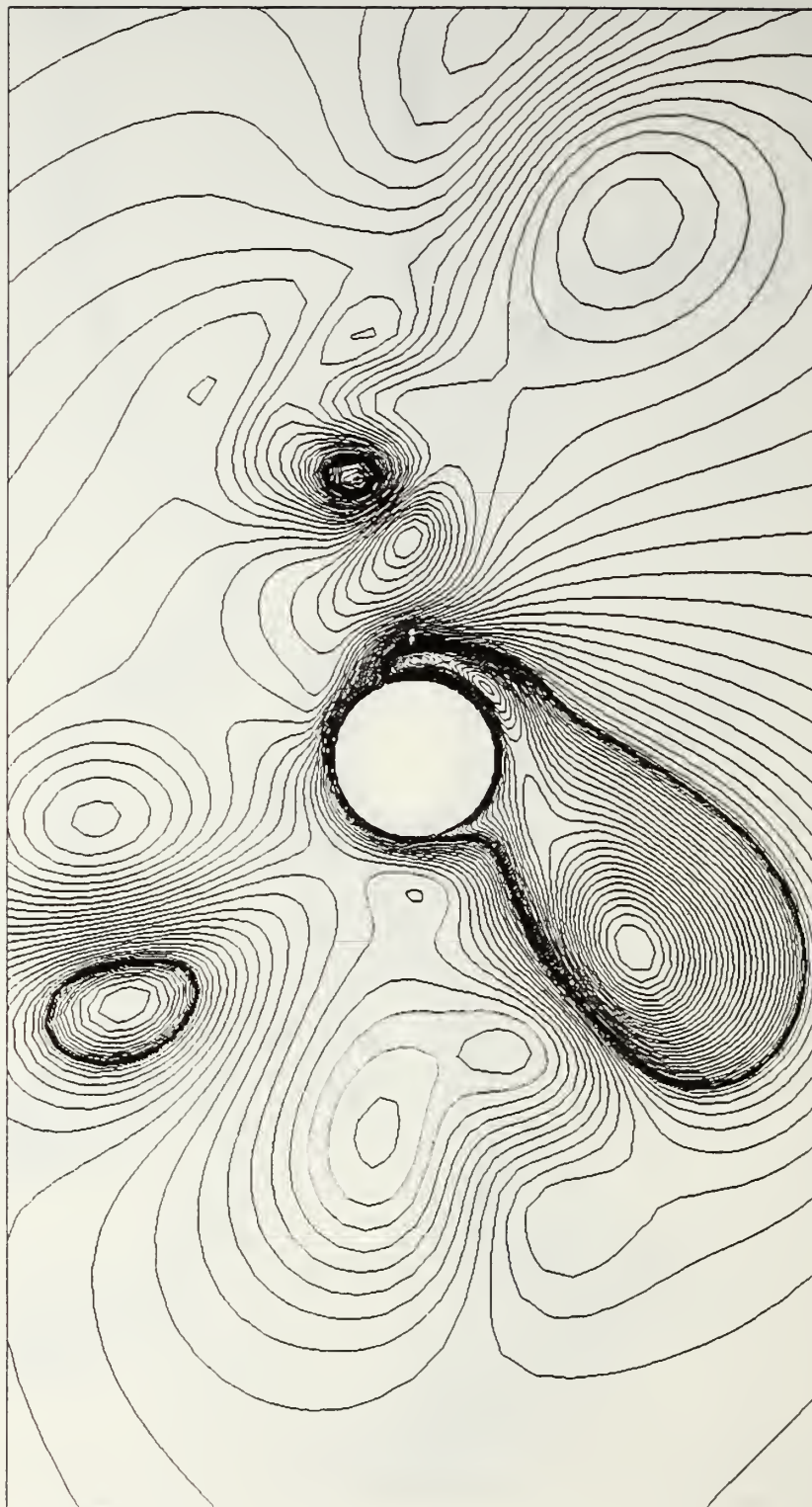


Figure 52. Streamlines (Relative Motion Ψ), $K = 4$, $\beta = 196$, $t/T = 6$

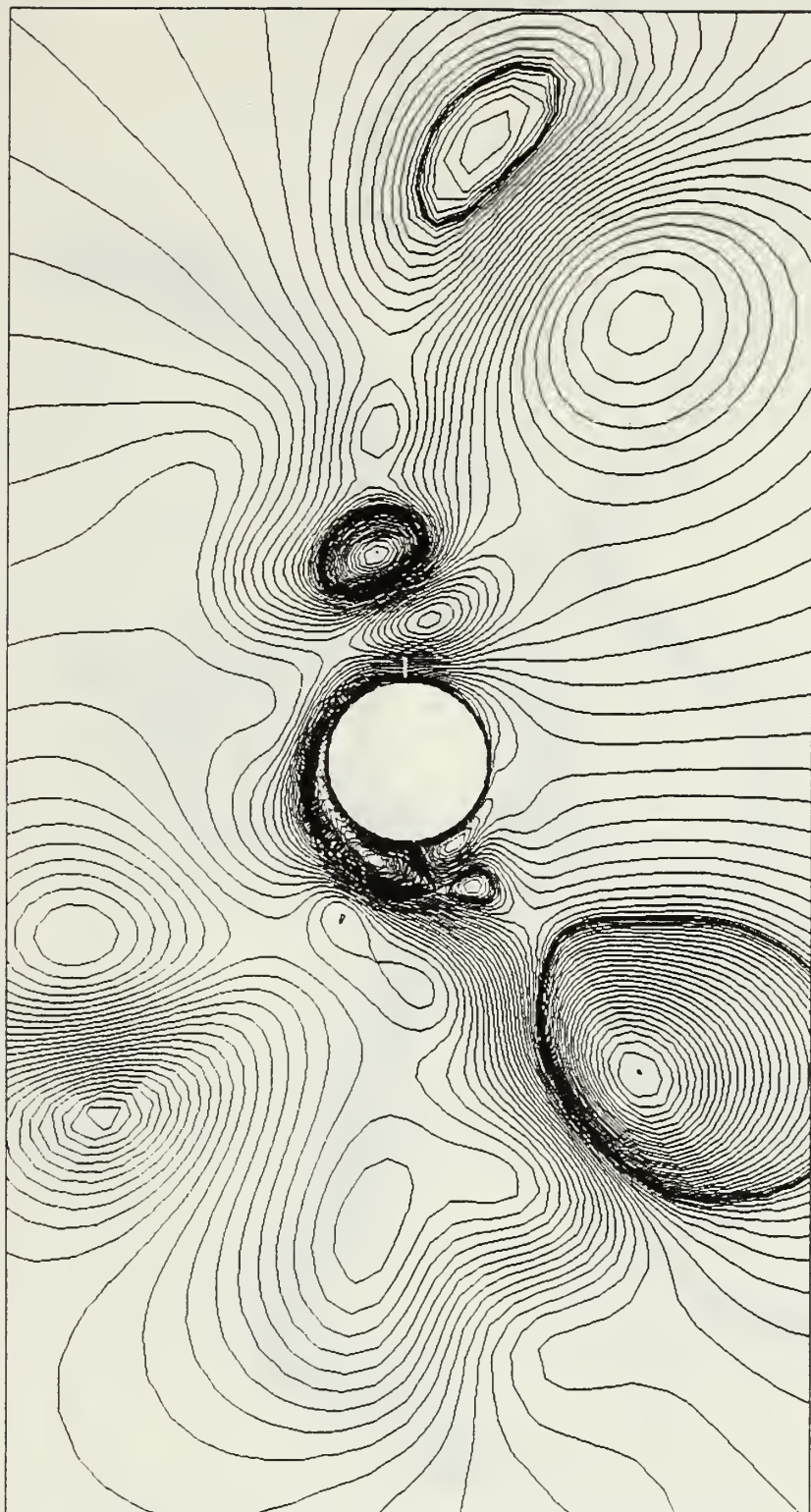


Figure 53. Streamlines (Relative Motion Ψ), $K = 4$, $\beta = 196$, $t/T = 6.25$

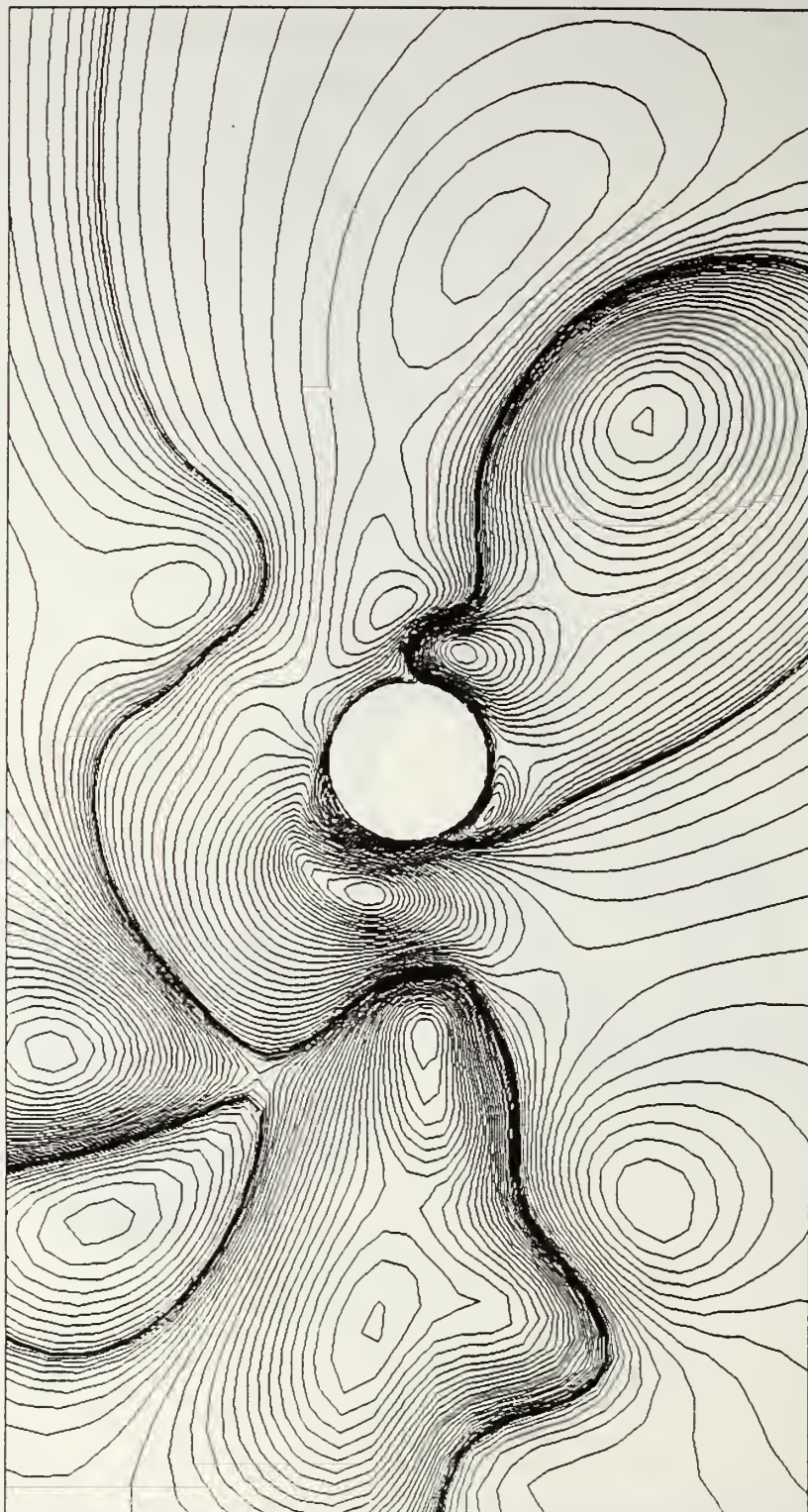


Figure 54. Streamlines (Relative Motion Ψ), $K = 4$, $\beta = 196$, $t/T = 6.5$

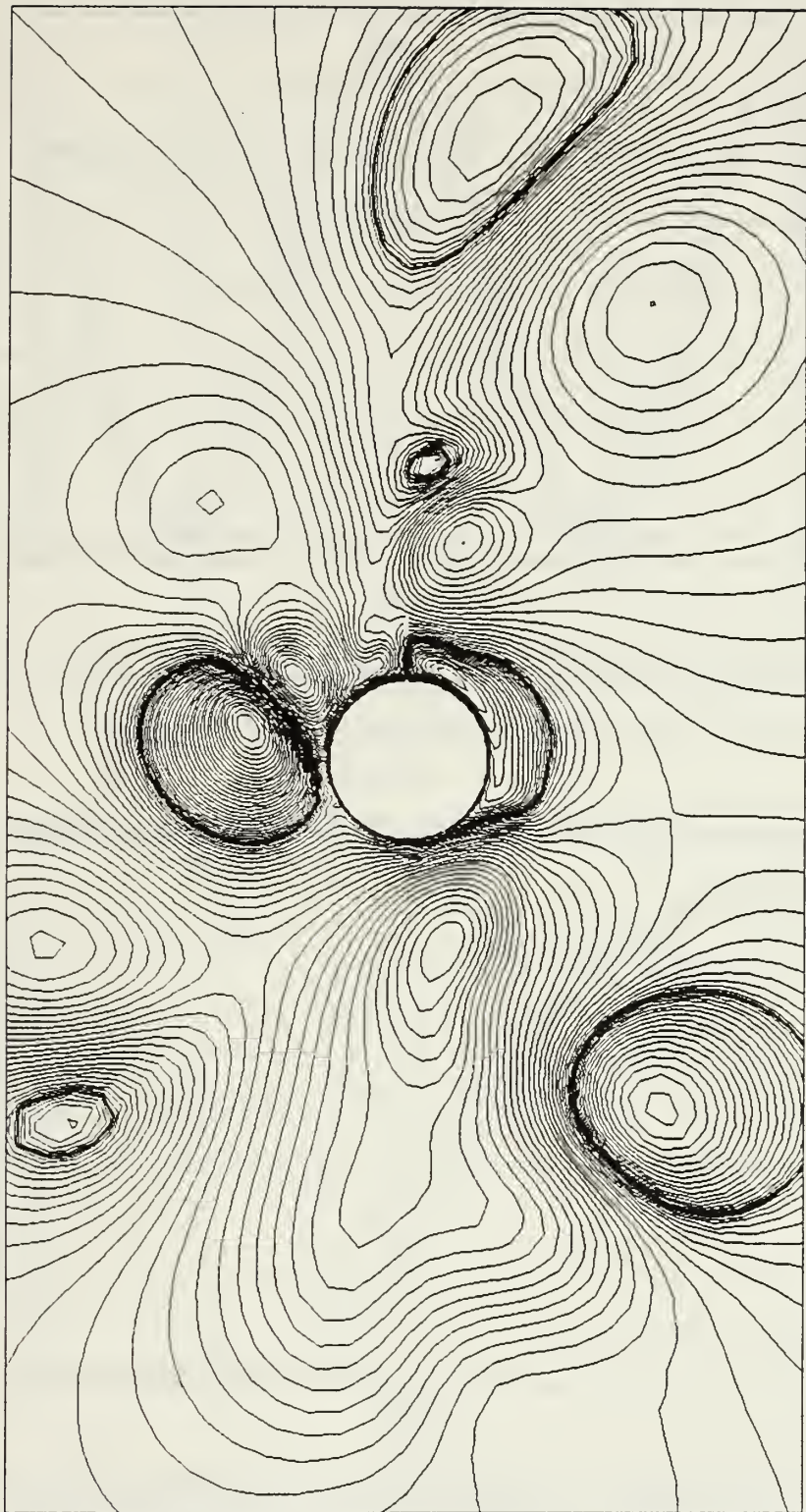


Figure 55. Streamlines (Relative Motion Ψ), $K = 4$, $\beta = 196$, $t/T = 6.75$

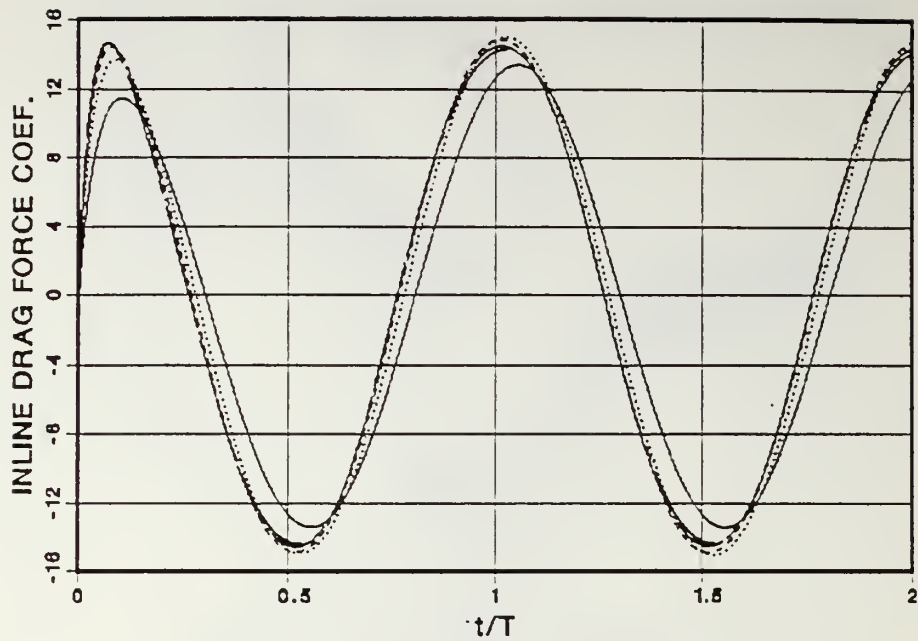


Figure 56a. C_{IL} versus t/T , $K = 1.5$, $\beta = 300$, — : $n = 2$, : $n = 4$,
 - - - : $n = 6$, — · — : $n = 8$, — — — : $n = 10$

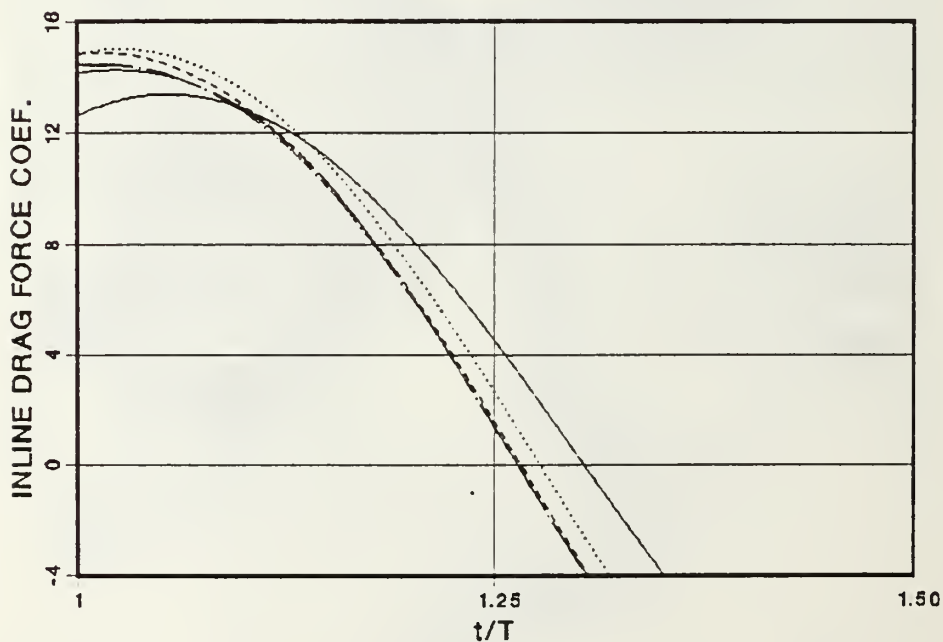


Figure 56b. C_{IL} versus t/T , (Close-up of Figure 56a)

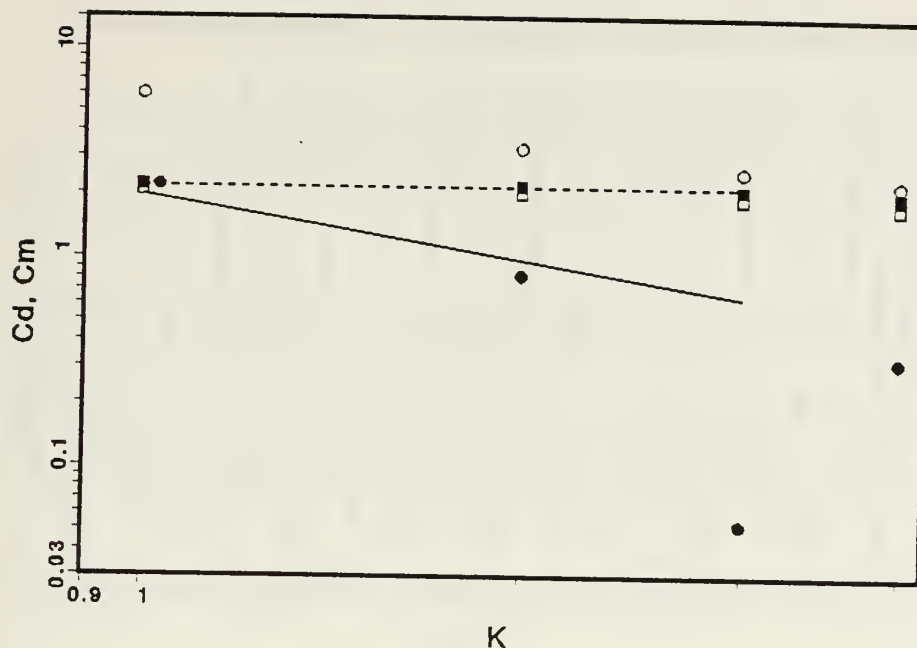


Figure 57a. C_d and C_m , versus K , C_d : for $n = 2$ (open circles),
 C_d : for $n = 8$ (full circles), C_m : for $n = 2$ (open squares),
 C_m : for $n = 8$ (full squares),: C_m (Theory),
 — : C_d (Theory)

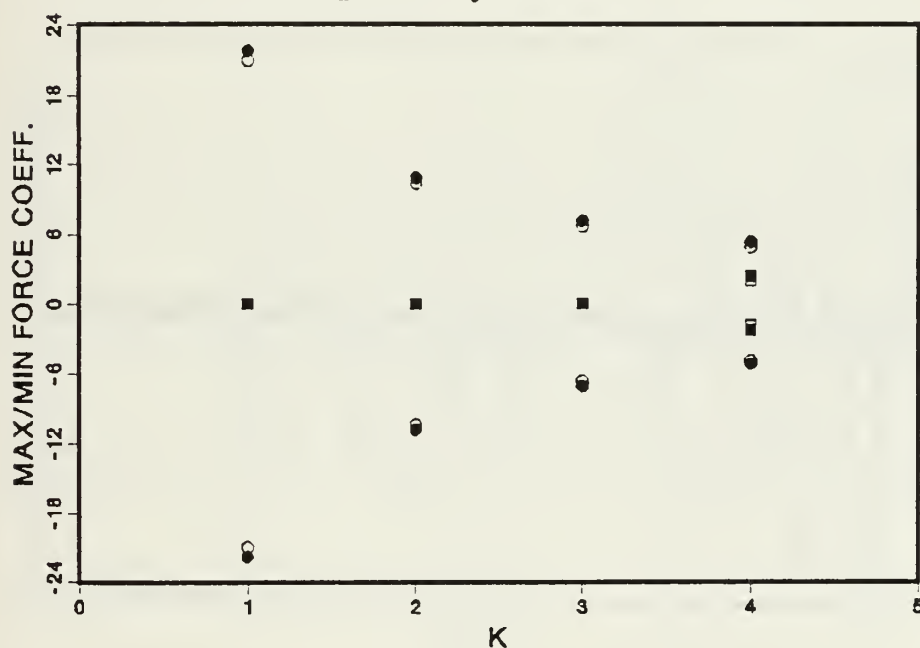


Figure 57b. C_{IL} and C_L , versus K , C_{IL} : for $n = 2$ (open circles),
 C_{IL} : for $n = 8$ (full circles), C_L : for $n = 2$ (open squares),
 C_L : for $n = 8$ (full squares)

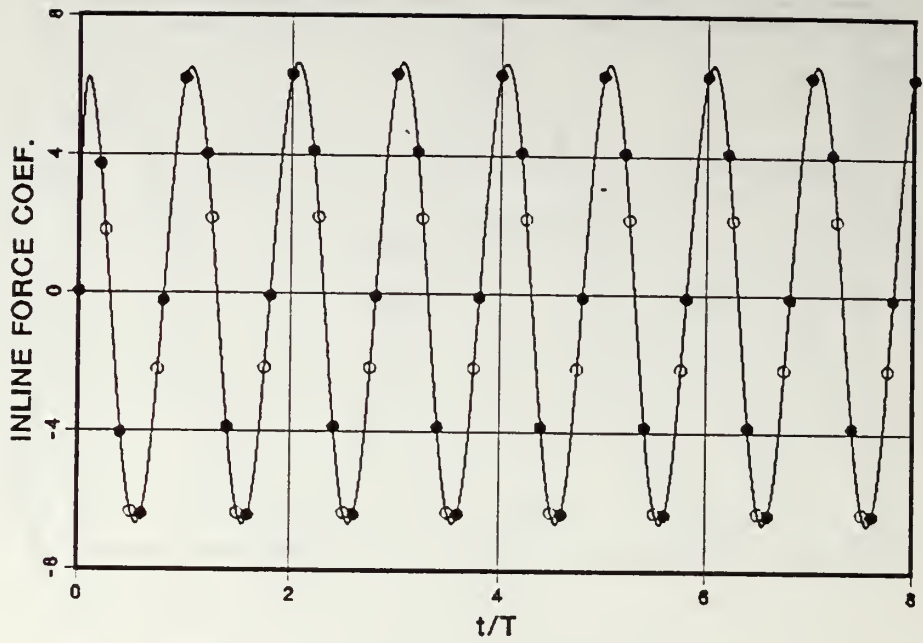


Figure 58a. C_{IL} versus t/T , $K = 3$, $\beta = 196$, $\Delta\alpha = 0.5$ (open circles), $\Delta\alpha = 5.0$ (full circles)

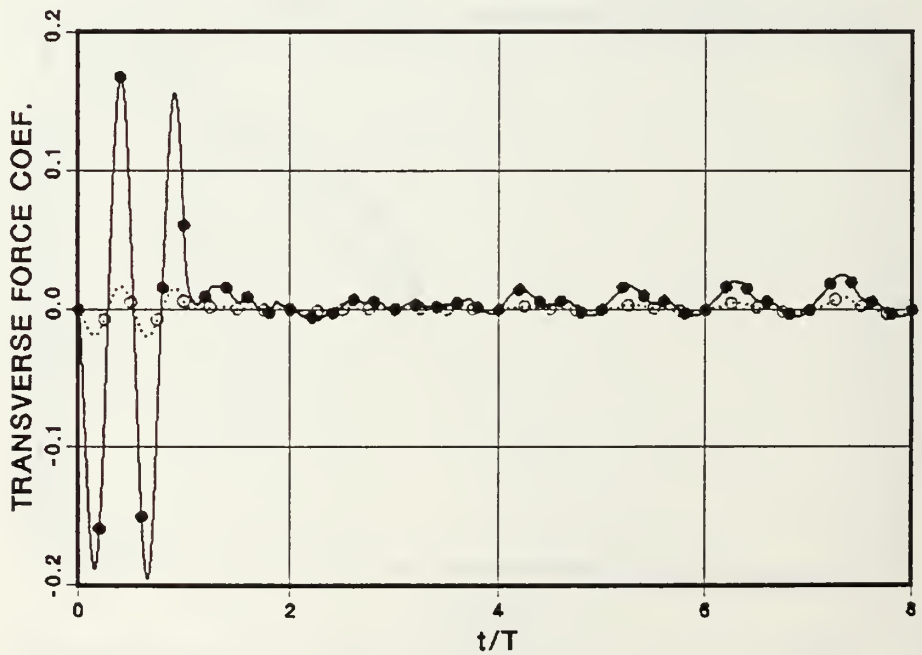


Figure 58b. C_L versus t/T , $K = 3$, $\beta = 196$, $\Delta\alpha = 0.5$ (open circles), $\Delta\alpha = 5.0$ (full circles)

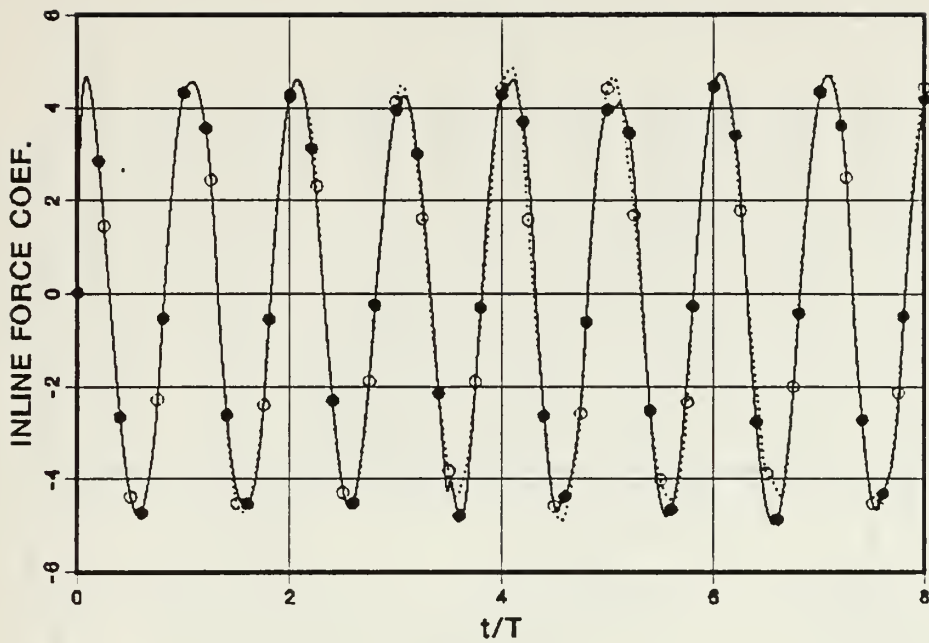


Figure 59a. C_{IL} versus t/T , $K = 4$, $\beta = 196$, $\Delta\alpha = 0.5$ (open circles),
 $\Delta\alpha = 5.0$ (full circles)

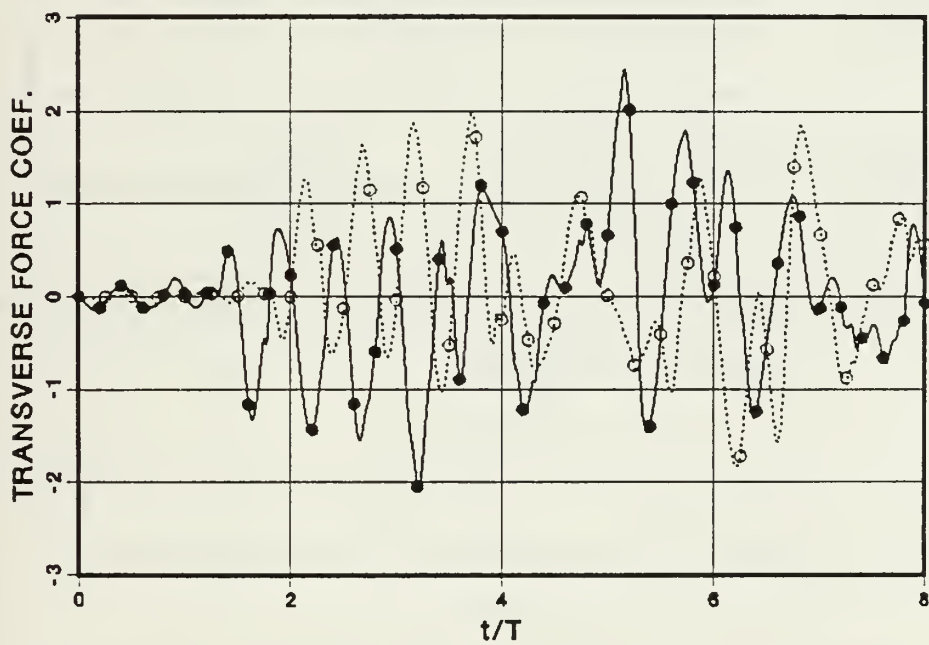


Figure 59b. C_L versus t/T , $K = 4$, $\beta = 196$, $\Delta\alpha = 0.5$ (open circles),
 $\Delta\alpha = 5.0$ (full circles)

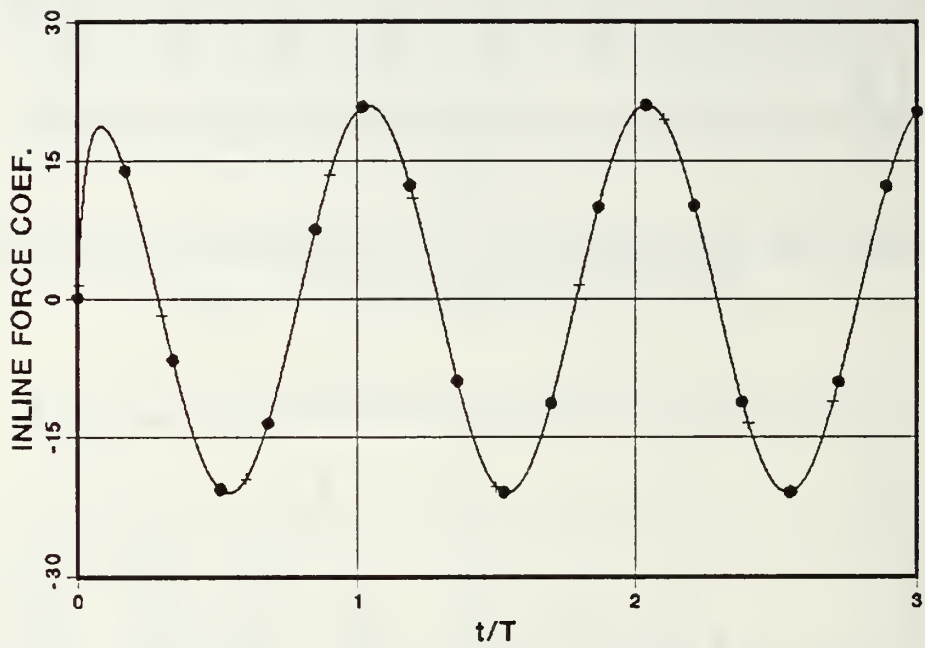


Figure 60. C_{IL} versus t/T , $K = 1$, with CRAY, $\beta = 450$, $\Delta t = 0.002$ (+),
 $\Delta t = 0.0001$ (full circles)

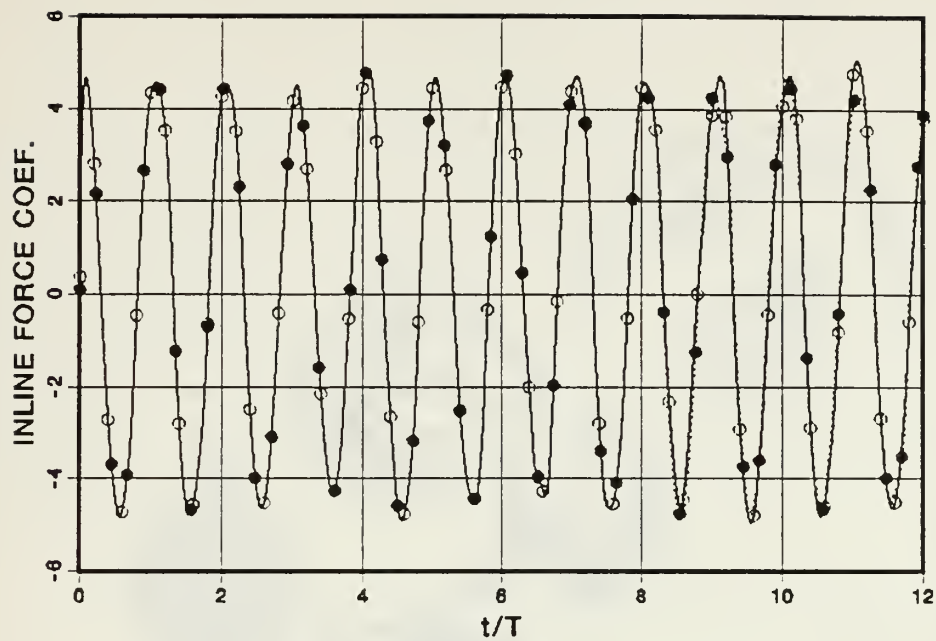


Figure 61a. C_{IL} versus t/T , $K=4$, $\beta = 196$, $\Delta t = 0.002$ (open circles),
 $\Delta t=0.0005$ (full circles)

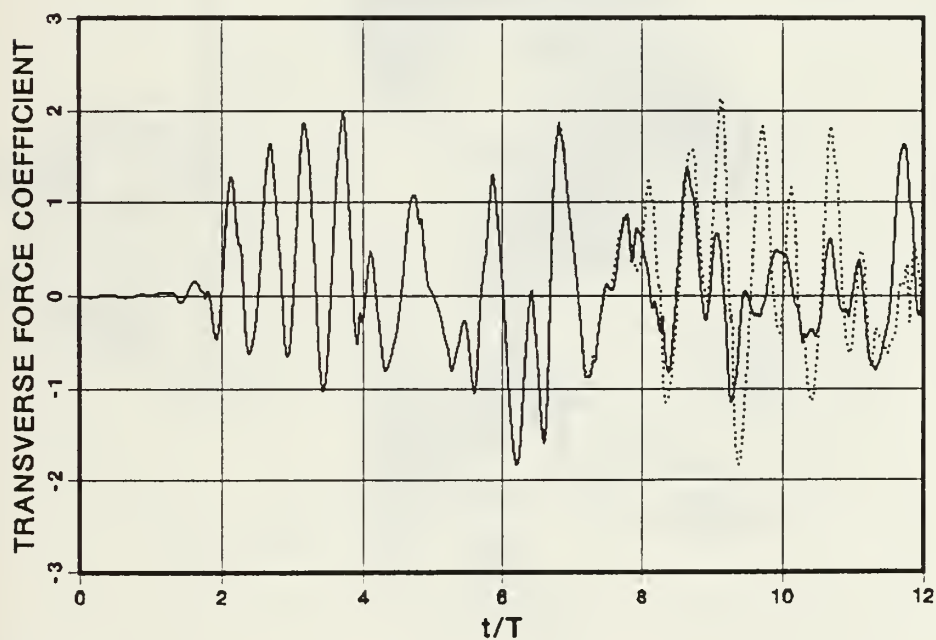


Figure 61b. C_L versus t/T , $K = 4$, $\beta = 196$, — : $\Delta t = 0.002$,
 : $\Delta t = 0.0005$



Figure 62. Streaklines, $K = 4$, $\beta = 196$, $\Delta t = 0.0005$, $t\Gamma = 4$

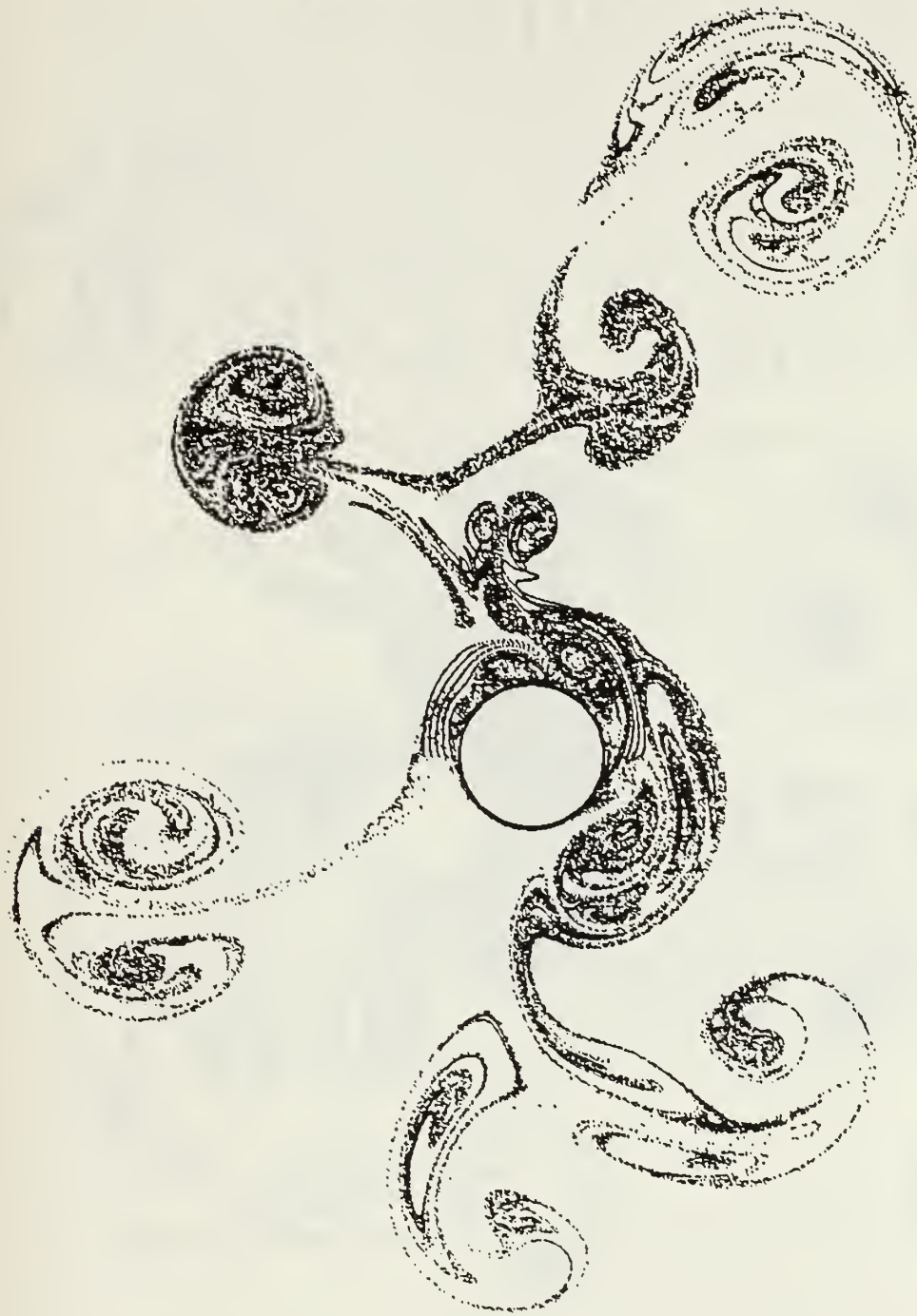


Figure 63 Streaklines, $K = 4$, $\beta = 196$, $\Delta t = 0.0005$, $t/T = 8$



Figure 64. Streaklines, $K = 4$, $\beta = 196$, $\Delta t = 0.0005$, $t/T = 12$

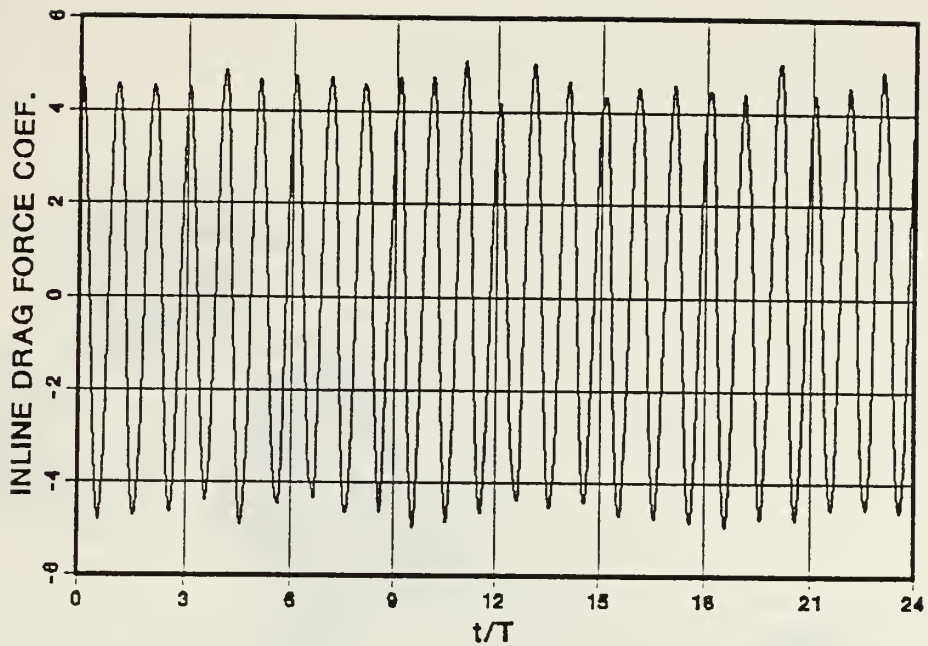


Figure 65. C_{IL} versus t/T , $K = 4$, $\beta = 196$, $\Delta t = 0.002$, $t/T = 24$

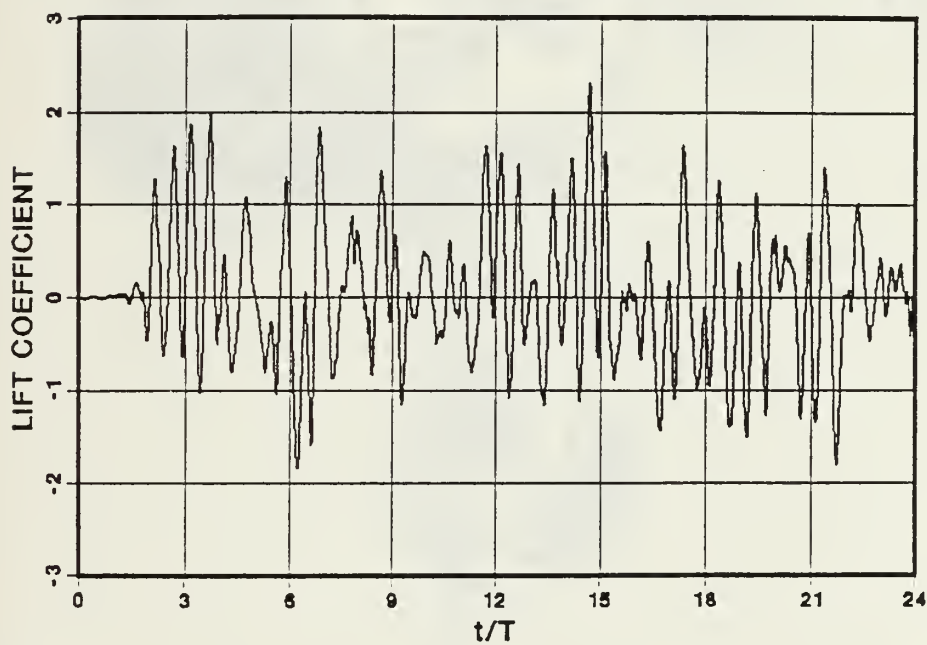


Figure 66. C_L versus t/T , $K = 4$, $\beta = 196$, $\Delta t = 0.002$, $t/T = 24$

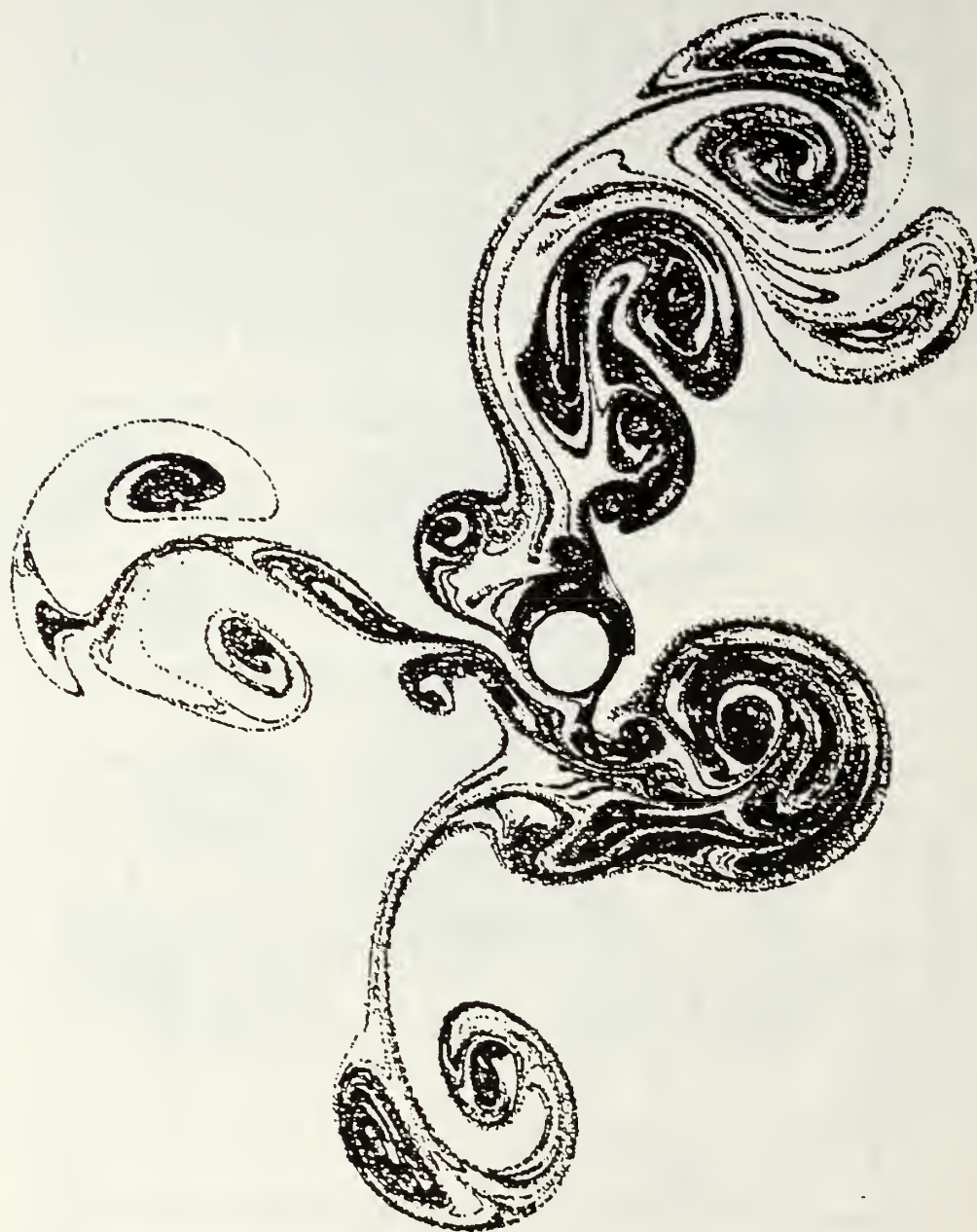


Figure 67. Streaklines, $K = 4$, $\beta = 196$, $\Delta t = 0.002$, $t/T = 24$

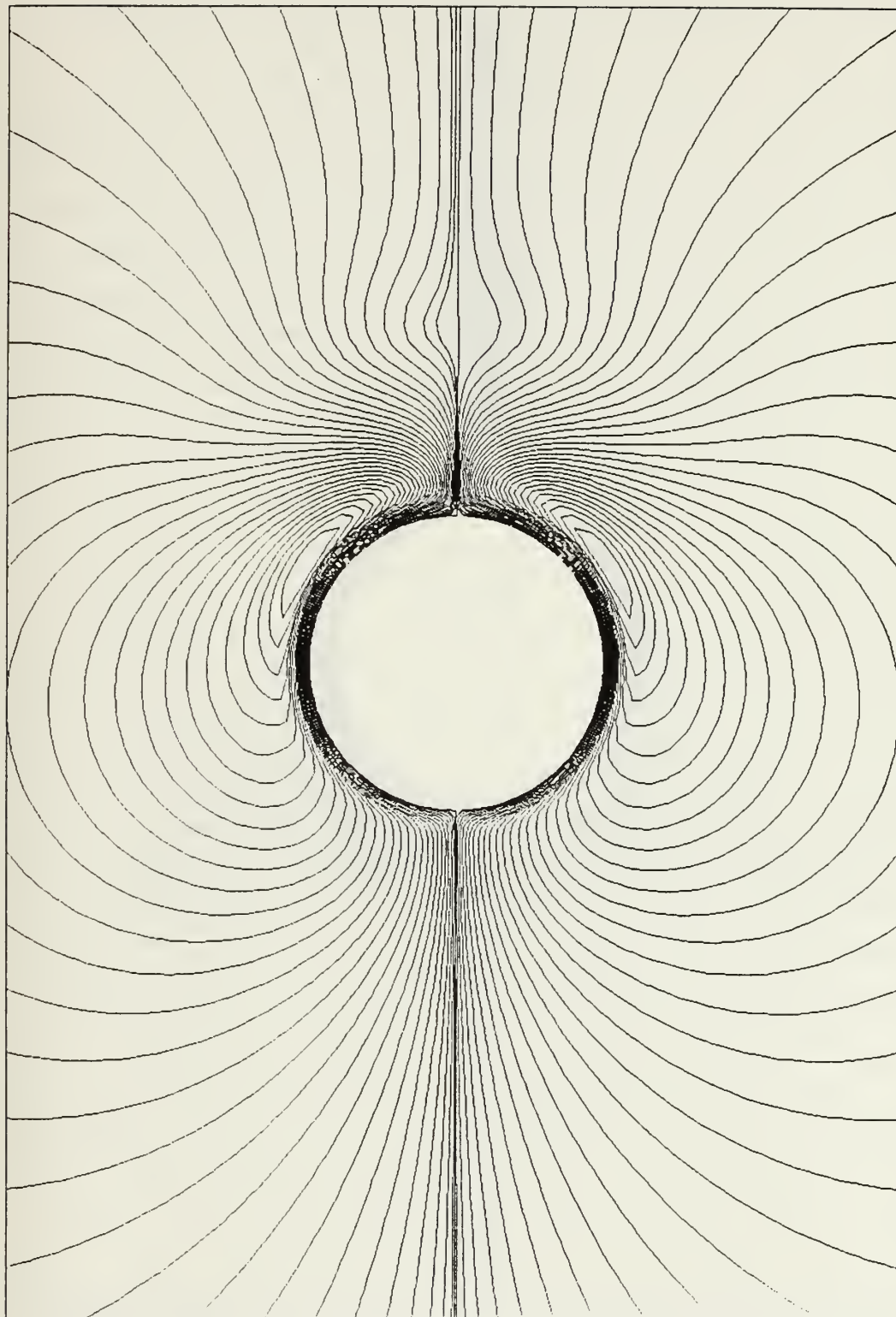


Figure 68. Streamlines (Relative Motion Ψ), $K = 1$, $\beta = 196$, $t/T = 7.00$

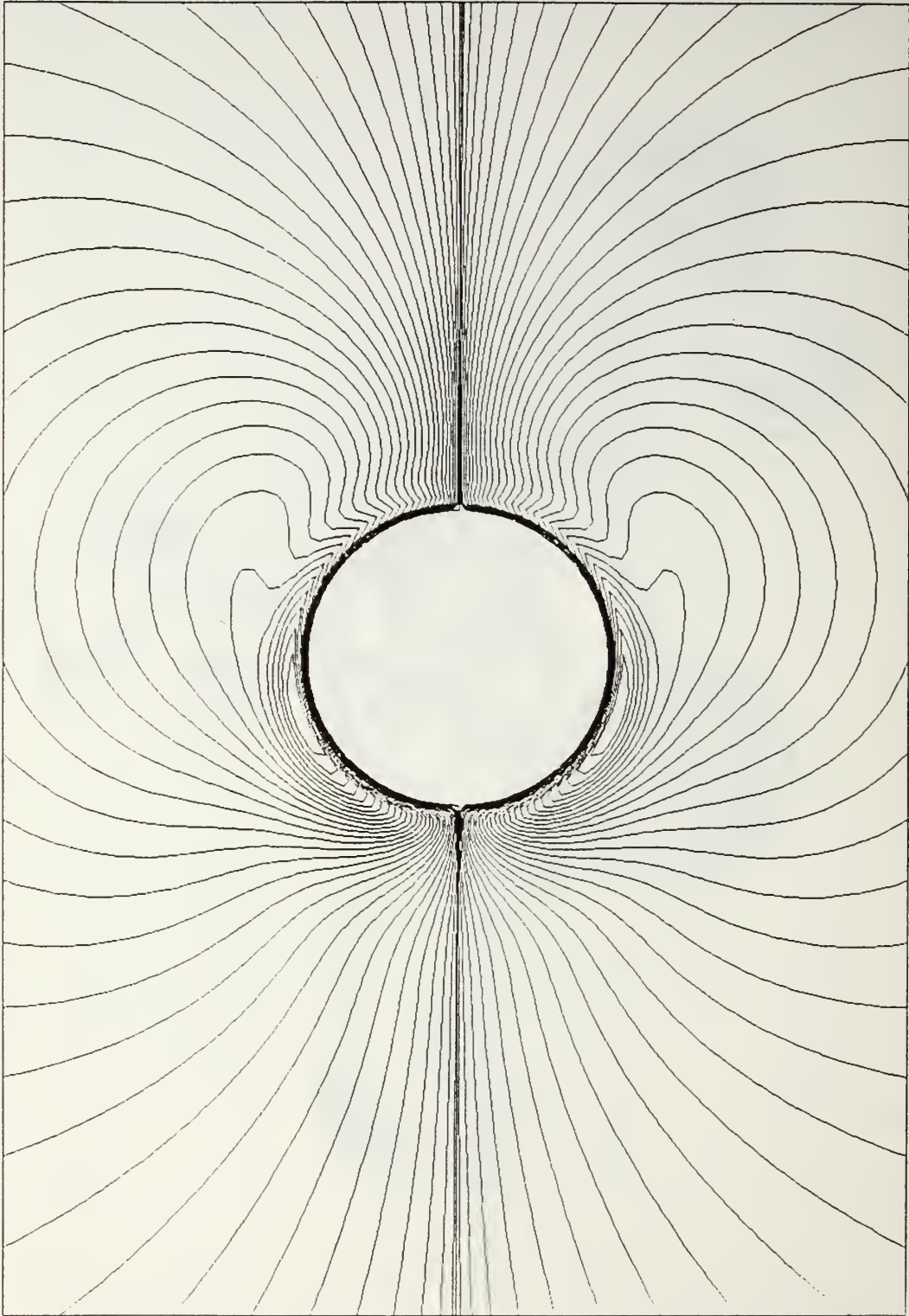


Figure 69. Streamlines (Relative Motion Ψ'), $K = 1$, $\beta = 196$, $t/T = 7.25$

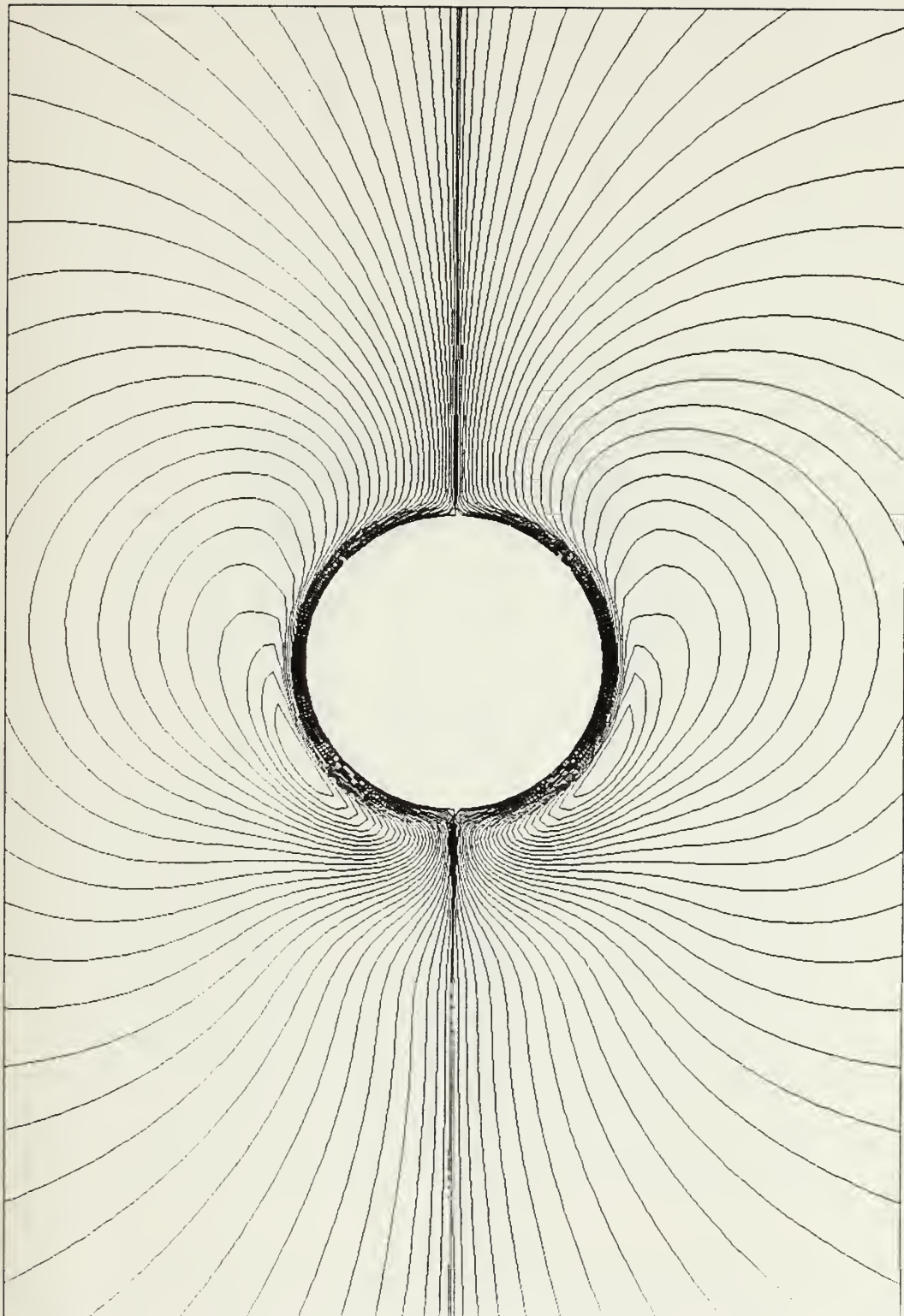


Figure 70. Streamlines (Relative Motion Ψ), $K = 1$, $\beta = 196$, $t/T = 7.50$

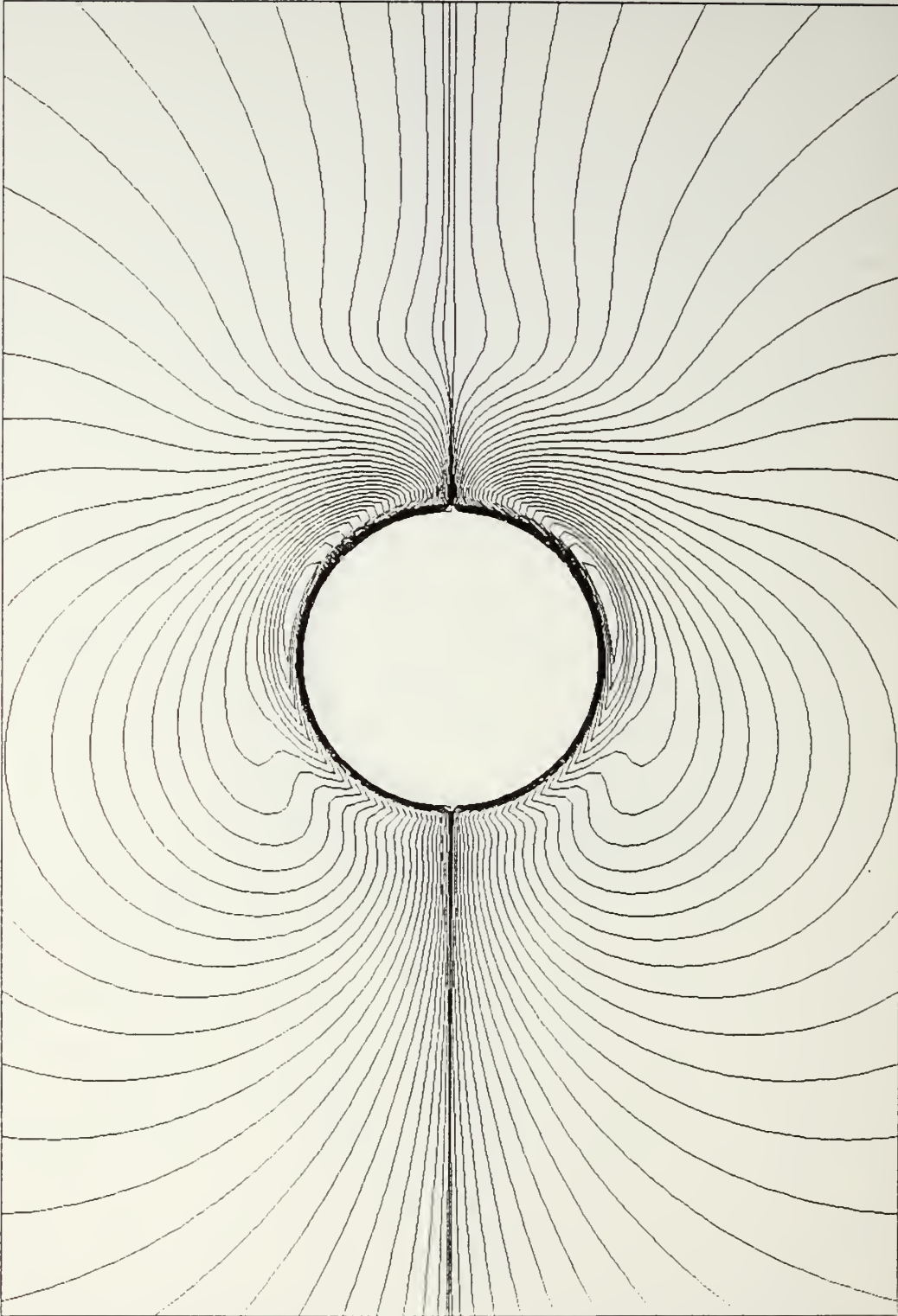


Figure 71. Streamlines (Relative Motion Ψ), $K = 1$, $\beta = 196$, $t/T = 7.75$

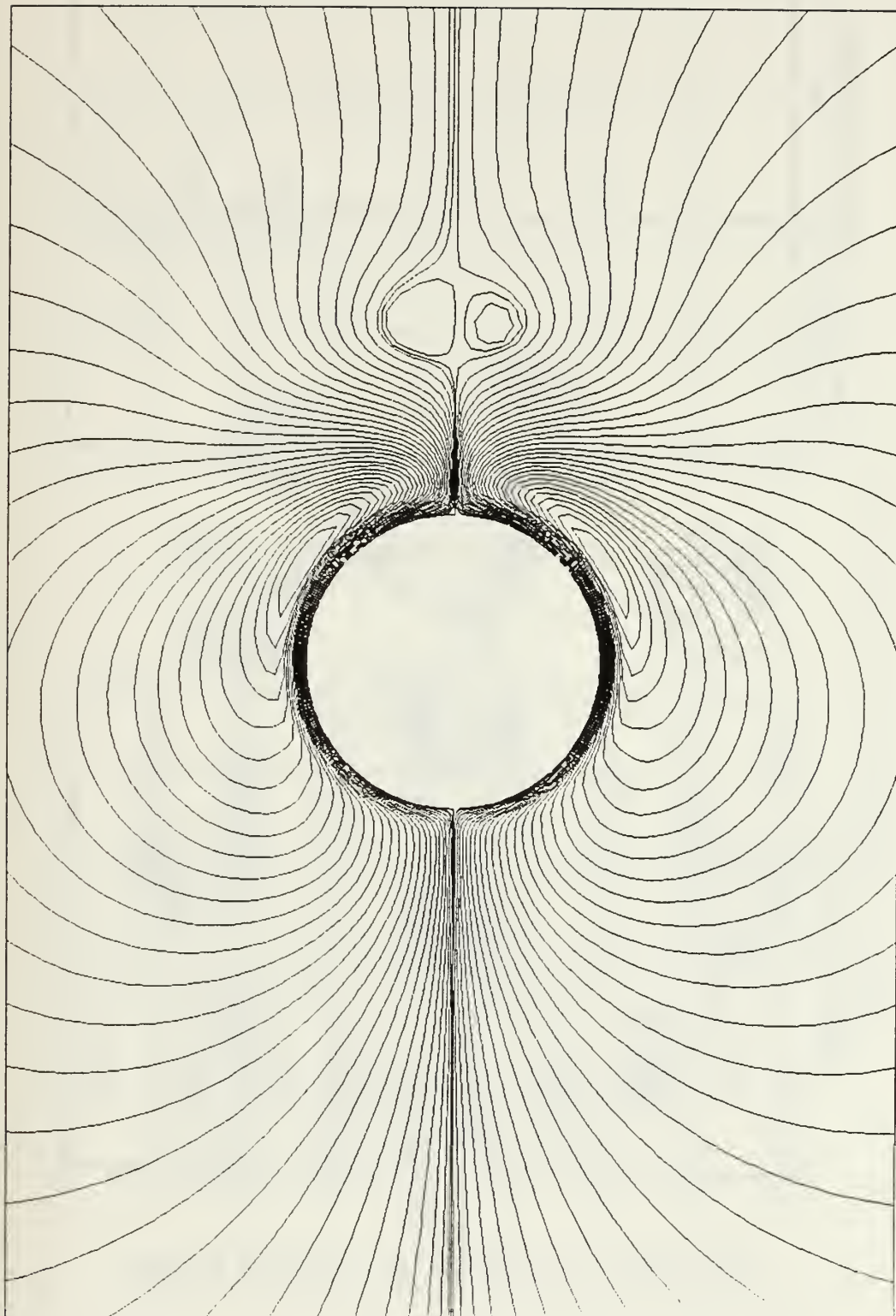


Figure 72. Streamlines (Relative Motion Ψ), $K = 1$, $\beta = 196$, $t/T = 8.00$

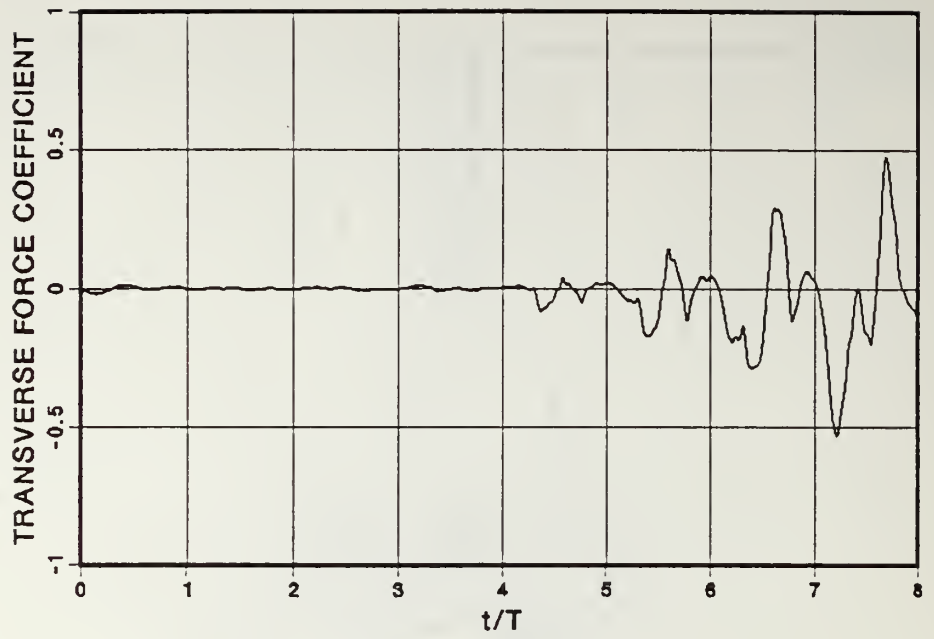


Figure 73. C_L versus t/T , $V_r = 0.4$ $K = 4$, $\beta = 196$

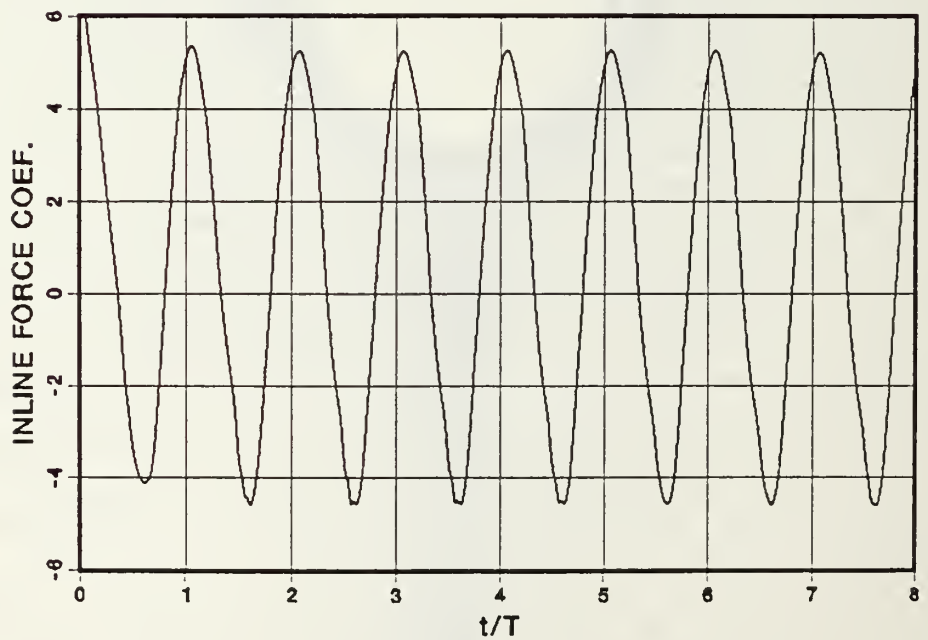


Figure 74. C_{IL} versus t/T , $V_r = 0.4$ $K = 4$, $\beta = 196$



Figure 75. Streaklines, $K = 4$, $\beta = 196$, $t/T = 8$

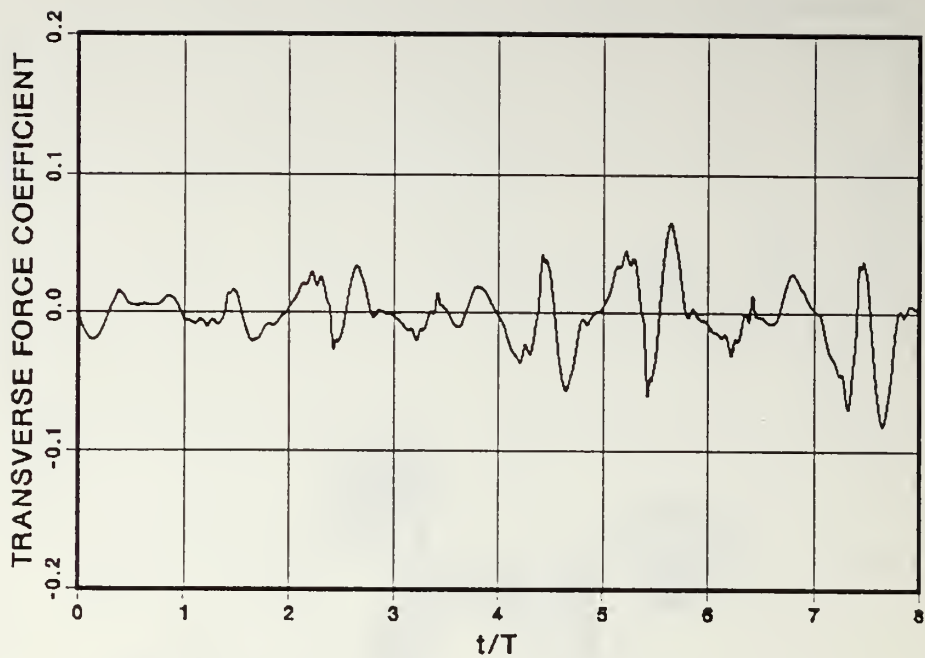


Figure 76. C_L versus t/T , $V_r = 0.6$, $K = 4$, $\beta = 196$

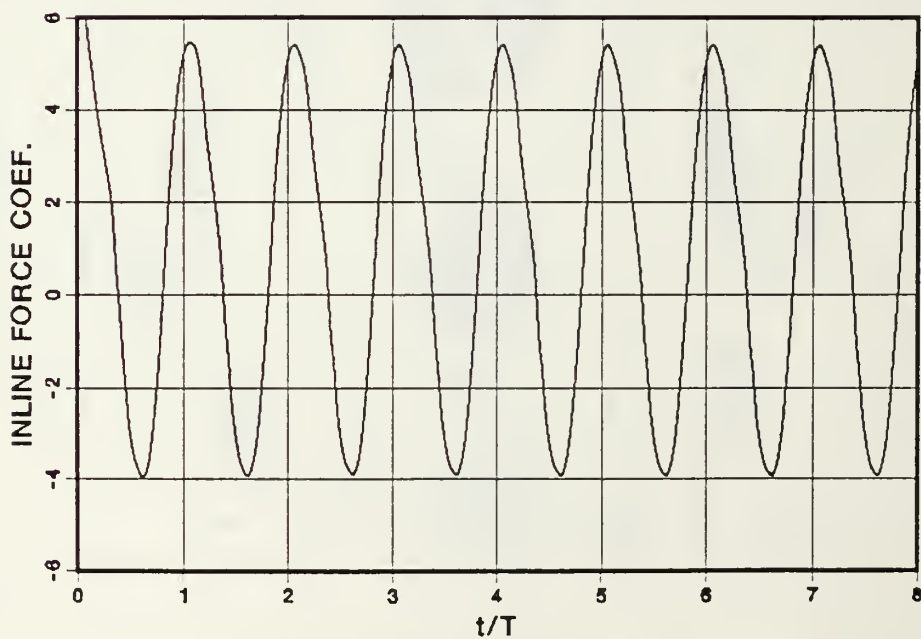


Figure 77. C_{IL} versus t/T , $V_r = 0.6$, $K = 4$, $\beta = 196$



Figure 78. Streaklines, $Vr = 0.6$, $K = 4$, $\beta = 196$, $t/T = 8$

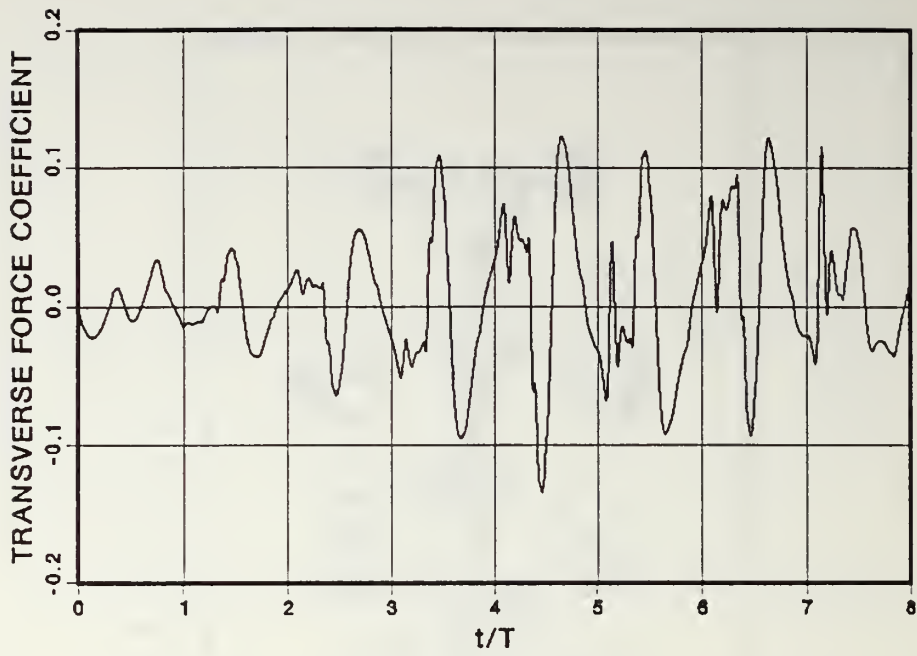


Figure 79. C_L versus t/T , $V_r = 0.8$, $K = 4$, $\beta = 196$

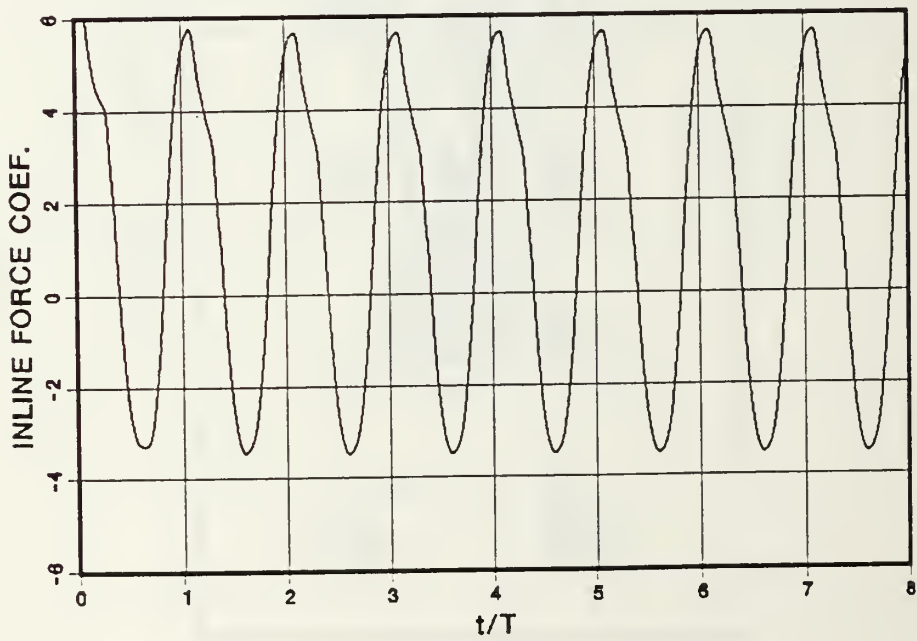


Figure 80. C_{IL} versus t/T , $V_r = 0.8$, $K = 4$, $\beta = 196$

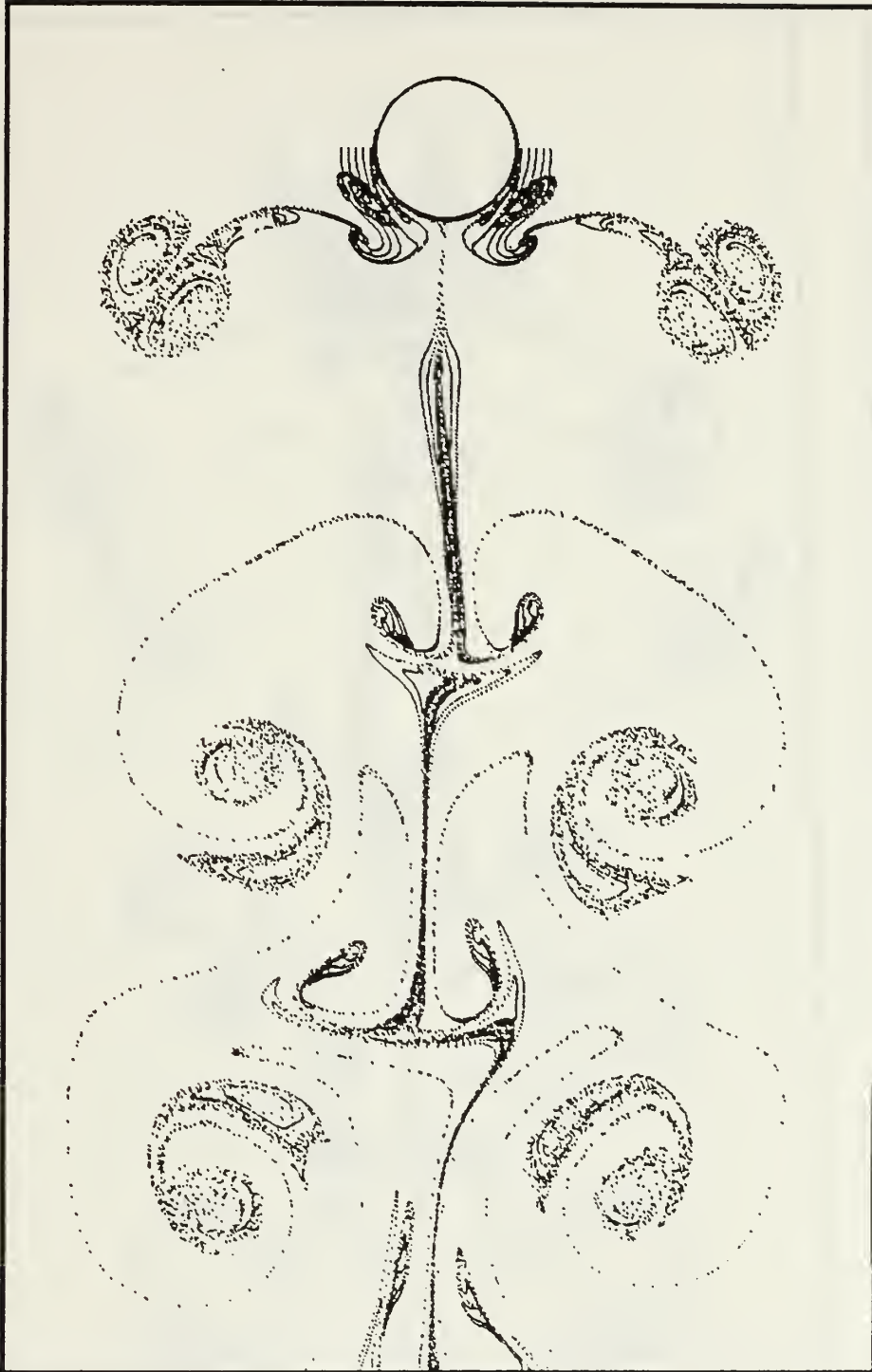


Figure 81. Streaklines, $V_r = 0.8$, $K = 4$, $\beta = 196$, $t/T = 8-1/8$

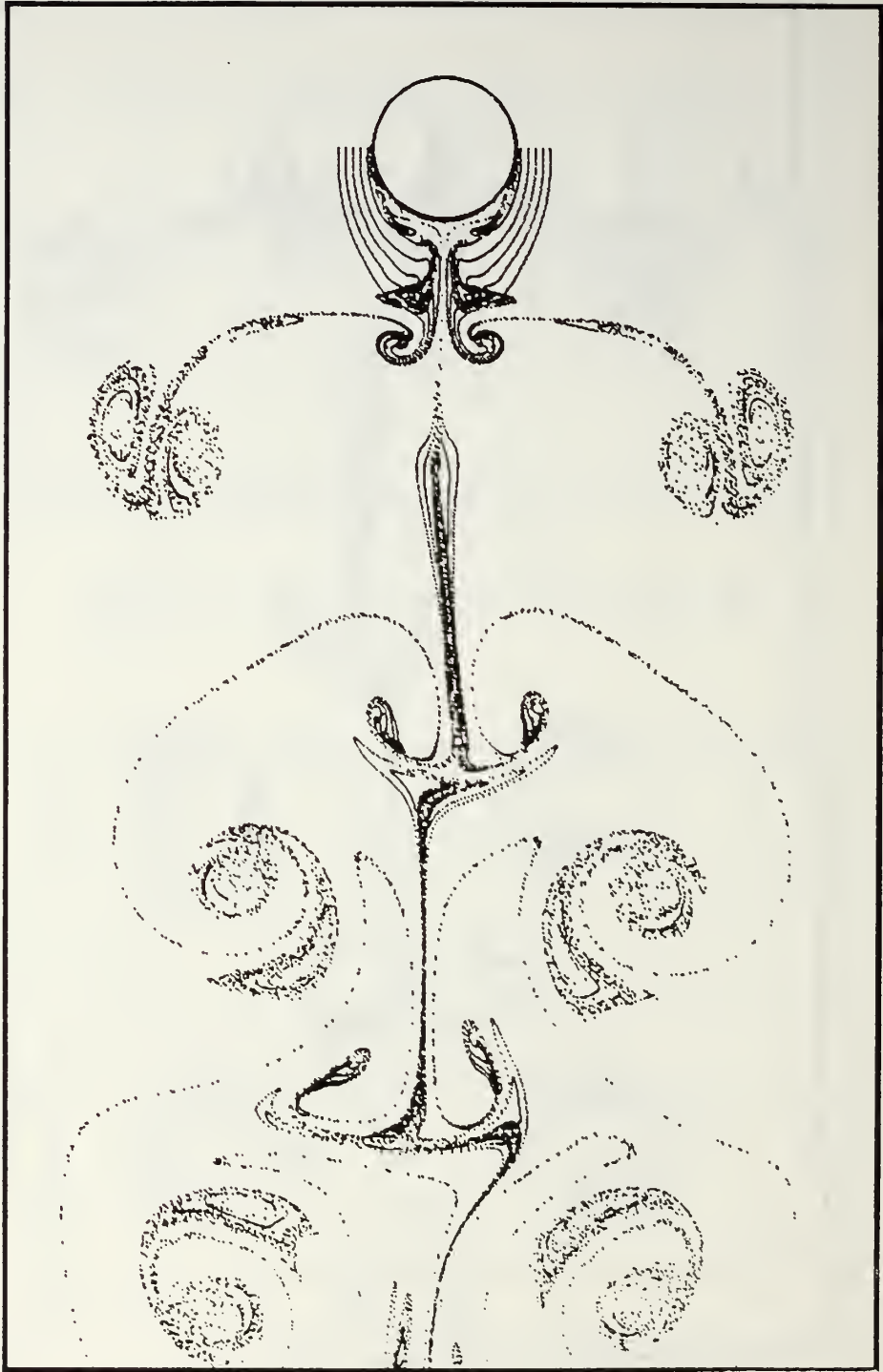


Figure 82. Streaklines, $V_r = 0.8$, $K = 4$, $\beta = 196$, $t/T = 8.2/8$

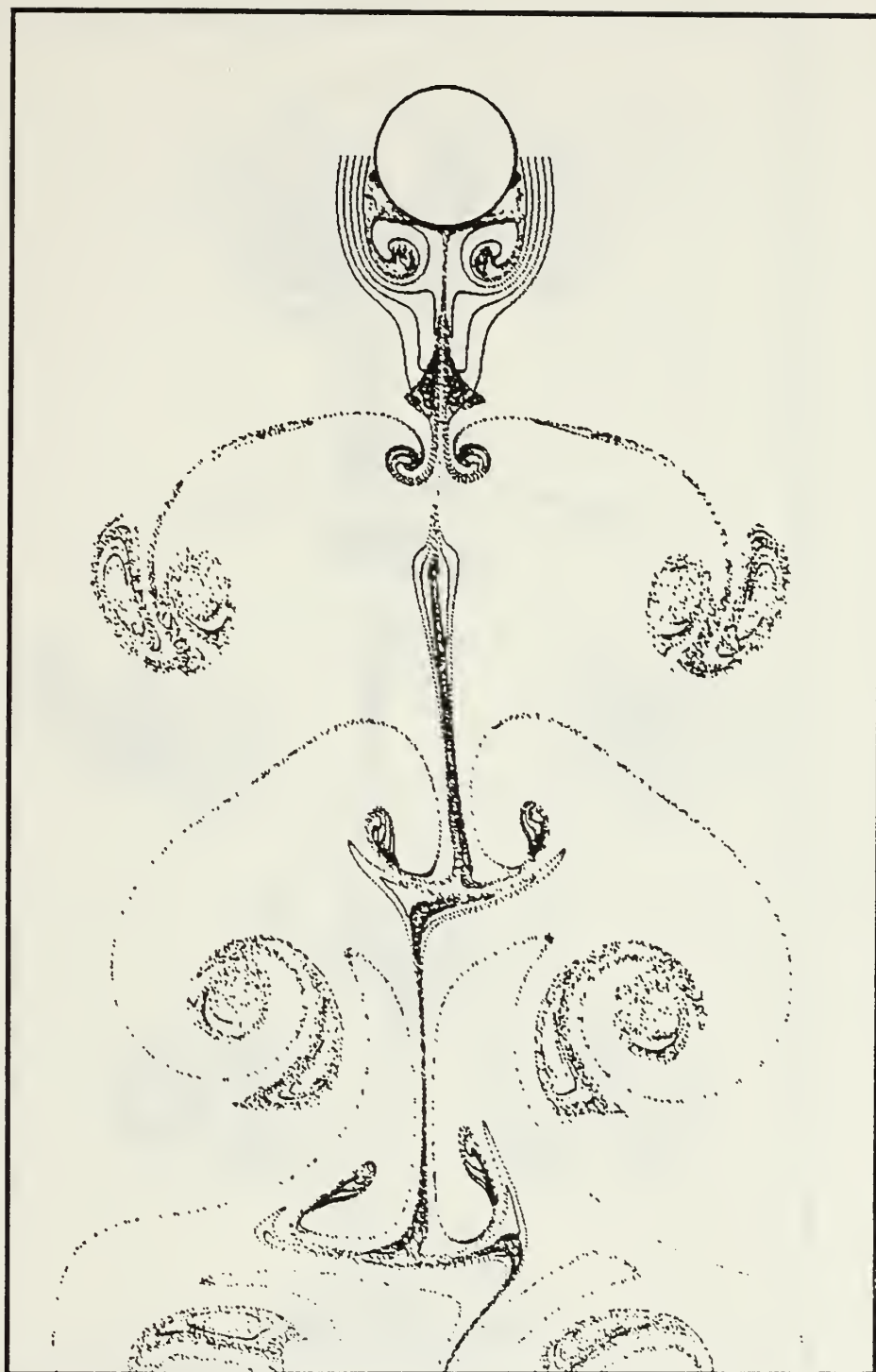


Figure 83. Streaklines, $V_r = 0.8$, $K = 4$, $\beta = 196$, $t/T = 8.3/8$

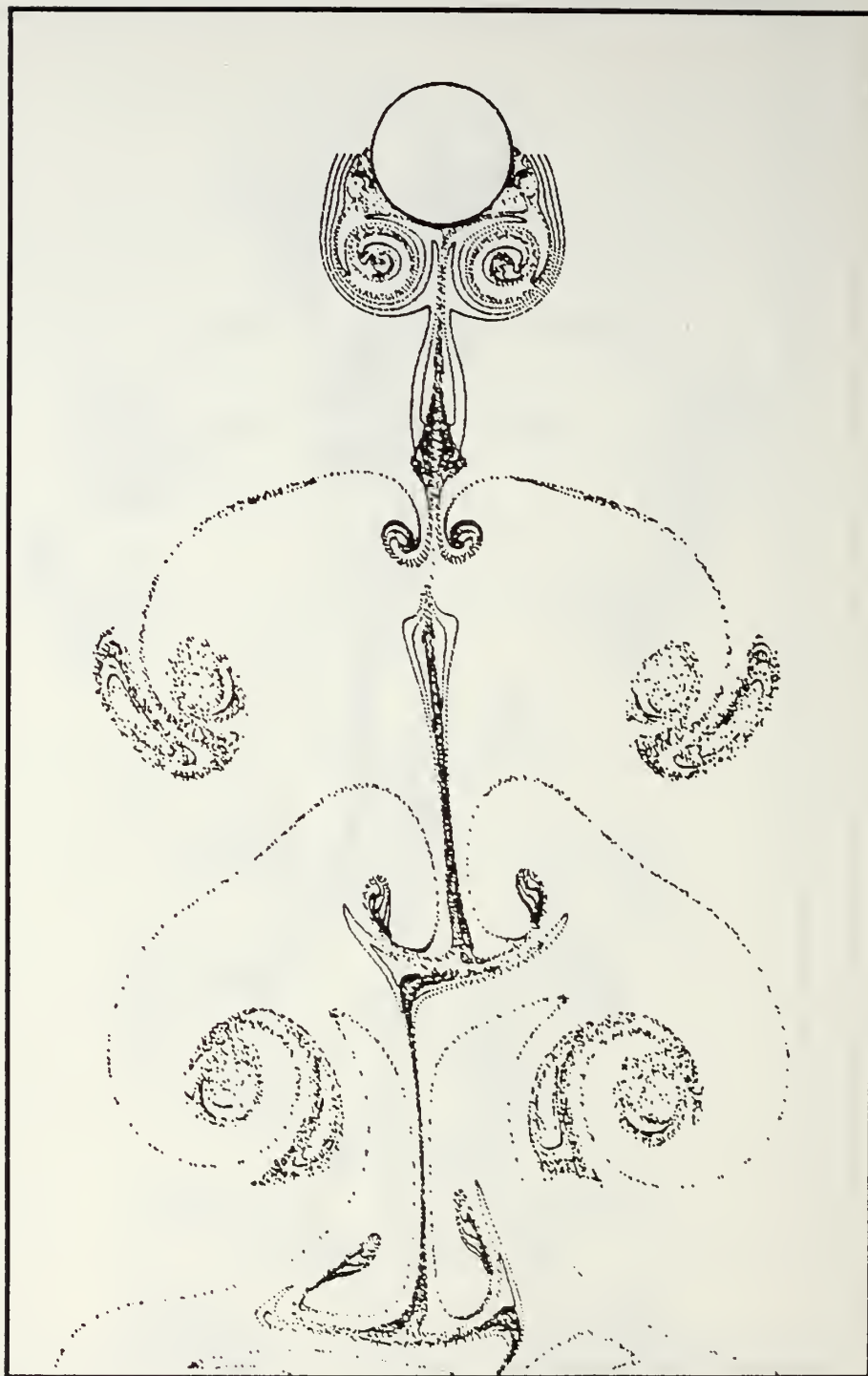


Figure 84. Streaklines, $V_r = 0.8$, $K = 4$, $\beta = 196$, $t/T = 8-4/8$

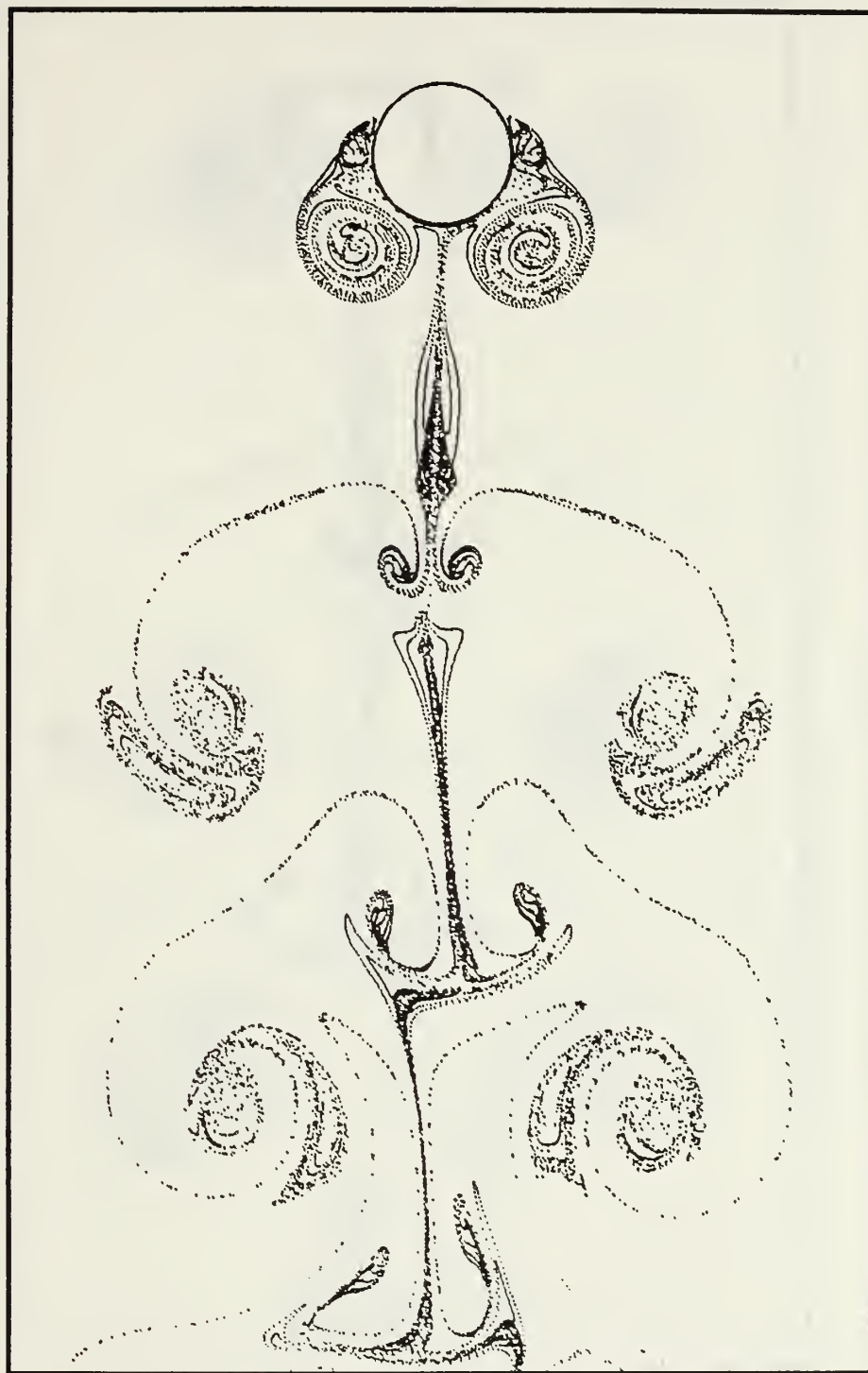


Figure 85. Streaklines, $V_r = 0.8$, $K = 4$, $\beta = 196$, $t/T = 8.5/8$

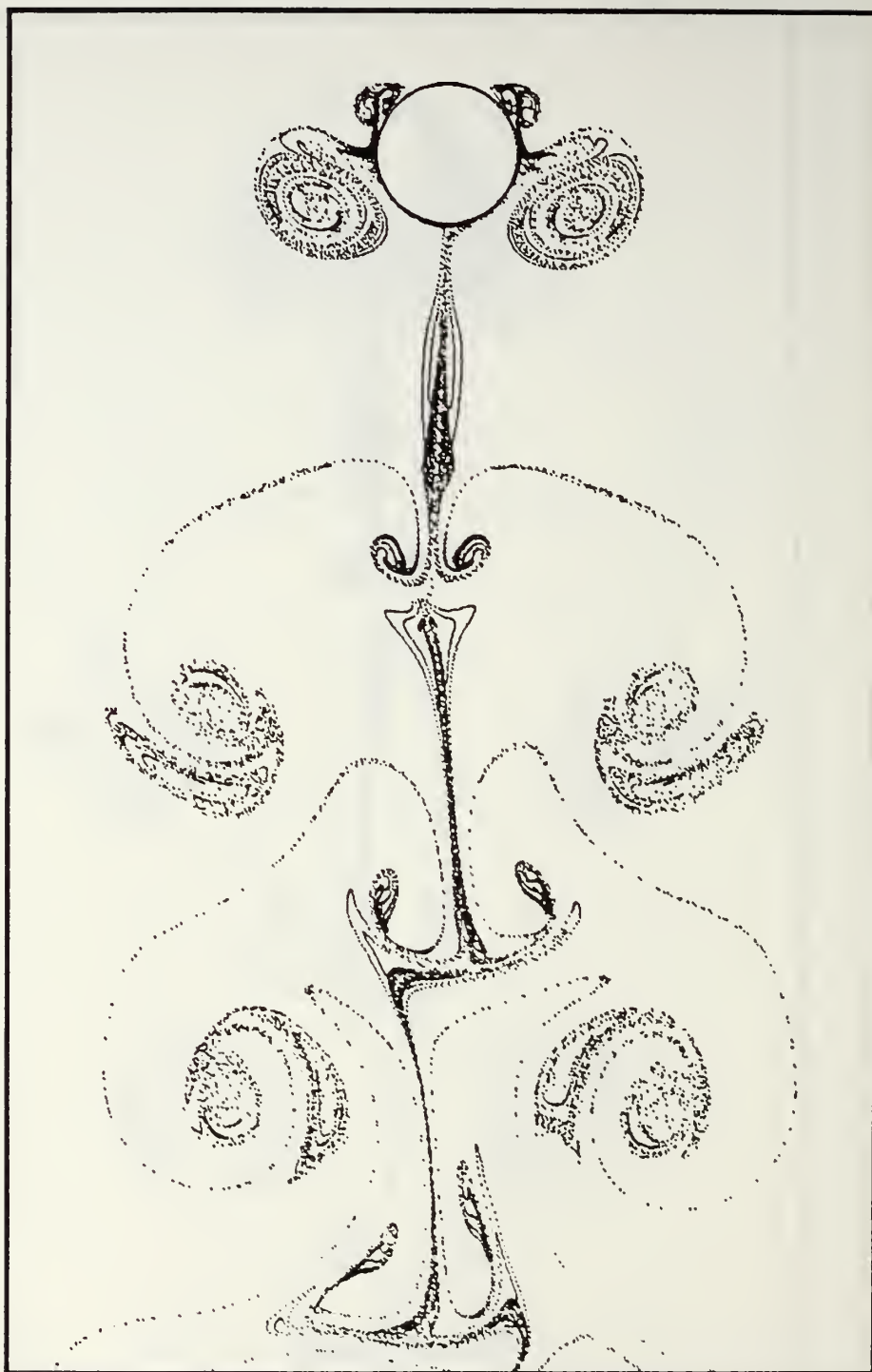


Figure 86. Streaklines, $V_r = 0.8$, $K = 4$, $\beta = 196$, $t/T = 8-6/8$

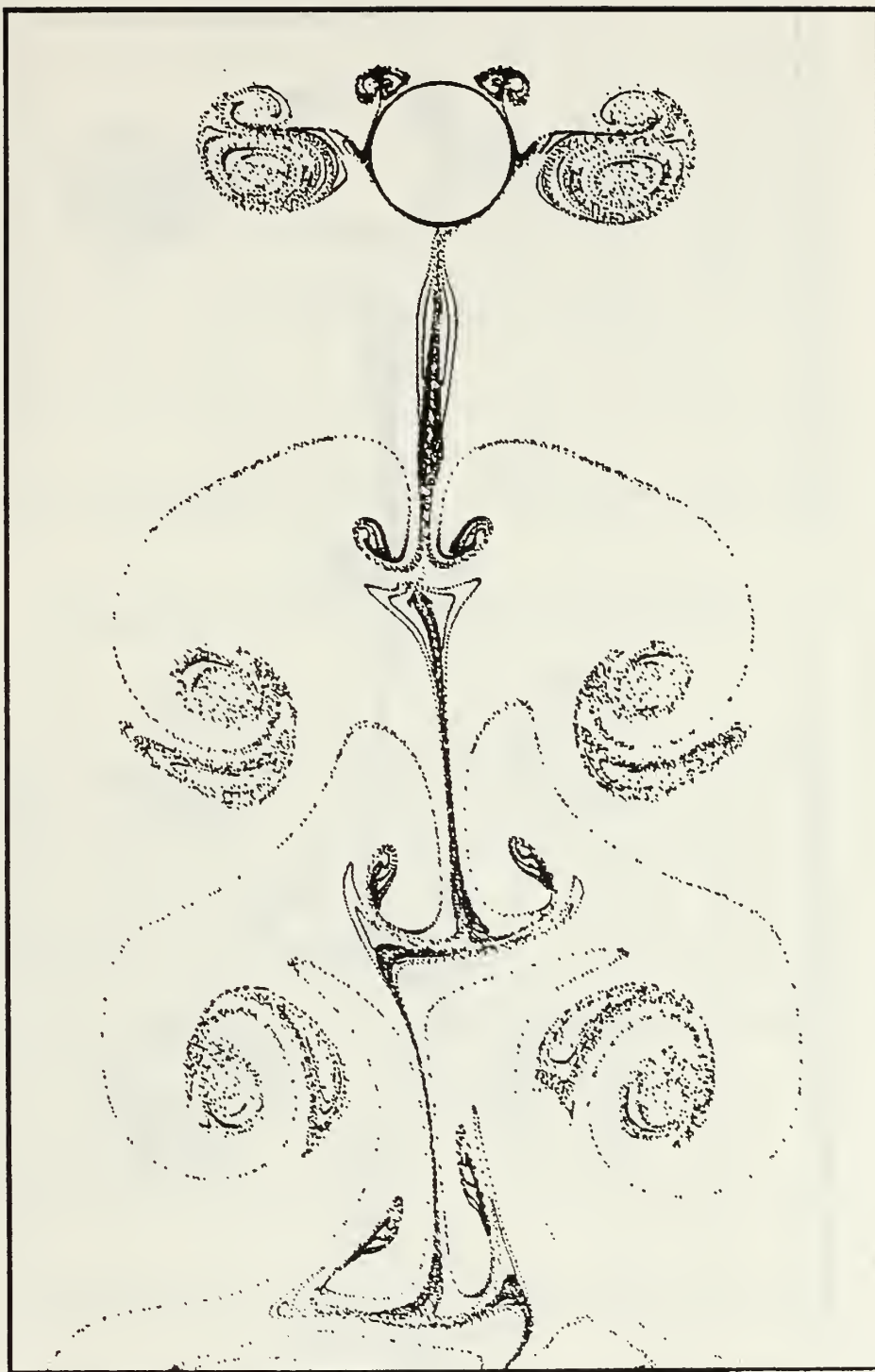


Figure 87. Streaklines, $V_r = 0.8$, $K = 4$, $\beta = 196$, $t/T = 8-7/8$

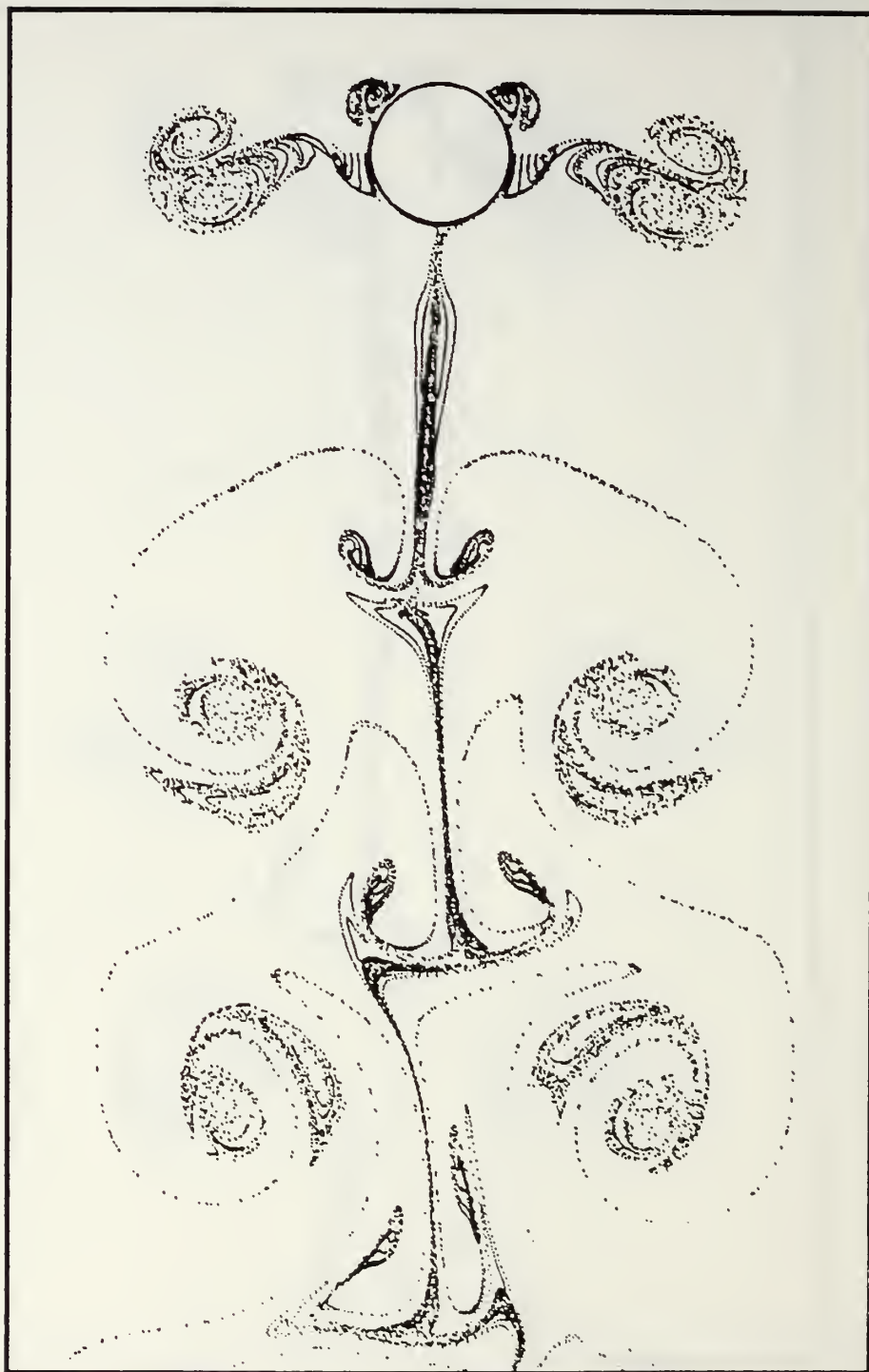


Figure 88. Streaklines, $V_r = 0.8$, $K = 4$, $\beta = 196$, $t/T = 9$

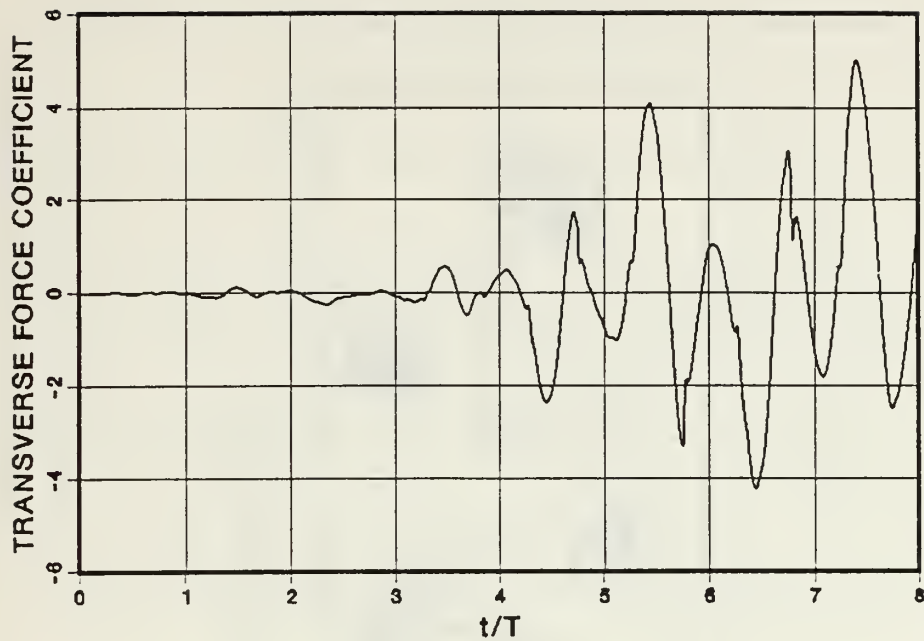


Figure 89. C_L versus t/T , $V_r = 1.0$, $K = 4$, $\beta = 196$

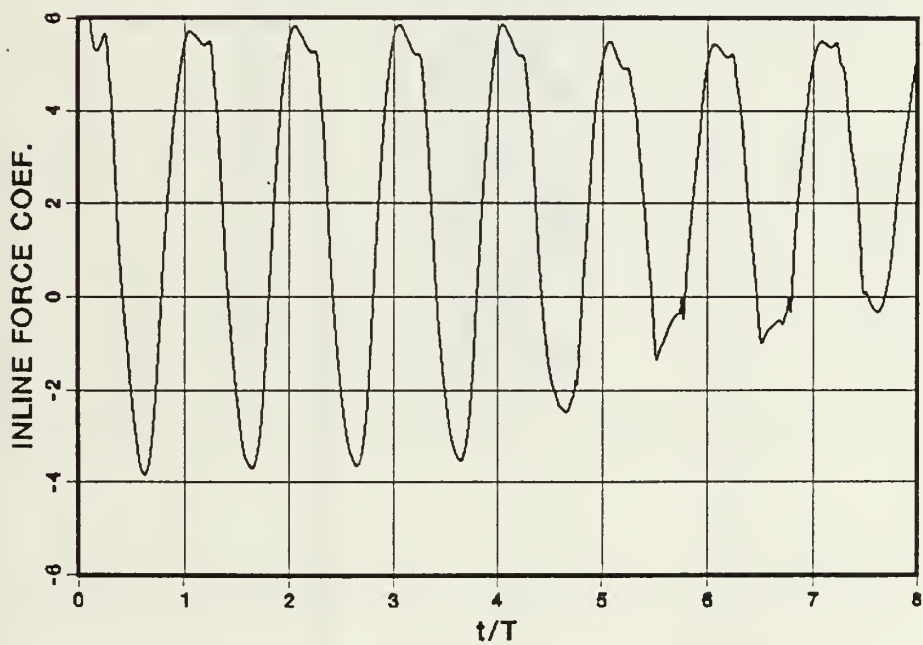


Figure 90. C_{IL} versus t/T , $V_r = 1.0$, $K = 4$, $\beta = 196$



Figure 91. Streaklines, $V_r = 1.0$, $K = 4$, $\beta = 196$, $t/T = 8$

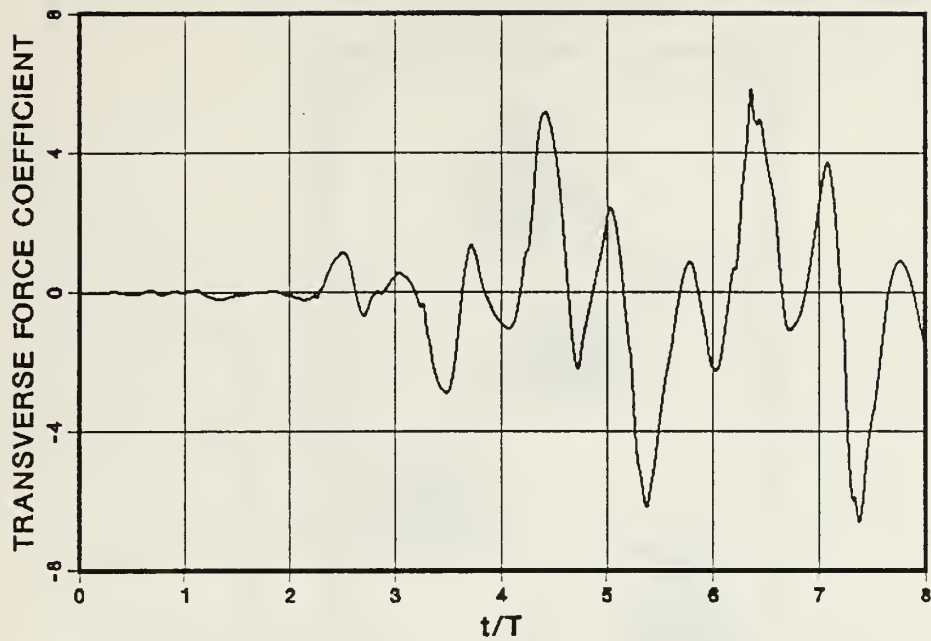


Figure 92. C_L versus t/T , $V_r = 1.1$, $K = 4$, $\beta = 196$

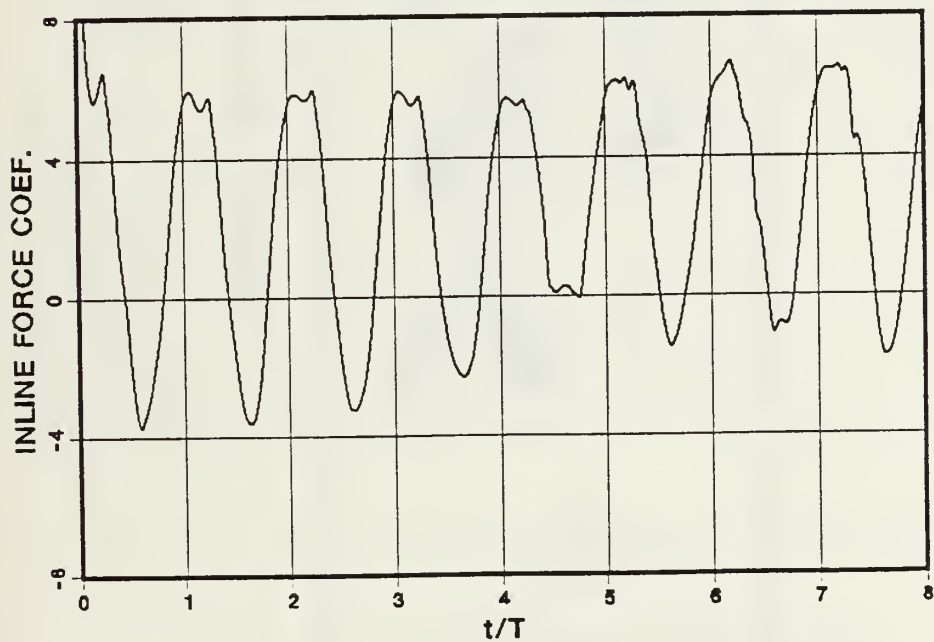


Figure 93. C_{IL} versus t/T , $V_r = 1.1$, $K = 4$, $\beta = 196$



Figure 94. Streaklines, $V_r = 1.1$, $K = 4$, $\beta = 196$, $t/T = 8$

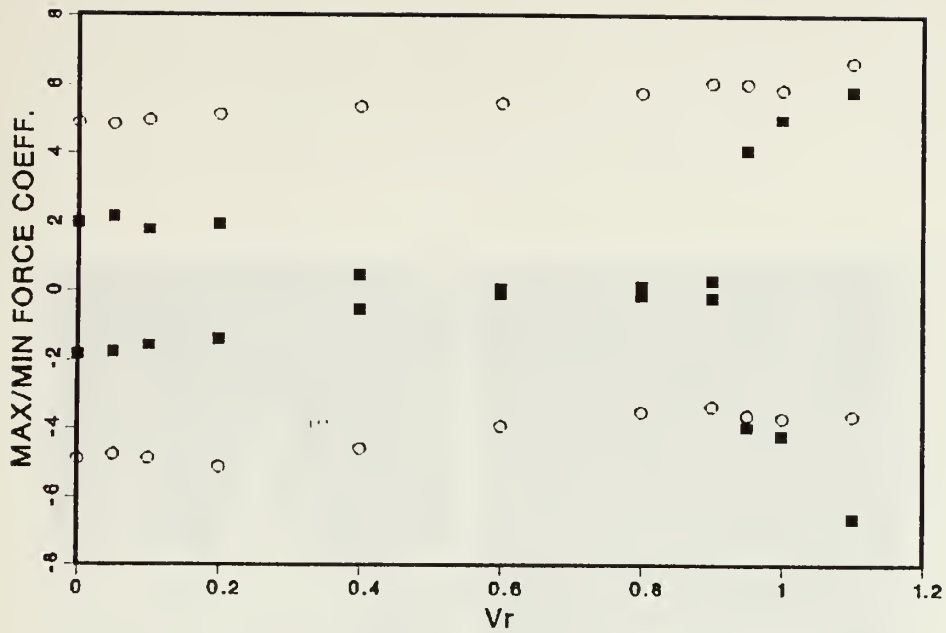


Figure 95. C_{IL} and C_L versus V_r , $K = 4$, $\beta = 196$, $n = 2$
 C_{IL} (open circles), C_L (full squares)

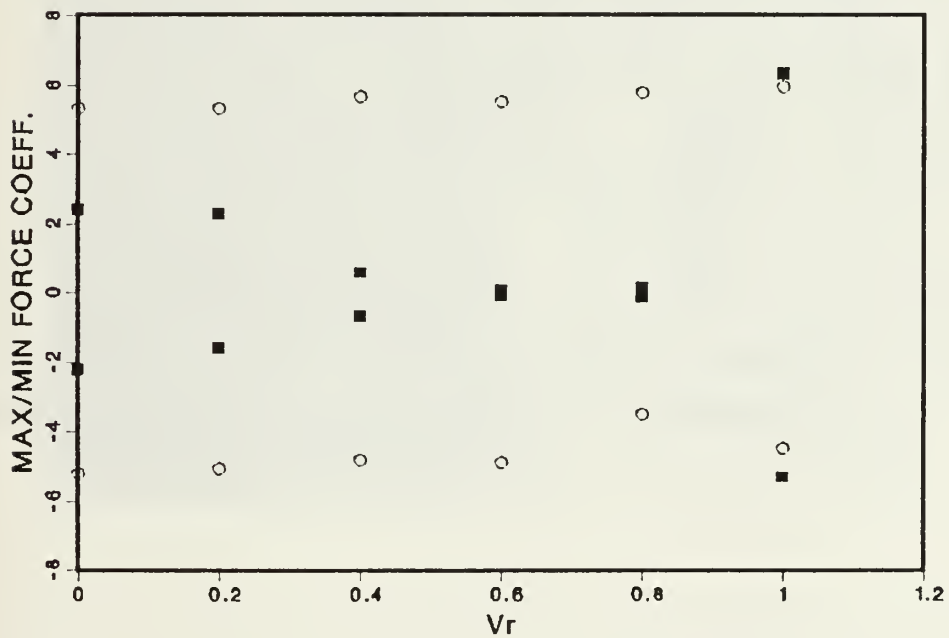


Figure 96. C_{IL} and C_L versus V_r , $K = 4$, $\beta = 196$, $n = 8$
 C_{IL} (open circles), C_L (full squares)

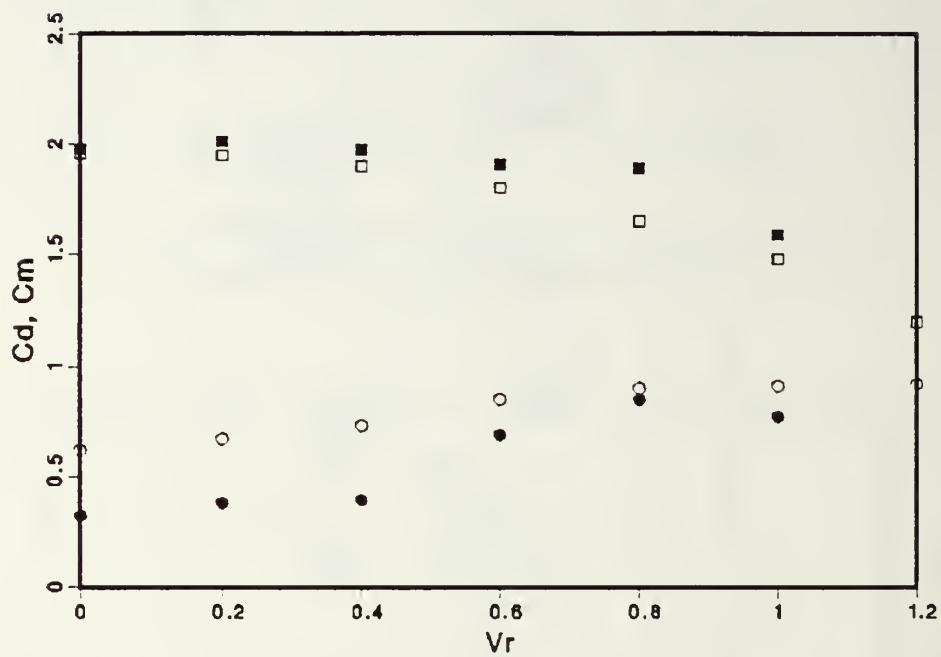


Figure 97. C_d and C_m versus V_r , $K = 4$, $\beta = 196$, $n = 8$,
 C_d numerical (full circles), C_m numerical (full squares)
 C_d experiment (open circles), C_m experiment (open squares)

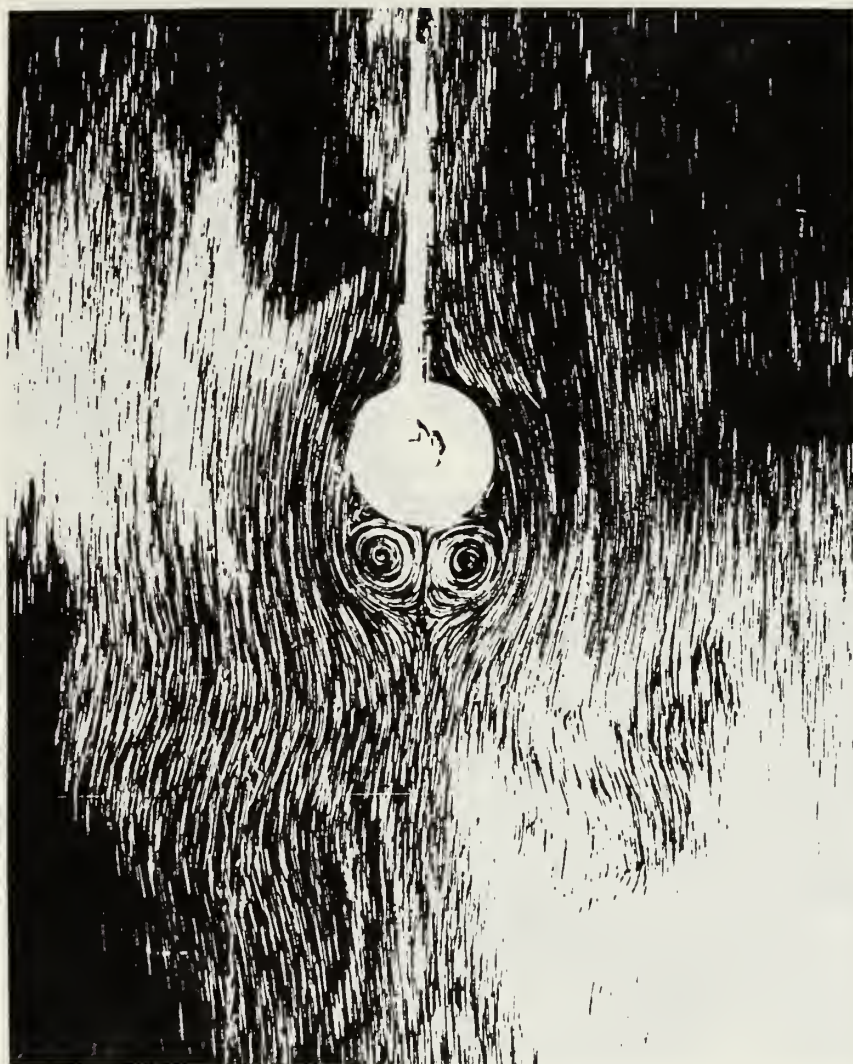


Figure 98. Flow Visualization for $K = 4$, $V_r = 0.8$, $t = 8.3/8$

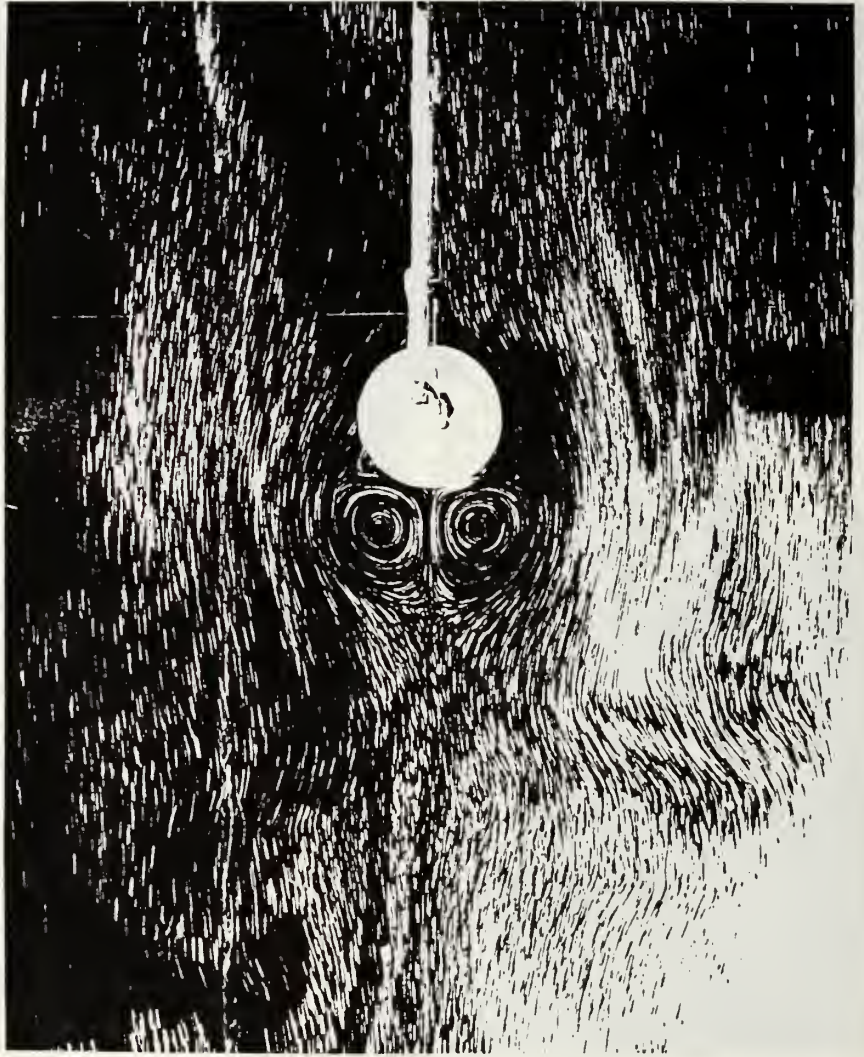


Figure 99. Flow Visualization for $K = 4$, $V_r = 0.8$, $t = 8.4/8$

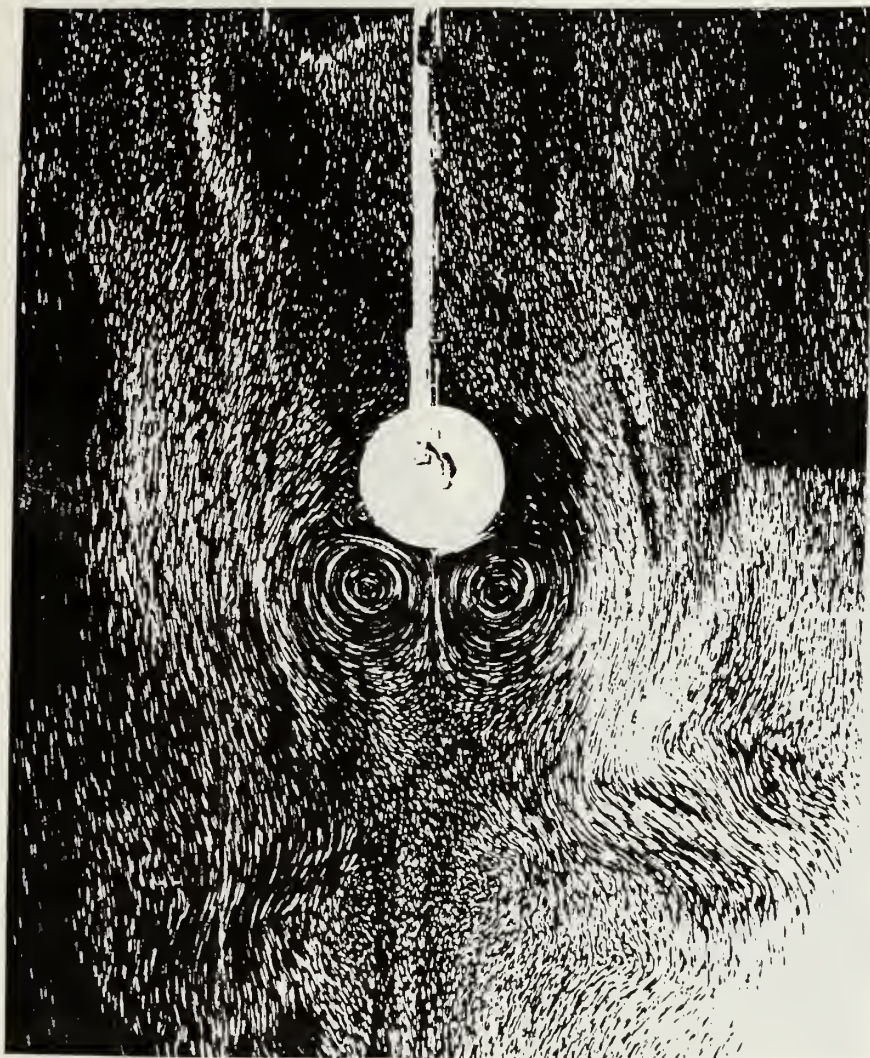


Figure 100. Flow Visualization for $K = 4$, $Vr = 0.8$, $t = 8.5/8$

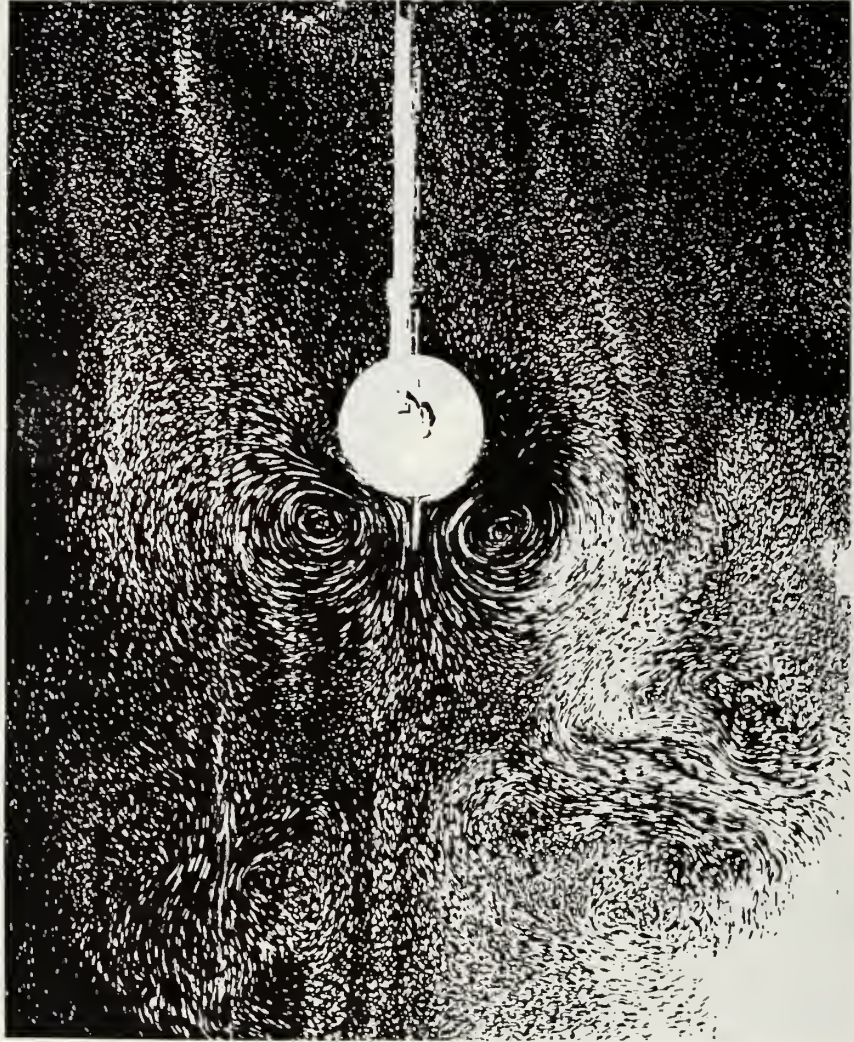


Figure 101. Flow Visualization for $K = 4$, $V_r = 0.8$, $t = 8.6/8$

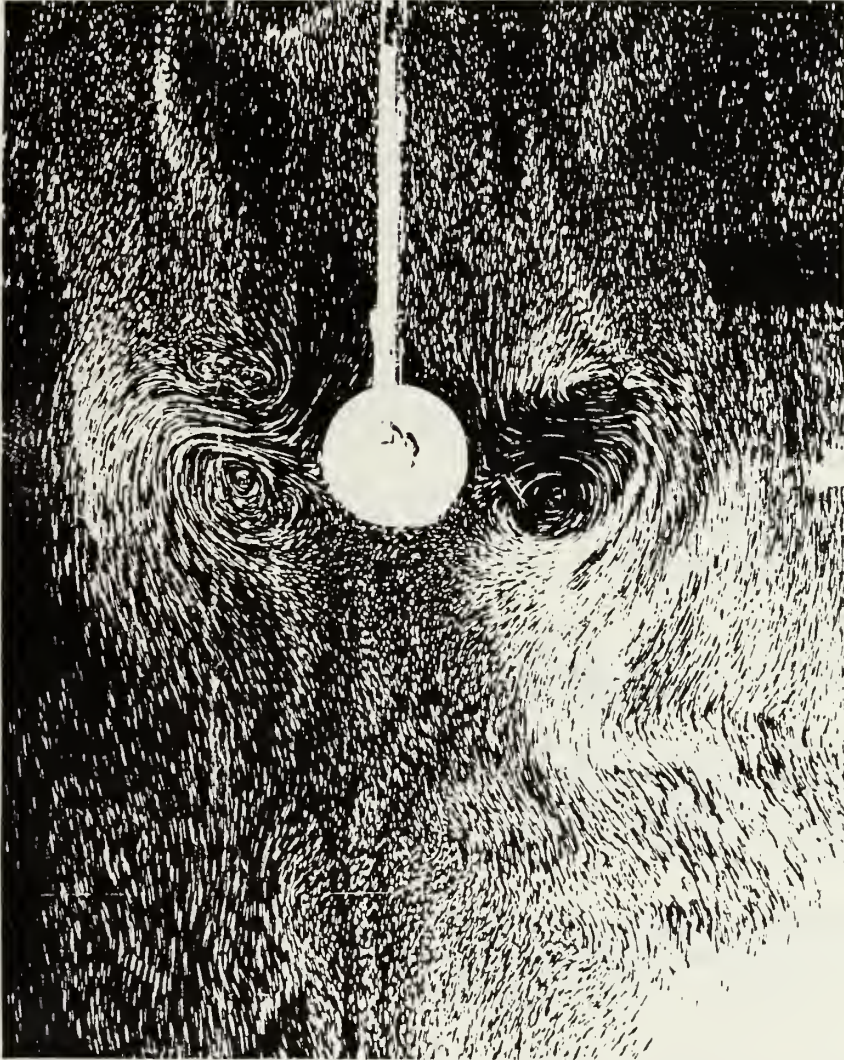


Figure 102. Flow Visualization for $K = 4$, $V_r = 0.8$, $t = 8-7/8$

REFERENCES

1. Baba, N., and Miyata, H., 1987, "Higher-Order Accurate Difference Solutions of Vortex Generation from a Circular Cylinder in an Oscillatory Flow," *Journal of Computational Physics*, Vol. 69, pp. 362-396.
2. Bouard, R., and Coutanceau, M., 1980, "The Early Stage of Development of the Wake Behind an Impulsively Started Cylinder for $40 < Re < 10^4$," *Journal of Fluid Mechanics*, Vol. 101, Part 3, pp. 583-607.
3. Chamberlain, R. R., 1987, "Unsteady Flow Phenomena in the Near Wake of a Circular Cylinder," AIAA Paper No. 87-0317.
4. Chang, C.-C., and Chern, R.-L., 1990, "Numerical Study of Flow Around an Impulsively Started Circular Cylinder by a Deterministic Vortex Method," (to appear in *Journal of Fluid Mechanics* in 1991).
5. Fredrickson, K., 1990, *Numerical Study of Non-impulsively Started Flow Around a Circular Cylinder*, M.S. Thesis, Naval Postgraduate School, Monterey, CA.
6. Justesen, P., 1991, "A Numerical Study of Oscillating Flow Around a Circular Cylinder," *Journal of Fluid Mechanics*, Vol. 222, pp. 157-196.
7. Lecointe, Y., and Piquet, J., 1984, "On the Use of Several Compact Methods for the Study of Unsteady Incompressible Viscous Flow Round a Circular Cylinder," *Computers & Fluids*, Vol. 12, No. 4, pp. 255-280.
8. Lecointe, Y., Piquet, J., and Plantec, J., 1987, "Flow Structure in the Wake of an Oscillating Cylinder," in *Forum on Unsteady Flow Separation* (Ed. K. N. Ghia), ASME, FED-Vol. 52, pp. 147-157.
9. Mostafa, S. I. M., 1987, *Numerical Simulation of Unsteady Separated Flows*, Ph. D. Thesis, Naval Postgraduate School, Monterey, CA.

10. Murashige, S., Hinatsu, M., and Kinoshita, T., 1989, "Direct Calculations of the Navier-Stokes Equations for Forces Acting on a Cylinder in Oscillatory Flow," In Proceedings of the Eight International Conference on Offshore Mechanics and Arctic Engineering, The Hague, Vol. 2, pp. 411-418.
11. Nagata, H., Funada, H., and Matsui, T., 1985, "Unsteady Flows in the Vortex Region Behind a Circular Cylinder Started Impulsively, 2nd Report, Velocity Fields and Circulations," *Japanese Society of Mechanical Engineers*, Vol. 28, No. 245, pp. 2608-2616.
12. Rumsey, C. L., 1988, "Details of the Computed Flowfield Over a Circular Cylinder at Reynolds Number 1200," *Journal of Fluids Engineering, Trans, ASME*, Vol. 110, pp. 446-452.
13. Sarpkaya T., 1966, "Separated Flow About Lifting Bodies and Impulsive Flow About Cylinders," *AIAA Journal*, Vol 3, No.3, pp. 414-420.
14. Sarpkaya, T., 1978, "Impulsive Flow About a Circular Cylinder," Naval Postgraduate School Technical Report No. NPS-69SL-78-008.
15. Sarpkaya, T., 1989, "Computational Methods with Vortices-The 1988 Freeman Scholar Lecture," *Journal of Fluids Engineering, Trans. ASME*, Vol. 111, No. 1, pp. 5-52.
16. Sarpkaya T., 1990, "Non-Impulsively-Started Steady Flow About a Circular Cylinder," *AIAA Paper No. 90-0578*.
17. Sarpkaya, T., and Ihrig, C. J., 1986, "Impulsively Started Steady Flow About Rectangular Prisms: Experiments and Discrete Vortex Analysis," *Journal of Fluids Engineering, Trans. ASME*, Vol. 108, pp. 47-54.
18. Sarpkaya, T., and Kline, H. K., 1982, "Impulsively-Started Steady Flow About Four Types of Bluff Body," *Journal of Fluids Engineering, Trans. ASME*, Vol. 104, pp. 207-213.
19. Sarpkaya, T., and Shoaff, R. L., 1979, "Inviscid Model of Two-Dimensional Vortex Shedding by a Circular Cylinder," *AIAA Journal*, Vol 17, No. 11, pp. 1193-1200.
20. Ta Phuoc Loc, 1980, "Numerical Analysis of Unsteady Secondary Vortices Generated by an Impulsively Started Cylinder," *Journal of Fluid Mechanics*, Vol. 100, Part 1, pp. 111-128.

21. Ta Phuoc Loc and Bouard, R., 1985, "Numerical Solution of the Early Stage of the Unsteady Viscous Flow Around a Circular Cylinder; a Comparison with Experimental Visualization and Measurements," *Journal of Fluid Mechanics*, Vol. 160, pp.93-117.
22. van der Vegt, J. J. W., 1988, *A Variationally Optimized Vortex Tracing Algorithm for 3-Dimensional Flows Around Solid Bodies*, Ph. D. Thesis, Maritime Research Inst., Netherlands.
23. Verley, R. L. P., 1979, "The Forces on a Cylinder Oscillating in a Current," Report No. 608018, River and Harbor Laboratory, Norwegian Institute of Technology, Trondheim, Norway.
24. Wang, X., 1989, *A Numerical Study of Unsteady Flows Past A Circular Cylinder*, Ph.D. Dissertation, University of Houston, Houston, Texas.

INITIAL DISTRIBUTION LIST

No. Copies

- | | | |
|----|---|---|
| 1. | Defense Technical Information Center
Cameron Station
Alexandria, VA 22304-6145 | 2 |
| 2. | Library, Code 0142
Naval Postgraduate School
Monterey, CA 93943-5002 | 2 |
| 3. | Department Chairman, Code ME
Department of Mechanical Engineering
Naval Postgraduate School
Monterey, CA 93942-5000 | 2 |
| 4. | Professor T. Sarpkaya, Code ME-SL
Department of Mechanical Engineering
Naval Postgraduate School
Monterey, CA 93943-5000 | 5 |
| 5. | LT Christopher J. Putzig
1928 Michienzi Rd.
Berne, NY 12023 | 1 |
| 3. | Curricular Officer, Code 34
Department of Naval Engineering
Naval Postgraduate School
Monterey, CA 93942-5000 | 1 |
| 6. | Office of Naval Research
800 North Quincy Street
Arlington, VA 22217 | 1 |
| 7. | Naval Sea Systems Command
PMS 350
Washington, D.C. 20362 | 1 |

Thesis

P977 Putzig

c.1 Numerical experiments in
unsteady flows through
the use of full Navier-
Stokes equations.

DUDLEY KNOX LIBRARY



3 2768 00036937 5